Structure, Function and Mitochondrial Targeting of Sideroflexin-3 (SFXN3)

Amy Elder BSc. (Hons)

A thesis submitted to the University of Glasgow in fulfilment of the requirements for the degree of MSc (Research) Biochemistry and Biotechnology

Institute of Molecular, Cell and Systems Biology

College of Medical, Veterinary and Life Sciences

University of Glasgow

January 2023

Abstract

Mitochondria possess a double membraned structure, consisting of a semi-permeable outer membrane (OM) and an impermeable inner membrane (IM). IM-localised mitochondrial carriers (MCs) are required to allow passage of small molecules across the IM, enabling communication of matrix and cytosol environments. Sideroflexins (SFXN) are a family of MCs comprised of five (SFXN1-5) members in mammals which are each nuclear-encoded and imported into the mitochondria via TIM22 and the carrier import pathway. Mammalian SFXN3 has been the subject of several recent studies, largely owing to the belief that SFXN3 may provide neuroprotection in Parkinson's Disease. Despite the surge in interest, the experimental structure, range of functions and mitochondrial targeting information of SFXN3 remain unknown. The first part of this thesis aimed to predict the transmembrane domain (TM) structure and orientation of SFXN3 at the IM. Through use of topology and AlphaFold structure predictions, we found that SFXN3 is likely a largely helical protein, with 4 TMs, a short C-terminal domain, large N-terminal domain, and beta-strand region conserved across all SFXNs. Topology predictions could not reliably deduce orientation of the N- and C-termini of SFXN3 at the IM. The second part of this thesis aimed to identify the mitochondrial targeting information of SFXN3. Import of ^{35}S-radiolabelled truncations of SFXN3 into isolated mitochondria revealed that the N-terminal domain of SFXN3 may contain mitochondrial targeting information, and three predicted TMs of the protein may enhance efficiency of import. However, reproducibility of said result was not assessed and must be confirmed in future. Further study involved purification of Tim9/10, an IMS-localised chaperone complex which interacts with carrier pathway substrates. Incubation of purified Tim9/10 with an SFXN3 peptide spot array suggests that the N-terminal domain, fourth transmembrane region and preceding loop domain can interact with Tim9/10 complex. This could imply that these regions of SFXN3 are essential for the chaperone interaction and thus mitochondrial import. The final part of this thesis initially aimed to characterise the function of SFXN3. Due to problems in obtaining an SFXN3-knockdown cell line, the aims shifted to characterising function of budding yeast SFXN homolog, fungal sideroflexin-1 (FSF1). Analysis of ΔFSF1 yeast growth revealed that FSF1 was not essential for mitochondrial respiration or iron transport. However, deletion of FSF1 decreased steady state levels of Fe-S cluster protein, mitochondrial aconitase. This

preliminary finding may suggest that FSF1 could play a role in Fe-S cluster biogenesis. However, further study is required to confirm this. Overall, this thesis provides a detailed analysis of SFXN3 structure, narrows down the sequence regions involved in mitochondrial targeting, and provides evidence which disputes certain proposed functions of FSF1. This provides a starting point upon which further study can build to ultimately determine if SFXN3 is a feasible therapeutic target for neurodegenerative disorders.

Table of Contents

List of Figures

List of Tables

Acknowledgements

Firstly, I would like to thank my supervisor Professor Kostas Tokatlidis for giving me the opportunity to complete the MScR in his lab, for all his guidance throughout and his continuous support within and out with the lab. Kostas' never-wavering encouragement has allowed me to gain confidence working in a laboratory environment, for which I am extremely grateful.

Secondly, I would like to thank each and every member of the Tokatlidis lab for all their help throughout the year. I would like to thank Dr. Ruairidh Edwards for showing me the ropes. Ru's patience, enthusiasm and dedication to his students make him a truly excellent teacher and I am very glad I got the opportunity to work with him.

I would also like to thank Dr. Ross Eaglesfield for his continuous advice and guidance throughout the MScR. Additionally, I would like to thank Erik Lacko for sharing his expertise and taking the time to help with the protein purification aspect of this study.

Author's Declaration

I declare that this thesis is the result of my own work, unless explicit reference is made to the work of others. The work in this thesis has not been submitted for any other degree at the University of Glasgow or any other institution.

List of Abbreviations

AAC: ADP/ATP carrier

ABCB: ATP-binding cassette subfamily B

ACO2: Mitochondrial aconitase

ALAS1/2: ALA synthase 1/2

ATP: Adenosine triphosphate

BSA: Bovine serum albumin

CCCP: Carbonyl cyanide m-chlorophenyl hydrazone

COPROIII: Coproporphyrinogen III

DDM: Dodecyl beta-D-maltoside

DMEM: Dulbecco's modified eagle medium

DTT: 1,4-Dithiothreitol

EGTA: Egtazic acid

ETC: Electron transport chain

FADH2: Flavin adenine dinucleotide

FBS: Foetal bovine serum

FECH: Ferrochelatase

FPLC: Fast protein liquid chromatography

FSF1: Fungal sideroflexin-1

H_2O_2: Hydrogen peroxide

IMM: Inner mitochondrial membrane

IMP1/2: Inner membrane protease 1/2

IMS: Intermembrane space

ISC: Iron-sulfur cluster

ITS: IMS targeting signals

KD: Knockdown

KO: Knockout

LB: Luria-Bertani

MC: Mitochondrial carriers

MIM: Mitochondrial import channel

MISS: Mitochondrial intermembrane space sorting signals

MMP: Matrix processing peptidase

MPC: Mitochondrial pyruvate carrier

MSA: Multiple sequence alignment

MTS: Mitochondrial targeting sequence

NADH: Nicotinamide adenine dinucleotide

NSF1: Cysteine desulfurase

OMM: Outer mitochondrial membrane

OXPHOS: Oxidative phosphorylation

PAM: Pre-sequence translocase-associated motor complex

PBS: Phosphate-buffered saline

PD: Parkinson's disease

PDB: Protein data bank

PPG IX: Protoporphyrinogen IX

PPIX: Protoporphyrin IX

SAM: Sorting and assembly machinery

SFXN: Sideroflexin

shRNA: Short-hairpin RNA

SLC25: Solute carrier family 25

TA: Tail-anchored

TCA: Tricarboxylic acid

TIM: Translocase of inner membrane

TM: Transmembrane domain

TOM: Translocase of the outer membrane

TR: Transmembrane region

TRO: Non-transfected

YPD: Yeast extract peptone dextrose

YPGal: Yeast extract peptone galactose

YPLac: Yeast extract peptone lactose

1-C: One-carbon

Chapter 1: Introduction

1.1 Mitochondria: discovery and structure

In the 19th century Altmann and colleagues identified granule-like structures within the cell cytoplasm (Altmann, 1890). Based on their appearance, these structures were later termed 'mitochondria' by Carl Benda, whereby 'mitos' is Greek for thread and 'chondros' Greek for granules (Benda, 1898). In the years following discovery, numerous researchers helped uncover the detail of mitochondrial structure. Electron micrographs revealed the mitochondria to be a double membraned organelle – having an outer (OMM) and an inner mitochondrial membrane (IMM) (Palade, 1953; Sjostrand, 1953). The IMM surrounds the innermost compartment of the mitochondria – the matrix – and contained between the IMM and OMM is an aqueous compartment known as the intermembrane space (IMS) (**fig. 1.1**). The IM is folded internally to form cristae, increasing capacity for electron transport which will be discussed in more detail in the next paragraphs. In addition, mitochondria contain mtDNA that encodes proteins which can be synthesised on ribosomes within the organelle itself (Greber and Ban, 2016).

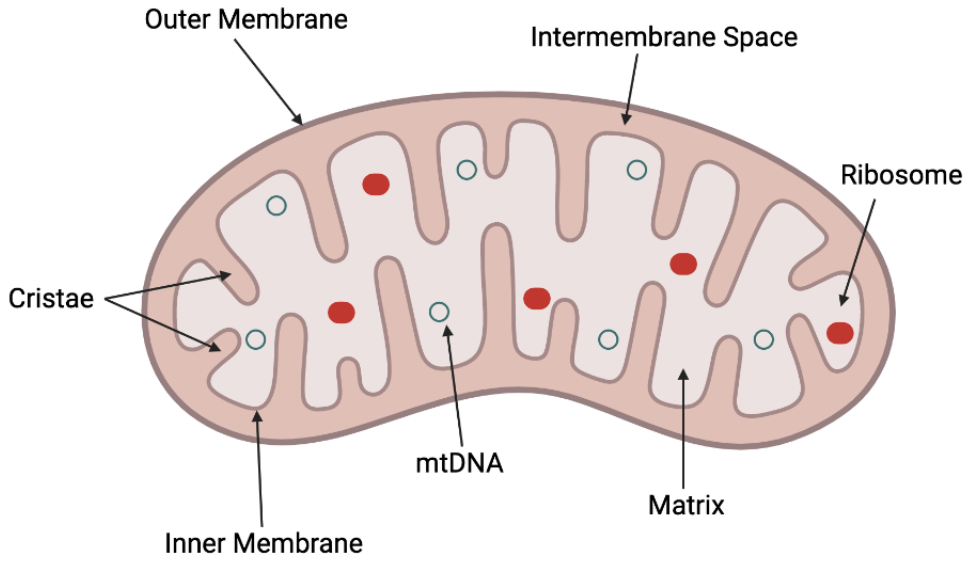

Fig. 1.1: Schematic showing structure of the mitochondrion

The four compartments of the mitochondria (outer membrane, intermembrane space, inner membrane and matrix) are labelled. Mitochondrial DNA (mtDNA)

and ribosomes are located in the matrix. Ribosomes are shown as red circles. Cristae (invaginations of the IM) are also annotated.

1.2 An overview of mitochondrial functions

1.2.1 Mitochondrial respiration

Following discovery, mitochondria were also quickly implicated in cellular bioenergetics (Kennedy and Lehninger, 1949; Hogeboom and Schneider, 1950). Today, mitochondria are widely referred to as 'the powerhouse of the cell' as they generate more than 90% of a eukaryotic cells energy (in the form of adenosine triphosphate (ATP)) via oxidative phosphorylation (OXPHOS).

OXPHOS can be divided into two processes: the electron transport chain (ETC) and ATP generation. In mammals, the ETC consists of four IM-embedded multi-subunit respiratory complexes (complex I-IV). To commence the ETC, electrons are transferred from nicotinamide adenine dinucleotide (NADH) or flavin adenine dinucleotide (FADH2) to respiratory complex I or II, respectively (Martínez-Reyes and Chandel, 2020). As electrons move along the ETC, complexes I, III and IV pump protons from the matrix into the IMS. Ultimately, this generates an electrochemical proton gradient across the IMM. The proton gradient then drives the second process of OXPHOS - ATP generation from ADP and inorganic phosphate (P_i), which occurs via the action of additional IM-embedded complex ATP synthase (or complex V) (Letts and Sazanov, 2017). ETC of *S. cerevisiae* differs in that it lacks complex I, and rather electrons enter OXPHOS via transfer from a different NADH dehydrogenase, Ndi1 (Iwata et al., 2012).

Central to the transfer of electrons during OXPHOS are the prosthetic groups of respiratory complexes, such as iron-sulfur clusters (Fe-S) and heme. Heme is a complex which consists of protoporphyrin IX (PPIX) and ferrous iron (Fe^{2+}), whereas Fe-S clusters are comprised of variable numbers of iron and sulfur atoms. The numbers of prosthetic groups in each mammalian complex are shown in **fig. 1.2.** *S. cerevisiae* respiratory complexes II and III also contain both heme and Fe-S clusters, complex IV harbours only heme whereas the Ndi1 lacks heme

and Fe-S clusters entirely (Lange and Hunte, 2002; Lemire and Oyedotun, 2002; Seo et al., 2006; Iwata et al., 2012; Berndtsson et al., 2020). Fe-S clusters and heme are essential for the activity of each respiratory complex in which they are present, and thus are essential for the generation of ATP via oxidative phosphorylation (Horowitz and Greenamyre, 2011).

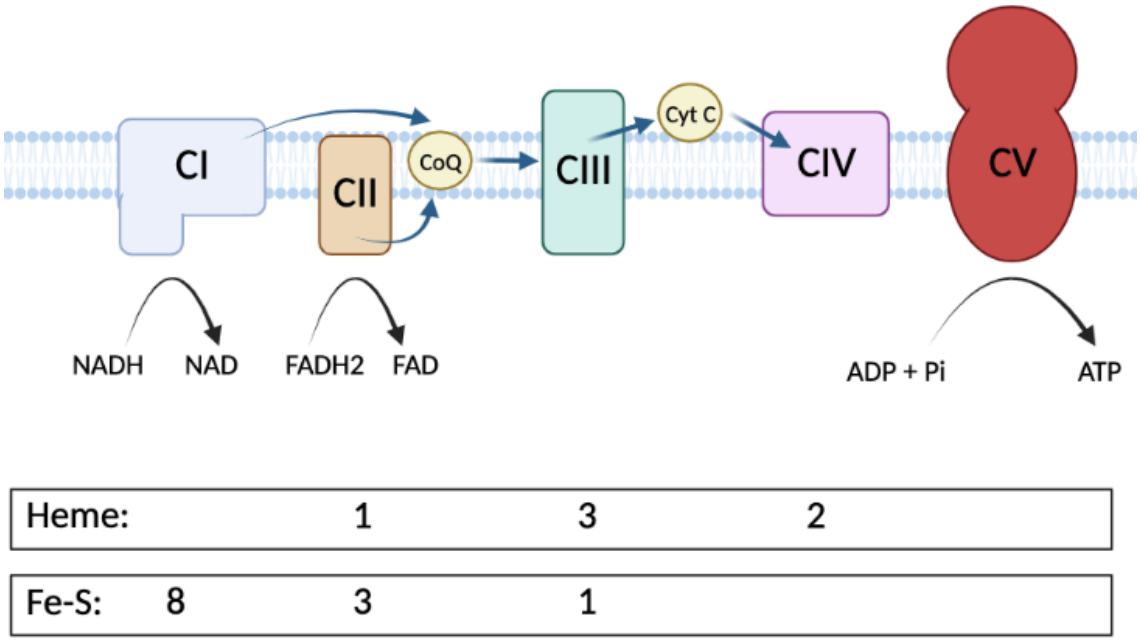

Fig. 1.2: Complexes of mammalian OXPHOS, showing passage of electrons and number of heme/Fe-S prosthetic groups. *A schematic of OXPHOS is shown, including complexes I - V (CI-CV). The passage of electrons is illustrated by blue arrows.*

1.2.2 Iron-sulfur cluster and heme biogenesis in the mitochondria

Mitochondria have several functions beyond energy generation. For instance, biogenesis of Fe-S clusters and heme biosynthesis are reliant on mitochondria.

Heme biosynthesis consists of eight steps in mammals and yeast, with four occurring in the mitochondria. As depicted in **fig. 1.3**, step one occurs in the mitochondrial matrix, whereby ALA synthase (ALAS1/2) catalyses the condensation of succinyl CoA and glycine to generate 5-aminolevulinic acid. Subsequently, ALAS1/2 is exported into the cytosol where an additional four

enzyme-catalysed steps generate coproporphyrinogen III (COPROIII). COPROIII is then believed to be imported back into the mitochondria via OM transporter ATP-binding cassette subfamily B member 6 (ABCB6) and across the IMM by the 2-oxoglutarate carrier (Kabe et al., 2006; Song et al., 2021). The final three enzyme-catalysed steps occur in the matrix: (1) oxidative decarboxylation of COPROIII to protoporphyrinogen IX (PPG IX), catalysed by coproporphyrinogen III oxidase, (2) oxidation of PPG IX to PPIX, catalysed by porphyrinogen IX oxidase and (3) incorporation of iron into PPIX to produce heme, catalysed by ferrochelatase (FECH) (Hoffman, Góra and Rytka, 2003). Heme is not only crucial for the activity of the respiratory complexes aforementioned, but is also implicated in other functions such as oxygen transport (via incorporation of heme into haemoglobin) and antioxidant responses (via incorporation of heme into peroxidases) (Sawicki, Chang and Ardehali, 2015).

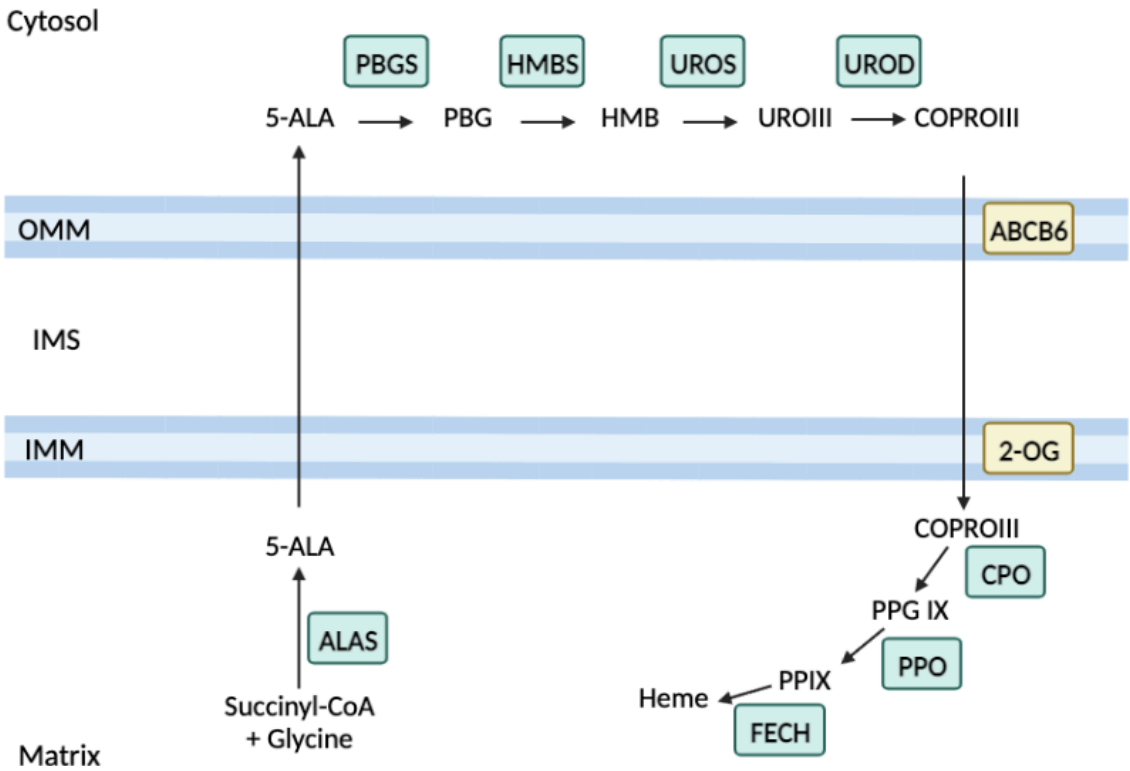

Fig. 1.3: Heme biosynthesis pathway. *The heme biosynthesis pathway is initiated in the matrix, generating 5-ALA from succinyl-CoA and glycine. 5-ALA is then transported to the cytosol and converted to COPROIII via 4 enzyme-catalysed reactions. COPROII is transported across the OM and IM into the matrix where three sequential reactions result in heme generation. Enzymes*

involved in heme biosynthesis are shown in green boxes. Mitochondrial transporters are shown in yellow boxes. ALAS, 5-amiolevulinate synthase; 5-ALA, 5-aminolevelunic acid; PBGS, porphobilinogen synthase; HMBS, hydroxymethylbilane synthase; UROS, uroporphyrinogen III synthase; UROD, uroporphyrinogen decarboxylase; PBG, porphobilinogen; HMB, hydroxymethylbilane; UROIII, uroporphyrinogen III; COPROIII, coproporphyrinogen III; CPO, coproporphyrinogen III oxidase; PPO, porphyrinogen IX oxidase; FECH, ferrochelatase; PPG IX, protoporphyrinogen IX; PPIX, protoporphyrin IX. Figure adapted from Paul et al. (2017).

Moreover, as Fe-S clusters are co-factors for proteins involved in various biological pathways, their biogenesis is a crucial function of mitochondria. Fe-S biogenesis is highly complex. For ease of understanding, an overview of the main steps will be provided.

In mammals, biogenesis of Fe-S clusters for incorporation into mitochondrial proteins is initiated on the iron-sulfur cluster (ISC) complex found in the matrix. ISC complex is comprised of dimeric cysteine desulfurase (NSF1), its cofactor pyridoxal phosphate, ISD11 and ACP bound to scaffold protein IscU. A nascent Fe-S cluster binds at IscU (Paul et al., 2017). NSF1 provides sulfur, which is transferred to the cluster upon binding of frataxin to the complex. Electrons are provided to the ISC complex by NADH. Frataxin can bind Fe^{2+} thus may be responsible for delivery of iron to the complex, however this has not been confirmed *in vivo* (Lane et al., 2015). Upon such delivery of electrons and iron, the Fe-S cluster is assembled. Following assembly, IscU bound to an Fe-S cluster is transferred to chaperones (HSPA9/HSC20) which deliver the cluster to the mitochondrial protein of interest or an intermediate carrier. Typically, the binding of Fe-S clusters to target proteins is mediated via an ionic interaction occurring between cysteine and iron (Paul et al., 2017). The process is highly similar in yeast, with *S. cerevisiae* possessing homologs of all proteins described (Lane et al., 2015; Shi et al., 2021). Additionally, it is generally believed that biogenesis of Fe-S clusters for cytosolic proteins is reliant on the mitochondria, with the ABCB7 transporter (Atm1p in yeast) being proposed to transport an

unknown substrate which contains sulfur from the matrix to the IMS for subsequent transport to the cytosol (Kispal et al., 1997; Lill et al., 2015).

In addition to the essential function of Fe-S clusters in permitting electron transfer through ETC complexes, Fe-S clusters are also required for activity of tricarboxylic acid cycle enzyme mitochondrial aconitase, structure of DNA damage repair enzyme DNA glycosylase, and regulation of SoxR activity during oxidative stress (Brzóska, Męczyńska and Kruszewski, 2006; Kobayashi, Fujikawa and Kozawa, 2014). Heme biosynthesis is also dependent on Fe-S biogenesis, as mammalian FECH and yeast/mammalian porphobilinogen synthase require Fe-S clusters for optimal activity (Dailey, Finnegan and Johnson,1994; Liu et al., 2020). Additionally, it should be noted that heme and Fe-S biogenesis are also linked by their requirement for mitochondrial iron.

1.2.3 Mitochondria: much more than powerhouses

Mitochondria also house processes such as fatty acid β-oxidation and the tricarboxylic acid (TCA) cycle, which generate NADH and FADH2 to facilitate electron transfer to the ETC as described in section 1.2.1 (Martínez-Reyes and Chandel, 2020). The TCA cycle also generates numerous metabolites with a vast range of cellular functions. For instance, TCA produces succinate, which functions in processes such as thermogenesis and tumorigenesis (Mills et al., 2018; Martinez-Reyes and Chandel, 2020).

Moreover, mitochondria are involved in numerous cell signalling pathways. For example, the mitochondria play an important role in the initiation of apoptosis via the intrinsic apoptotic signalling pathway. Said pathway promotes cell death through cytochrome C release and subsequent apoptosome formation (Liu et al., 1996; Bock and Tait, 2020). Too, mitophagy (a type of autophagy pathway whereby mitochondria are degraded) is dependent on the recruitment of E3 ubiquitin ligase Parkin to damaged mitochondria by a mitochondrial kinase (PINK1) (Fiesel et al., 2010). Additionally, a plethora of studies suggest that mitochondria can regulate immune responses by various means. To focus on one,

mitochondrial antiviral-signalling protein is activated upon detection of viral RNA, ultimately stimulating pro-inflammatory cytokine release (Vasquez and Horner, 2015). Finally, mitochondria also play roles in amino acid biosynthesis, steroidogenesis, and lipid synthesis (Liu, Rone and Papadopoulos, 2006; Schlame, 2008). Therefore, although mitochondria are vital for ATP generation, these organelles are far more than a powerhouse.

1.3 Mitochondrial Import Pathways

Each mitochondrial function is dependent on mitochondrial proteins. Proteomics has revealed the mitochondrial proteome of mammals and yeast to be comprised of between 1000 and 1500 proteins (Pfanner, Meisinger and Schmidt, 2010; Rath et al., 2021). mtDNA encodes only ~1% of said proteins, which are synthesised on ribosomes in the matrix as aforementioned (**fig. 1.1**). The remaining 99% of mitochondrial proteins are nuclear-encoded and synthesised in the cytoplasm. Therefore, such proteins must be imported from the cytoplasm into the mitochondria. To achieve localisation of mitochondrial proteins to the appropriate intraorganellar compartment, numerous import pathways exist.

The studies which dissected mitochondrial import pathways were primarily conducted using yeast as a model organism, and have since been shown to be highly conserved across species (Hoogenraad, Ward and Ryan, 2002). Thus, import pathways described throughout section 1.3 can be assumed to be those of yeast (*S. cerevisiae*) unless explicitly stated otherwise.

1.3.1 Import into the matrix via the pre-sequence pathway

The majority of proteins destined for the matrix (~70%) follow the pre-sequence import pathway (**fig. 1.4**). Import of proteins via this pathway is reliant on a mitochondrial pre-sequence, or mitochondrial targeting sequence (MTS), first characterised by Gottfried Schatz (Hurt, Pesold-Hurt and Schatz, 1984). Pre-sequences are typically located at the N-terminus of a protein and consist of 15-50 amino acids which form an amphipathic helix, whereby one side of the helix is hydrophobic and the other positively charged (Pfanner, 2000).

Following synthesis on cytosolic ribosomes, precursors bearing an MTS are present in an unfolded ('import-competent') state. To initiate import of precursors, they are bound by cytosolic chaperones (Hsp70/Hsp90) to maintain the import-competent state and prevent their aggregation (Sha and Wu, 2006). Upon ATP hydrolysis by Hsp70/90 chaperones, the precursor is released and transferred to the translocase of the outer membrane (TOM) complex (**fig. 1.4)**. The TOM complex is comprised of receptors (Tom20, Tom22 and Tom70), small Tom proteins (Tom5, Tom6 and Tom7) and Tom40. The latter is a 19-transmembrane beta-barrel protein which forms a ~20Å wide channel to allow passage from cytosol to IMS (Hill et al., 1998; Wiedemann and Pfanner, 2017). Foremost, Tom20 binds the precursor via hydrophobic interactions with the amphipathic pre-sequence. Subsequently, the precursor is passed to Tom22 to which it binds via interaction of the positively charged side of the amphipathic helix and negatively charged patches of Tom22 (Komiya et al., 1998; Yano, Terada and Mori, 2004). The precursor then passes through Tom40, and binds the negatively charged IMS-localised region of Tom22 (Van Wilpe et al., 1999; Araiso et al., 2019). This transfer from Tom22, through Tom40 and back to Tom22 on the IMS side is driven by the 'acid chain' hypothesis (Komiya et al., 1998).

Once in the IMS, precursors are transferred to the translocase of the inner membrane (TIM23) complex. The TIM23 complex is comprised of various subunits: Tim17, Tim21, Tim23, Tim44 and Tim50. Foremost, Tim50 binds the precursor to permit its transfer to the IMS domain of Tim23 (Lytovchenko et al., 2013). Tim23 forms a channel through the IM through which precursors can pass in the presence of the IM membrane potential ($\Delta\Psi$) (Dekker et al., 1993). However, $\Delta\Psi$ alone is insufficient for matrix import. To achieve complete precursor translocation into the matrix, the pre-sequence translocase-associated motor complex (PAM) must be recruited by TIM23. PAM is comprised of mtHsp70, Tim44, Pam16, Pam18 and Mge1 (Li et al., 2004; Wiedemann and Pfanner, 2017). Tim44 facilitates the coupling of matrix-localised mtHsp70 to TIM23. The precursor binds mtHsp70 at its C-terminal peptide binding domain. Subsequent cycles of ATP hydrolysis by mtHsp70, facilitated by co-chaperones Pam16 and Pam18 and nucleotide-exchange factor Mge1, efficiently translocates the protein

into the matrix (Kang et al., 1990; Li et al., 2004; Wiedemann et al., 2007). Once matrix-localised, the pre-sequence of the precursor can be removed via action of matrix processing peptidase (MPP) (Hawlitschek et al., 1988; Vögtle et al., 2009). Folding of the protein in the matrix requires additional chaperones, including Hsp60 (Ostermann et al.,1989).

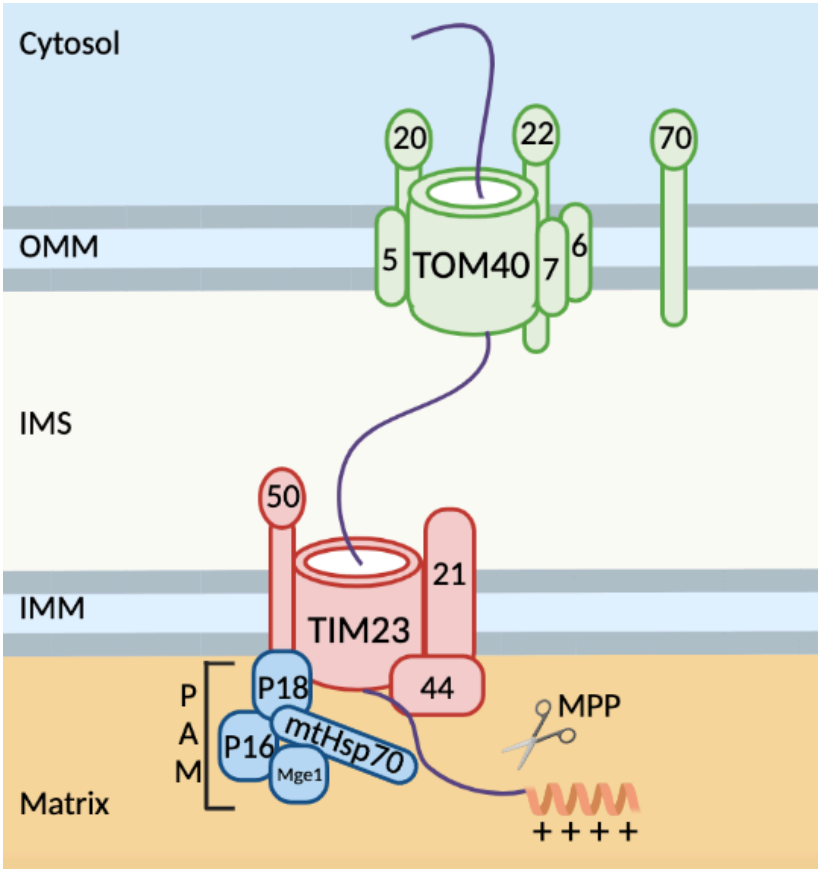

Fig. 1.4: Import into the mitochondrial matrix via the pre-sequence pathway. *Briefly, matrix import involves passage of the pre-sequence-containing precursor through TOM40 complex into the IMS and TIM23 complex into the matrix. In the matrix, the pre-sequence is removed by MPP, and the protein can fold into its mature state.*

1.3.2 Import into the intermembrane space

In yeast, 51 mitochondrial proteins are found in the IMS (53 in mammals) (Rath et al., 2021). All of these proteins are nuclear-encoded and must be imported into the mitochondria. The main and most well-defined pathways for IMS import include the Mia40 import pathway and the stop-transfer pathway. It should be noted that unconventional, and to some extent much less characterised, IMS

import pathways have been identified and are utilised by proteins such as cytochrome c and cytochrome c haem lyase (Edwards, Eaglesfield and Tokatlidis, 2021).

1.3.2.1 The Mia40 import pathway

Precursors targeted to the IMS via the Mia40 import pathway harbour characteristic cysteine-rich motifs (most often Cx_3C or Cx_9C) and typically have a molecular weight of <20 kDa (Gabriel et a., 2007). Mia40 substrates do not possess an N-terminal MTS, but rather harbour internal targeting information which directs said proteins through the Mia40 pathway. These targeting sequences are known as mitochondrial intermembrane space sorting signals (MISS) or IMS targeting signals (ITS) and consist of 9 amino acids which form an amphipathic helix (Milenkovic et al., 2009).

To initiate mitochondrial import, as shown in **fig. 1.5**, Mia40 substrates are translocated across the OMM via the TOM complex in a Tom receptor-independent manner (Vögtle et al., 2012; Mordas and Tokatlidis, 2015). Substrates must be reduced and unfolded for translocation. The cryo-EM structure of the TOM complex revealed an interaction between the most N-terminal alpha-helix of Tom40 and Tom5, which was subsequently shown to be a requirement for efficient import of Mia40 substrates (Araiso et al., 2019). The first encounter with the MIA machinery comes after TOM translocation.

The two main components of Mia40 import machinery are Erv1 (ALR in mammals) and Mia40 itself (CHCHD4 in mammals). The latter is an oxidoreductase which is anchored to the IM and is IMS-facing. The former is a soluble FAD-binding sulfhydryl oxidase localised to the IMS (Mesecke et al., 2005; Wiedemann and Pfanner, 2017). Precursors interact first with Mia40 via a ‘sliding-docking model’ as they exit the TOM channel (Sideris et al., 2009). First, the MISS/ITS of precursors interacts with the hydrophobic cleft of Mia40 via non-covalent interactions (sliding step). This orientates the precursor appropriately to facilitate the interaction with the Mia40 cysteine-proline-cysteine (CPC) motif. Specifically, the ‘docking’ cysteine residue of the precursor and the second

cysteine of CPC form a transient intermolecular disulfide bond (docking step). Via subsequent nucleophilic attack of the intermolecular disulfide, an intramolecular disulfide bond forms within the precursor protein. The protein can then fold correctly and is released into the IMS (Kawano et al., 2009; Mordas and Tokatlidis, 2015).

To complete the MIA pathway, the CPC motif of Mia40 must be re-oxidised by Erv1 to allow Mia to interact with further substrates. Re-oxidation occurs via collaboration of Mia40 and Erv1 in a disulfide relay system in the IMS. Briefly, Erv1 binds Mia40 at its hydrophobic binding cleft. Erv1 then accepts electrons from Mia40, leaving Mia40 in the oxidised state and free to bind another substrate (Mesecke et al., 2005; Edwards, Eaglesfield and Tokatlidis, 2021). Erv1 itself must be re-oxidised, which is achieved via the shuttling of electrons to cytochrome C and subsequently cytochrome C oxidase (Allen et al., 2005). Alternatively, electrons can be shuttled directly to molecular oxygen in the IMS for Erv1 re-oxidation (Bihlmaier et al., 2007). Thus, in this manner, the Mia40 and Erv1 collaboration is essential for import and folding of Mia40 substrates. Proteins which are imported into the IMS via MIA include the small Tims (Tim8, Tim9, Tim10, Tim13) and other small proteins such as COXIV assembly factor Cox19 (Sideris et al., 2009).

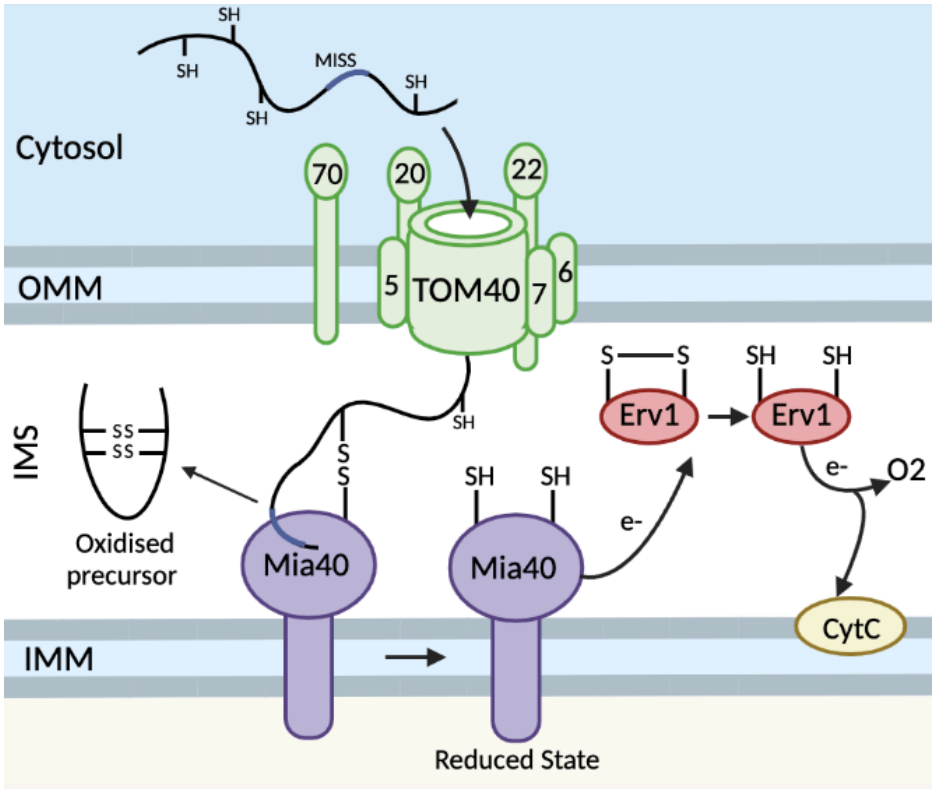

Fig. 1.5: The Mia40 pathway for import into the IMS. *Cys-rich precursor containing MISS/ITS passes through TOM40 complex and enters IMS where it interacts with Mia40 to facilitate import and folding. Erv1 re-oxidises Mia40 and is re-oxidised itself via a disulphide relay system. -SH indicates free sulfhydryl groups whereas S-S indicates presence of a disulfide bond. Arrows designated e- indicate the passage of electron shuttling.*

1.3.2.2 The stop-transfer import pathway

The transfer of precursors from the cytosol to the IMS may also be directed by the stop-transfer import pathway. In contrast to Mia40 substrates, precursors are targeted to the stop-transfer pathway via a bipartite signal. The bipartite signal is composed of two sequence regions: the first is a positively charged and cleavable amphipathic helix (pre-sequence) and the second is a strongly hydrophobic region (Edwards, Eaglesfield and Tokatlidis, 2021).

To initiate import, the pre-sequence interacts with Tom20 and Tom22 at their cytosolic domains (Araiso et al., 2019). Subsequently, the precursor enters the Tom40 channel and is translocated to the IMS. In the presence of the IMM potential, the precursor enters the channel of TIM23 following an interaction with Tim50. The transmembrane domain of the bipartite signal acts to halt translocation of the IMS precursor whilst in the Tim23 channel ('stop'). This prevents the precursor from passing through the channel and into the matrix. Next comes the 'transfer' component of the pathway, whereby it is believed that the precursor is laterally released from TIM23 and into the IMM (Glick et al., 1992). The pre-sequence region is now matrix-localised and will be removed via cleavage by MPP (Vögtle et al., 2012). Subsequently, proteases residing in the inner membrane (Imp1 and Imp2) cleave the precursor to remove the transmembrane signal (Esser et al., 2004; Kunová et al., 2022). Thus, releasing the mature IMS protein into the IMS where it can fold into its native state. This pathway is depicted in **fig. 1.6**. Various IMS proteins follow the stop-transfer pathway for import, including endonuclease G and cytochrome b2 (Glick et al., 1992; Ohsato et al., 2002). The stop-transfer pathway can also be utilised by IMM precursor proteins for membrane integration. In this case, the stop-transfer

pathway ceases after lateral integration of the protein into the IMM, and Imp1/2 proteins are not required (Glick et al., 1992; Park et al., 2013).

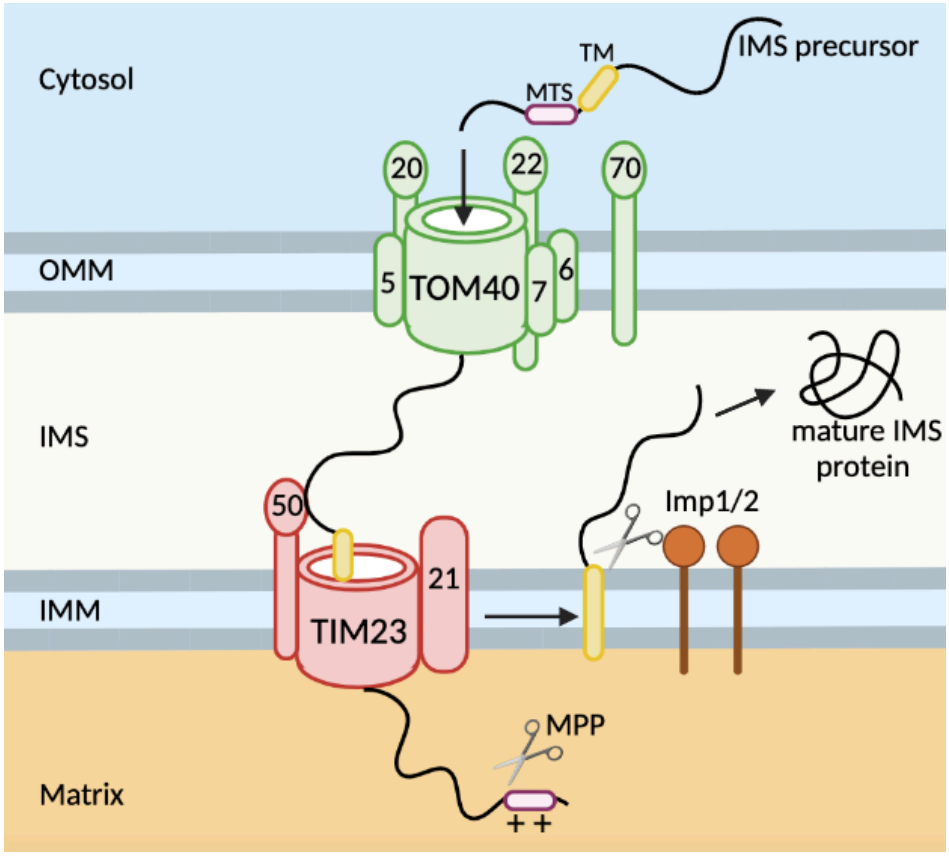

Fig. 1.6: The stop-transfer pathway for mitochondrial import. *Stop-transfer substrates possess a bipartite signal, comprised of a pre-sequence (labelled MTS and shown in pink) and a hydrophobic transmembrane segment (labelled TM and shown in yellow). MTS directs the precursor to TOM20 and into the IMS. The precursor then enters TIM23 until translocation is arrested by TM. MPP cleaves the pre-sequence. The precursor is released into the IM. IMM proteins are retained in the IMM whereas IMS proteins are cleaved by Imp1/2 for subsequent release into the IMS.*

1.3.3 Import into the outer mitochondrial membrane

There are two types of mitochondrial protein synthesised in the cytosol which must be targeted to and embedded into the OMM: α-helical proteins and β-barrel proteins. α-helical proteins are anchored to the membrane via

transmembrane helix(es) whereas β-barrel proteins traverse the membrane via transmembrane β-strands (Wiedemann and Neupert, 2017).

The most ubiquitous protein of the OMM is the β-barrel protein Porin which permits transfer of small molecules from the cytosol to the IMS (Krimmer et al., 2001). *S. cerevisiae* harbours two distinct porin isoforms (Por1 and Por2) whereas mammals harbour three (Young et al., 2007). To initiate import, β-barrel precursors first pass through the channel of the TOM40 complex and enter the IMS (**fig. 1.7**). Here, the small translocase of the inner membrane (TIM) chaperones are found, namely Tim9 and Tim10, which form a heterohexameric complex (Webb et al., 2006; Weinhäupl et al., 2018). These Tim9-Tim10 complexes bind the exposed hydrophobic regions of the precursor, once again to protect from aggregation. Subsequently, the Tim9-Tim10 complex delivers the precursor to the sorting and assembly machinery (SAM) complex of the OMM, which is responsible for integration of β-barrel precursors into the outer membrane. The SAM complex is comprised of Sam35, Sam37 and Sam50 (Wiedemann et al., 2003). Sam37 promotes insertion of precursors into the SAM complex by binding Tom22, bringing SAM and TOM complexes into close proximity (Wenz et al., 2015). Sam50 forms a channel in the OM into which β-barrel precursors are inserted. A single β-strand of β-barrel precursors harbours a targeting sequence known as a β-signal. Recognition of the β-signal by Sam35/50 is believed to trigger the lateral release of β-barrel proteins from the Sam50 channel and into the lipid bilayer (Kutik et al., 2008; Höhr et al., 2015).

The import pathways of α-helical proteins are detailed in **fig. 1.7**. The pathway followed by each α-helical protein is dependent on the number of transmembrane helices harboured by said proteins. Signal-anchored α-helical proteins are those which are anchored to the OM via a single transmembrane helix at their N-terminal. Signal-anchored proteins are targeted to the OM via the mitochondrial import channel (MIM) complex (comprised of Mim1 and Mim2) (Becker et al., 2008). α-helical proteins harbouring several transmembrane helices also utilise MIM for import, yet this pathway differs in that Tom70 must first bind to the precursors for their subsequent delivery to MIM. Tail-anchored

(TA) α-helical proteins (proteins anchored to the OM via a single transmembrane helix at the C-terminus), such as Bcl2, have been identified in the OM (Chipuk et al., 2010). TA precursor import does not require the TOM40 complex, nor does it depend on any defined component of OM insertion machinery (Kemper et al., 2008). Thus, the mechanism for TA import remains largely unknown, but is thought to be driven by the ergosterol composition of the OM (Krumpe et al., 2012). Nonetheless, all helical proteins are believed to contain mitochondrial targeting information in their transmembrane domains, but a consensus sequence does not exist (Ellenrieder, Mårtensson and Becker, 2015).

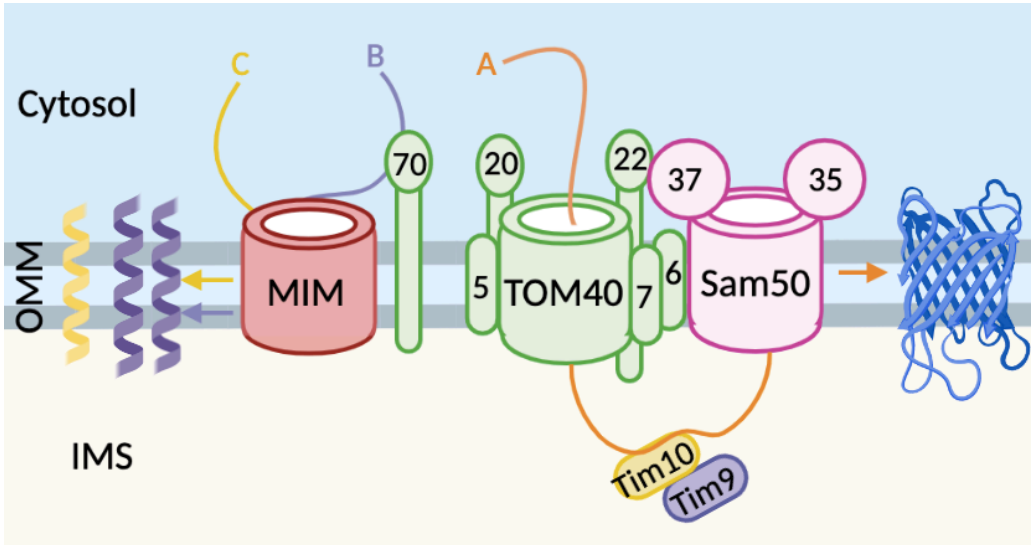

Fig. 1.7: Import pathways for the integration of α-helical and β-barrel proteins into the OM of mitochondria. *(A) Import of β-barrel precursors into the OMM. Precursor shown in orange. Proteins of the TOM40 complex are shown in green and proteins of the SAM complex are shown in pink. Sam35 and Sam37 are peripherally associated with the membrane. (B) Import of multi-spanning α-helical proteins into OMM via Tom70 and MIM complex (shown in red). Precursor and final helical membrane-integrated protein shown in purple. (C) Import of signal-anchored α-helical proteins into OMM via MIM complex. Precursor and membrane-embedded helix shown in yellow.*

1.3.4 Import into the inner membrane: The carrier import pathway

As aforementioned, precursors can be imported into the IMM via the stop-transfer pathway (**fig. 1.6**). However, various IMM precursors lack a pre-

sequence and thus cannot be targeted to mitochondria via stop-transfer (Luciano et al., 2001). Early studies demonstrated that said proteins follow a distinct import pathway and are likely targeted here via internal targeting information (within hydrophobic transmembrane domains) (Pfanner and Neupert, 1987; Ryan, Muller and Pfanner, 1999). This pathway was termed the 'carrier import pathway' as its substrates are primarily polytopic mitochondrial metabolite carriers which will be discussed in more detail in the following section.

The carrier import pathway will be described according to the operational staging mechanism originally defined by Ryan, Muller and Pfanner (1999). Foremost, chaperones Hsp70 and Hsp90 bind a carrier precursor in the cytosol to protect the highly hydrophobic, unfolded protein from aggregation (stage I). Bound chaperones deliver the precursor to Tom70, an OM receptor which harbours a binding site for the precursor and a distinct binding site for chaperones (Sha and Wu, 2006). ATP binding to chaperones results in their dissociation from the precursor and Tom70 (stage II). The precursor is transferred to Tom22, and from here is translocated through the Tom40 channel and into the IMS. Here, heterohexameric complexes of soluble small Tim chaperones (yeast Tim8/13 or Tim9/10, human Tim9/Tim10a) bind hydrophobic regions of the precursor (Webb et al., 2006). The Tim9/10 solution NMR structures revealed that binding of precursors occurs at a 'clamp-like' binding site and that a highly hydrophobic conserved motif was crucial for said interaction (Weinhäupl et al., 2018). The precursor is released from said binding site on soluble Tim chaperones to Tim chaperones (yeast Tim9-Tim10-Tim12 or human Tim9-Tim10a-Tim10b) associated with IMM-integrated TIM22 complex (stage III). The TIM22 complex is comprised of said Tim9-Tim10-Tim12 complex, Tim22, Tim54 and Tim18. Tim54 is IMS-facing and as such facilitates binding of Tim9-Tim10-Tim12 to TIM22 (Gebert et al., 2008). In the presence of $\Delta\Psi$, the carrier precursor is transferred into the channel of TIM23, created by Tim22, and is laterally integrated into the IMM (stage IV). The carrier pathway is depicted in **fig. 1.8**. The pathway is highly conserved in humans, the only differences being that Tim29 (rather than Tim54) binds Tim9a-Tim10a-Tim10b and acylglycerol kinase is required for TIM22 stability (Vukotic et al., 2017; Jackson et al., 2021).

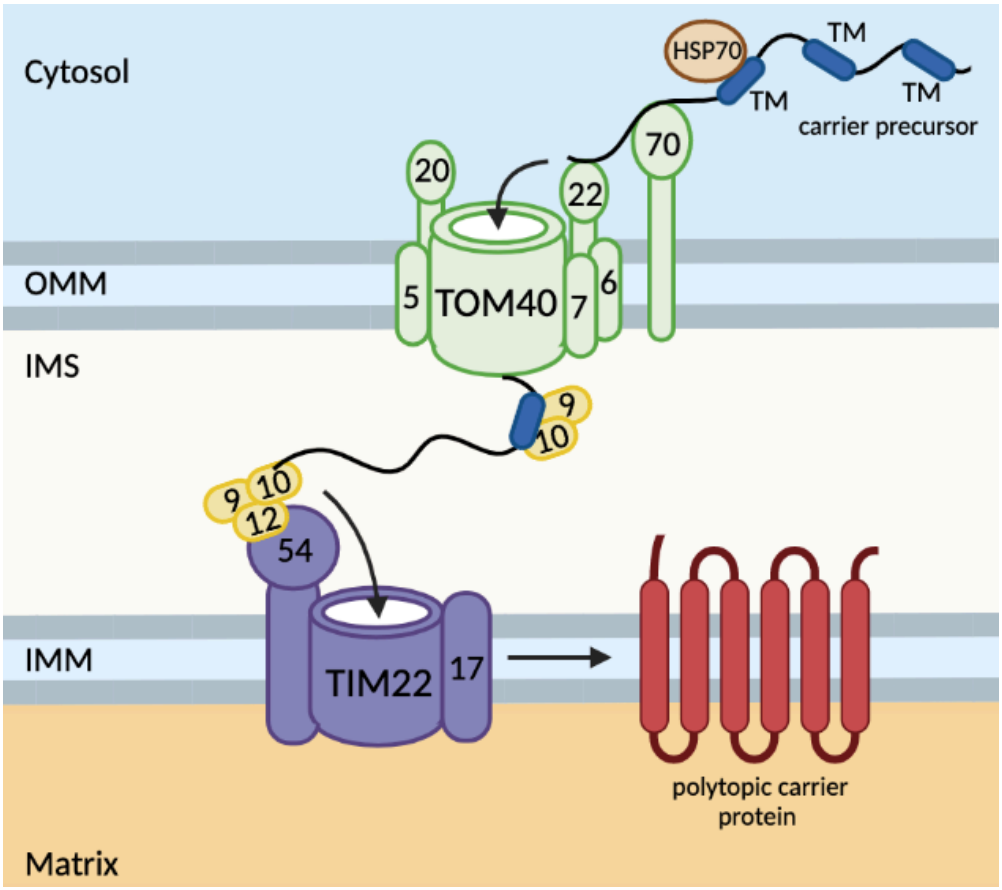

Fig. 1.8: The carrier pathway for import of IMM precursors into mitochondria. *The carrier precursor is shown in the cytosol with various transmembrane domains. The precursor is translocated across OM via TOM40 and bound by soluble Tim9/10 in the IMS. The precursor is transferred to TIM22-bound Tim9/10/12, enters the Tim22 channel and is integrated into the IMM.*

1.4 Substrates of the mitochondrial carrier pathway

The IMM is highly impermeable, ensuring the separation of IMS and matrix environments. However, various mitochondrial processes such as OXPHOS, Fe-S cluster biogenesis and heme biosynthesis are dependent upon the transport of small molecules between these two mitochondrial compartments (section 1.2). To permit transport across the IMM, mitochondria harbour numerous IMM metabolite carriers. Various metabolite carrier (often referred to as mitochondrial carriers, or MCs) families are imported via the carrier pathway and TIM22, with the most well-defined of these being SLC25 carriers, mitochondrial pyruvate carriers (MPC) and recently sideroflexins (SFXNs).

Substrates transported by MCs include amino acids, OXPHOS intermediates, ions and nucleotides (Cunningham and Rutter, 2020).

1.4.1 SLC25 carriers

The SLC25 (solute carrier family 25) carriers belong to the solute carrier protein (SLC) superfamily and are the largest family of MCs, with the human genome encoding 53 SLC25 members and the yeast genome encoding ~30 (Ruprecht and Kunji, 2019). To be defined as a member of the SLC25 family, carriers must possess specific structural and sequence elements. For instance, all SLC25 members possess six transmembrane helices arranged as three repeats of a helix-loop-helix domain which are each approximately 100 amino acids in length (**fig. 1.9**). This structural arrangement has led to SLC25s often being described as having a tripartite structure (Saraste and Walker, 1982). In addition, each odd-numbered helix of an SLC25 carrier harbours a highly conserved signature motif (PX[D/E]XX[K/R]) (Pebay-Peyroula et al., 2003; Kunji et al., 2016).This motif is key for the transporter function of SLC25s. For instance, the proline residues introduce a kink into helices to allow said helices to interact via formation of salt bridges. This acts to close the pore of the transporter such that substrates cannot pass (Pebay-Peyroula et al., 2003). Moreover, SLC25 carriers follow the same orientation at the IMM, with both the N- and C-termini extend into the IMS (Ruprecht and Kunji, 2019) (**fig. 1.9**).

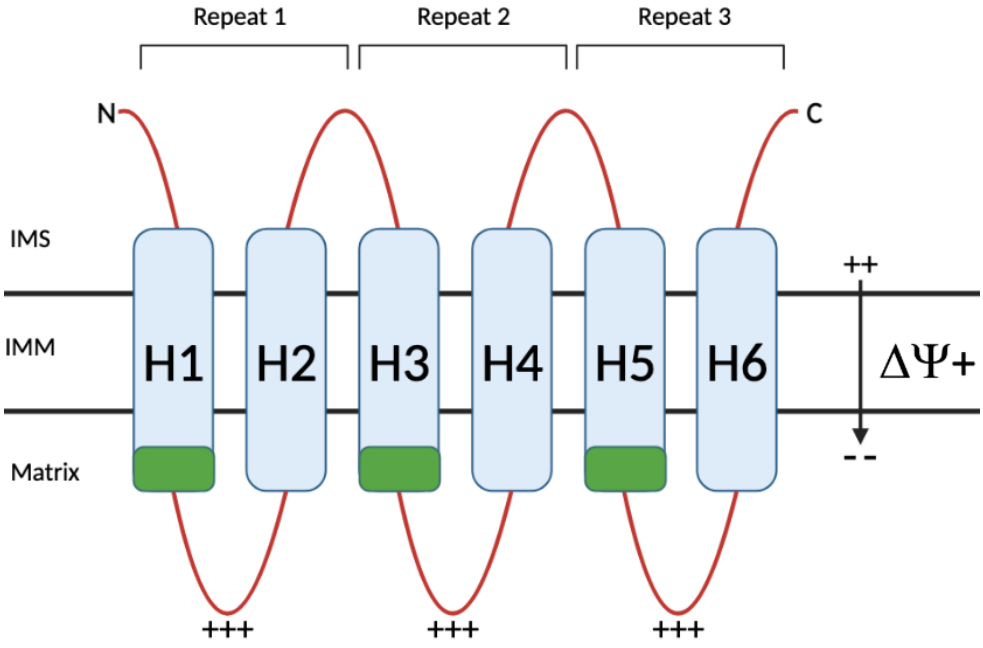

Fig. 1.9: Tripartite structure of an SCL25 carrier. *Helices 1-6 are labelled H1-H6. Green boxes on odd-numbered helices indicate the position of the conserved signature carrier motif.*

There is no consensus sequence for the targeting of SLC25 carriers to the IMM. However, numerous studies have identified targeting information in the transmembrane domains of SLC25s (Wiedemann, Pfanner and Ryan, 2001; Vergnolle et al., 2002; Vaseljev et al., 2004; Kunji et al., 2016). Additionally, it is known that SLC25 carriers are inserted into TOM40 one helix-loop-helix domain at a time (Wiedemann, Pfanner and Ryan, 2001). Further, matrix-localised loops of SLC25 carriers carry a greater overall positive net charge than IMS-localised loops. Under the IMM potential, these positively charged loops are driven into the matrix via an electrophoretic force. Thus, this feature is too essential for import (Horten, Colina-Tenorio and Rampelt, 2020). Examples of mammalian SLC25 carriers include the ADP/ATP carrier (AAC), SLC25A42 (CoA transporter for alpha-ketoglutarate dehydrogenase-catalysed step of the TCA cycle) and mitoferrin-1/2 (iron transporters involved in heme/Fe-S biosynthesis) (Pebay-Peyroula et al., 2003; Paw et al., 2006; Almannai et al., 2018).

1.4.2 Mitochondrial pyruvate carriers

Over time, more and more multi-span IM proteins have been identified which transport metabolites across the IMM but show distinct characteristics relative to the SLC25 family. For instance, transmembrane proteins MPC1 and MPC2 are TIM22 substrates possessed by both mammals and yeast which form a heterodimer at the IMM to facilitate pyruvate transport (Herzig et al., 2012; Bender, Pena and Martinou, 2015; Cunningham and Rutter, 2020). Contrasting from the 6-transmembrane structure of SLC25 carriers, MPC1 harbours two transmembrane helices, showing matrix-localisation of the N- and C-termini. In contrast, MPC2 is believed to possess three transmembrane helices (Bender, Pena and Martinou, 2015) (**fig. 1.10**). Due to this clear structural difference, MPC1/2 are classed as a family of their own – designated SLC54.

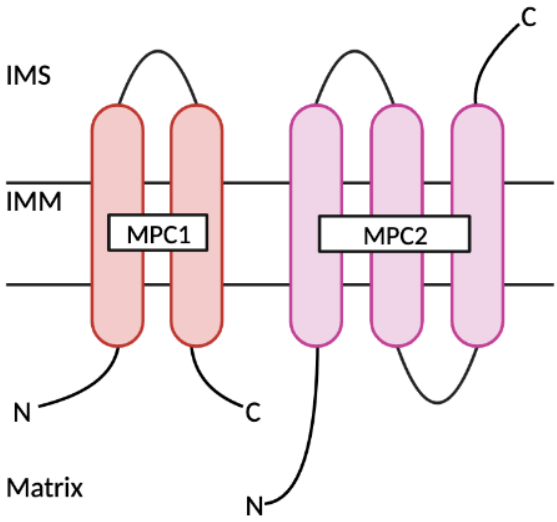

Fig. 1.10: Structure of MPCs. *Structure of MPC1 shown in red. Structure of MPC2 shown in pink. N- and C-termini labelled.*

1.4.3 The TIM22 complex is responsible for the integration of Tim17, Tim22 and Tim23 into the IMM

The carrier pathway and TIM22 are not solely utilised by MCs. Yeast import machinery components Tim17, Tim22 and Tim23 are themselves imported via TIM22 (Káldi et al., 1998). The structure of said Tims differs from all previously defined carrier families, with each Tim being comprised of four transmembrane domains and having IMS-facing N- and C-termini (Chaudhuri et al., 2020). Tim17/22/23 do not possess an N-terminal pre-sequence and rather are targeted to mitochondria via internal signals (within both transmembrane and loop regions of the protein structure) (Kaldi et al., 1998). Similar to SLC25s, the overall positive net charge of matrix-localised loops is a requirement for import of these Tims (Davis et al., 2007). Evidently, there is a high degree of diversity not only amongst MCs, but amongst TIM22 substrates.

1.5 Sideroflexins: a unique family of carrier proteins

SFXNs are a more recently identified family of MCs. SFXNs were initially discovered when a frameshift mutation in *SFXN1* was found to be responsible for the mitochondrial iron overload phenotype of sideroblastic anaemia in *flexed-tail (f)* mice (Fleming et al., 2001). SFXNs were named based on this discovery,

taking ‘sidero-’ from sideroblastic anaemia and ‘-flexin’ from flexed-tail. Following discovery of SFXN1, four homologs were identified in rodents – bringing the total number of SFXN family members to five (named SFXN1-5). Numerous SFXN homologs have since been identified across species: SFXN1-5 in humans and xenopus, fungal sideroflexin-1 (FSF1) *in S. cerevisiae* and dSFXN1/2 and SFXN2 in *Drosophila* (Tifoun et al., 2021). Sequence analysis has shown that SFXN sequences are highly conserved across eukaryotes (Miotto et al., 2007; Kory et al., 2018).

1.5.1 Classification of mammalian SFXNs as mitochondrial carriers

Mammalian SFXNs were classified as MCs based on their localisation, mitochondrial targeting and structure. To focus first on localisation, SFXN family members were found to localise to the mitochondria *in vivo* through use of confocal microscopy (Fleming et al., 2001; Miyake et al., 2002; Rivell et al., 2019; Mon et al., 2019). Specifically, SFXN1, SFXN3, SFXN4 and SFXN5 integrate into the IMM (Paul et al., 2019; Acoba et al.,2021 Ledahawsky et al., 2022; Jackson et al., 2022). In contrast, SFXN2 localisation has been disputed – with studies showing both OMM and IMM localisation (Mon et al., 2019; Jackson et al., 2021). Nonetheless, all SFXNs are thought to be targeted to the IMM via TIM22 and the carrier pathway (Jackson et al., 2021; Ledahawsky et al., 2022). To achieve such mitochondrial localisation, SFXNs inevitably should harbour some form of mitochondrial targeting sequences. As reigns true for TIM22 substrates, SFXNs are believed to possess internal targeting information, yet no study has been yet reported to seek to uncover these precise signals.

SFXN structure is predicted to consist of various TMs. Whilst studies have predicted that each SFXN traverses the IMM via four or five TMs, no study has confirmed this *in vitro* (Fleming et al., 2001; Lockhart et al., 2002; Miyake et al., 2002; Miotto et al., 2007; Kory et al., 2018; Mon et al., 2019; Acoba et al., 2021).

1.5.2 The function of mammalian SFXNs

As an IMM protein, the role of mammalian SFXNs in mitochondrial respiration and more specifically, OXPHOS, have inevitably been studied. From the research currently available, only SFXN4 shows a clear link to respiration as a potential complex I assembly factor (Hildick-Smith et al., 2013; Paul et al., 2019; Jackson et al., 2022). The role of each additional mammalian SFXN in respiration is unclear and for SFXN3, unstudied (Amorim et al., 2017; Mon et al., 2019; Paul et al., 2019; Acoba et al., 2021).

It is estimated that the identity of the small molecule(s) transported by a third of mammalian MCs are yet to be uncovered (Ruprecht and Kunji, 2019). Originally, based on the TM structure and sideroblastic anaemia phenotype described in section 1.5, it was hypothesised that SFXNs could be iron transporters (Fleming et al., 2001). However, this hypothesis has never been proven and is widely disputed. Said disputes originated from the fact that many researchers believe that mutation in Madh5 (rather than SFXN1) is responsible for the anaemic phenotype of f/f mice (Lenox, Perry and Paulson, 2005). Nonetheless, in recent years, loss of SFXN2 and SFXN4 have both independently been shown to stimulate mitochondrial iron accumulation in cell lines (Mon et al., 2019; Paul et al., 2019; Tifoun et al., 2022; Chen et al., 2022). Therefore, a role for SFXNs in iron homeostasis is still plausible.

The ability of mammalian SFXNs to transport various other substrates, such as citrate and pyridoxine, has been disproven (Yoshikumi et al., 2005; Kory et al., 2018). The lack of success in defining the substrate of SFXNs led researchers to pursue other avenues, which ultimately led to the identification of SFXN1 as a serine transporter which translocates serine into the matrix for one-carbon (1C) metabolism (Kory et al., 2018). 1C-metabolism is essential in generating one-carbon units for use in processes such as thymidine biosynthesis and synthesis of nucleotides (Ducker and Rabinowitz, 2017). Serine transport appears to be a function conserved amongst SFXNs, with the exception of SFXN4 and SFXN5 (Kory et al., 2018). To date, the Kory et al. (2018) study is the sole investigation which demonstrates the ability of a mammalian SFXN to transport a substrate *in vitro*.

1.5.3 Spotlight on SFXN3: an SFXN implicated in neurodegenerative disorders

In recent years, there has been a surge in interest surrounding sideroflexin-3 (SFXN3). This is likely attributable to the fact that SFXN3 is highly expressed in the brain and inversely regulated by α-synuclein, a neuronal protein associated with Parkinson's disease (PD) due to its aggregation in Lewy bodies (Amorim et al., 2017; Rivell et al., 2019). α-synuclein is predominantly localised to presynaptic terminals, and its overexpression can stimulate a decline in the release of neurotransmitters and alterations in synaptic vesicle morphology, contributing to neurotoxicity (Nemani et al., 2010). There is interest in therapeutically targeting α-synuclein, but this is difficult due to the dynamic nature of the protein. Therefore, it was proposed that SFXN3 could be a feasible target in PD (Amorim et al., 2017). Additionally, the loss of dopaminergic neurons in two PD fly models could be rescued by increasing levels of SFXN3 expression (Ledahawsky et al., 2022). It is possible that this neuroprotective role of SFXN3 stems from its influence on synapse formation, as SFXN3 loss impaired ability to form synapses in the eye of SFXN3-deficient mice (Chen et al., 2020).

Whilst a link to neurodegeneration is evident, it must be acknowledged that SFXN3 has also been implicated in further diseases and disorders. For instance, a role for SFXN3 in cancer development has recently come to light. Upregulation of SFXN3 expression was identified in head and neck squamous cell carcinoma and may promote cancer progression by contributing towards chemotherapy drug resistance and impairing activity of T-cells (Chen et al., 2022). Strengthening the link to cancer, the SFXN3 sequence harbours sites to which Myc (an oncogene) can bind (Kory et al., 2018). As aforementioned, SFXN3 can compensate for the loss of SFXN1 in terms of serine transport (Kory et al., 2018). Serine metabolism is crucial for the growth of cancer cells, thus perhaps SFXN3 links to cancer via its role in serine transport (Amelio et al., 2017; Kory et al., 2018). However, evidence for the ability of SFXN3 to transport serine *in vitro* has not yet been provided. Finally, SFXN3 has been linked to diabetes, with enhanced SFXN3 levels being seen in rodent models of diabetes and said increased expression supposedly occurring to promote islet regeneration (Yoshikumi et al., 2005). However, to date no studies have further elucidated how SFXN3 contributes to such a process.

Chapter 2: Aims

Recent advances in the sideroflexin field have uncovered the mitochondrial localisation of SFXNs and proposed a function in serine transport. Being the sole SFXN linked to neurodegeneration and a downstream target of α-synuclein, SFXN3 is of current interest. However, the precise structure, mitochondrial targeting, and breadth of functions of SFXN3 remain unknown. The following aims were constructed to address these unknowns.

Chapter 4 - *In silico analysis of the structure and sequence of human SFXN3*

The aim of chapter 4 was to predict the TM structure and N- and C-termini orientation of human SFXN3 to better understand the structure of the protein at the IMM. Structure predictions can be used to inform study of the three-dimensional structure of the protein, which is greatly informative in structure-based drug design.

Chapter 5 - *Investigating the mitochondrial targeting of human SFXN3*

The aim of chapter 5 was to identify mitochondrial targeting information of SFXN3. As the project progressed, an additional aim was proposed to specifically identify the sequences of SFXN3 required for interaction with Tim9/10. This will provide a more complete overview of the SFXN3 mitochondrial import pathway, which is crucial for understanding protein assembly, insertion and folding.

Chapter 6 - *Characterising the function of human SFXN3 and S. cerevisiae FSF1*

The initial aim of chapter 6 was to knockdown (KD) SFXN3 expression in HEK293 cells to allow investigation of SFXN3 function. However, the aims shifted to characterising the function of *S. cerevisiae* FSF1. By elucidating protein function, we can predict the potential downstream effects of manipulating SFXN3 activity/levels therapeutically.

Chapter 3: Materials and Methods

3.1 Materials

3.1.1 Antibodies

Primary and secondary antibodies used in this study are listed in **table 3.1.** To achieve the desired concentration, primary antibodies were diluted in 5% (w/v) milk in TBST (1X Tris-buffered saline, 0.1% (v/v) Tween® 20 detergent). For fluorescent Western blot detection, secondary antibodies were diluted in TBST. For chemiluminescent Western blot detection, secondary antibodies were diluted in 5% (w/v) milk in TBST.

Table 3.1: List of antibodies used in this study.

Antibody	Species Origin	Company	Species raised in	Conc.	Source
a-AAC	Yeast	Davids Biotechnologie	Rabbit Polyclonal	1:500	Tokatlidis Lab
a-Aconitase	Yeast	Davids Biotechnologie	Rabbit Polyclonal	1:10000	Tokatlidis Lab
a-Cox4	Yeast	Cell Signal	Rabbit Polyclonal	1:500	Tokatlidis Lab
a-Histidine	Synthetic histidine peptide	Bio-Rad	Mouse Monoclonal	1:500	Purchased from Bio-Rad
a-Hsp70	Yeast	Davids Biotechnologie	Rabbit Polyclonal	1:10000	Gifted by Professor Nikolaus Pfanner
a-Mia40	Yeast	Davids Biotechnologie	Rabbit Polyclonal	1:1000	Sideris et al., 2009
a-Mouse IgG DyLight 800CW	Mouse	Invitrogen	Goat Polyclonal	1:10000	Purchased from Invitrogen

a-Mouse IgG HRP	Mouse	Sigma Aldrich	Goat Polyclonal	1:10000	Purchased from Sigma Aldrich
a-mtHSP70	Human	Davids Biotechnologie	Mouse Polyclonal	1:10000	Tokatlidis Lab
a-Porin1	Yeast	Davids Biotechnologie	Rabbit Polyclonal	1:10000	Gifted by Professor Nikolaus Pfanner
a-Rabbit IgG DyLight 680	Rabbit	Invitrogen	Goat Polyclonal	1:10000	Purchased from Invitrogen
a-Rabbit IgG HRP	Rabbit	Sigma Aldrich	Goat Polyclonal	1:10000	Purchased from Sigma Aldrich
a-Sam35	Yeast	Schatz Lab Collection	Rabbit Polyclonal	1:1000	Schatz Lab Collection
a-SFXN3	Human	Atlas Antibodies	Rabbit Polyclonal	1:500	Purchased from Atlas Antibodies
a-Tim10	Yeast	Davids Biotechnologie	Rabbit Polyclonal	1:500	Tokatlidis Lab
a-Tom40	Yeast	Davids Biotechnologie	Rabbit Polyclonal	1:1,000	Tokatlidis Lab

3.1.2 Plasmids

Plasmids used in this study are detailed in **table 3.2**.

Table 3.2: List of plasmids used in this study.

Insert	Plasmid	Source	Use
FSF1	pSP64-FSF1	Tokatlidis Lab	T_NT Coupled Transcription/Translation

SFXN3 (full-length protein)	pSP64-SFXN3	Tokatlidis Lab	T_NT Coupled Transcription/Translation
	pLKO.1-puro-SFXN3	Sigma Aldrich (Merck)	shRNA knockdown of SFXN3 in HEK293 cells, contains puromycin-resistant (puroR) gene for selection
SFXN3 N-terminal	pSP64-SFXN3 NT	This study	T_NT Coupled Transcription/Translation
SFXN3 N-terminal to TM1	pSP64-SFXN3 T1	This study	T_NT Coupled Transcription/Translation
SFXN3 N-terminal to TM2	pSP64-SFXN3 T2	This study	T_NT Coupled Transcription/Translation
SFXN3 N-terminal to TM3	pSP64-SFXN3 T3	This study	T_NT Coupled Transcription/Translation
SFXN3 N-terminal to TM4	pSP64-SFXN3 T4	This study	T_NT Coupled Transcription/Translation
Tim9 (6xHis-tagged)	pET28	Tokatlidis Lab	Protein Expression and Purification
Tim10 (6xHis-tagged)	pRSET	Tokatlidis Lab	Protein Expression and Purification

3.1.3 Primers

Primer stocks were purchased from Sigma-Aldrich. Primers were resuspended in nuclease-free water to achieve a concentration of 100 μM and were subsequently stored at -20°C. The list of primers used in this study are shown in **table 3.3**.

Table 3.3: Primers used in this study and description of their use. *Primers were used to amplify truncations of the SFXN3 sequence from the pSP64 vector containing the SFXN3 gene (pSP64-SFXN3), originally cloned in the Tokatlidis lab. As each truncation was designed for use in in vitro ^{35}S-radiolabelled translation experiments, three additional methionine residues were added to the forward primer (shown in bold) before the stop codon (underlined).*

Primer Name	Primer Sequence (5' – 3' orientation)	Use
FRW_SFXN3_ECOR1	CAGTGAATTC**ATGATGATG**TGAAATTCGTAATCATGTCATAGCTGTTTCCTGTGTG	Forward primer to amplify pSP64 of pSP64-SFXN3
REV_SFXN3NT_ECOR1	CAGTGAATTCGCCTCACAGTGATGGGAGTGTC	Reverse primer to amplify residues 1-144 of SFXN3 within the pSP64-SFXN3 vector
REV_SFXN3T1_ECOR1	CAGTGAATTCCAAGGGGGGCAAGTGCTTGGTG	Reverse primer to amplify residues 1-174 of SFXN3 within the pSP64-SFXN3 vector
REV_SFXN3T2_ECOR1	CAGTGAATTCGCCCACCTGCAGCTCTCTCT	Reverse primer to amplify residues 1-203 of SFXN3 within the

		pSP64-SFXN3 vector
REV_SFXN3T3_ ECOR1	CAGTGAATTCCAGGAAGTCTTTCTTCTCCAGAG TGTCC	Reverse primer to amplify residues 1-256 of SFXN3 within the pSP64-SFXN3 vector
REV_SFXN3T4_ ECOR1	CAGTGAATTCGTTGCTTATGTGTATGGAGCTCT TCTGG	Reverse primer to amplify residues 1-296 of SFXN3 within the pSP64-SFXN3 vector

Primer sequences from failed cloning attempts are detailed in **appendix table 1**.

3.1.4 Bacterial strains and media

For transformation with plasmid DNA during cloning, DH5α *Escherichia coli* (*E. coli*) cells were used. BL21 (DE3) *E. coli* cells were used for recombinant protein expression. All *E. coli* cells were grown at 37°C in liquid Luria-Bertani (LB) media (1% (w/v) bactotryptone, 0.5% (w/v) yeast extract, 1% (w/v) NaCl) or on LB agar (prepared by adding 2% (w/v) agar to liquid LB). Kanamycin (30 μg/μL) or ampicillin (100 μg/μL) was added to the media to select for bacteria successfully transformed with plasmids expressing the corresponding antibiotic resistance genes. All media was sterilised by autoclaving at 121°C for 15 minutes.

3.1.5 Mammalian cells and media

HeLa cells were used for RNA isolation. HEK293 cells were used for shRNA transfection. HeLa and Hek293 cells were grown in Dulbecco's Modified Eagle Medium (DMEM) (Gibco) supplemented with 10% (v/v) foetal bovine serum (FBS), 100 IU/ml penicillin/streptomycin and 2 mM L-glutamine. Selective media (DMEM supplemented with 1 μg/mL puromycin) was used for selection of shRNA transfected HEK293 cells. All mammalian cells were grown at 37°C in a 5% CO_2 humidified atmosphere.

3.1.6 Yeast strains

Saccharomyces cerevisiae (*S. cerevisiae*) strains used in this study are detailed in **table 3.4**.

Table 3.4: List of yeast strains used in this study.

Strain	Genotype	Description	Source
D273-10B	MATα mal	Wild-type yeast strain, used for isolation of mitochondria	Sherman, 1964
BY4741	MATα his3Δ1, leu2Δ0, met15Δ0, ura3Δ0.	Wild-type yeast derived from S288C strain, used for comparison to ΔFSF1 yeast strain	Brachmann et al., 1998
ΔFSF1	MATα his3Δ1, leu2Δ0, met15Δ0, ura3Δ0 FSF1Δ0.	FSF1 knockout in BY4741 background	Horizon Discovery Yeast Knockout Collection

3.2 Methods

3.2.1 Molecular Biology Assays

3.2.1.1 RNA isolation from HeLa cells

HeLa cells were grown in DMEM (10% (v/v) FBS, 2 mM glutamine, 100 U penicillin/0.1 mg/mL streptomycin) (Gibco) in a T75 cell culture flask. Once cells were 80-90% confluent, the DMEM was removed. The cells were then detached from the surface of the flask by adding 1 mL trypsin EDTA and incubating the flask at 37°C for ~3 minutes (trypsinisation). Subsequently, 9 mL DMEM was added to neutralise the trypsin. The solution was transferred to a 15 mL falcon and cells were pelleted via centrifugation at 500g for 5 minutes. Subsequently, RNA was isolated from the cells using TRIzol™ reagent and the accompanying Invitrogen protocol. RNA was stored at -80°C until required for cDNA synthesis.

3.2.1.2 cDNA synthesis

cDNA was synthesised from RNA through reverse transcription, using the Agilent AffinityScript cDNA Synthesis Kit and protocol. The Agilent oligo(dT) primer (0.5 μg/μL) was used to direct cDNA synthesis. cDNA was stored at -20°C until required for PCR reactions.

3.2.1.3 Plasmid DNA purification

To isolate plasmid DNA from bacteria, the QIAprep Spin Miniprep Kit (QIAGEN) and protocol were used. Plasmids were stored at -20°C until use.

3.2.1.4 Polymerase chain reaction (PCR)

Genes of interest were amplified through PCR using primers described in **table 3.3** and **appendix table 1**. The composition of the PCR reaction mix used is shown below:

- 5 μL cDNA or plasmid DNA (arbitrary conc.)
- 5X Q5 Reaction Buffer (NEB)
- 2 mM dNTPs (NEB)
- 10 μM Forward Primer
- 10 μM Reverse Primer
- 5X Q5 High GC Enhancer (NEB)

- Q5 High-Fidelity DNA Polymerase (NEB)
- Nuclease-free water to a volume of 100 μL

The reaction mix was added to the T3 thermocycler, which heated the mix to 95°C for 2 minutes to begin denaturation of dsDNA. The thermocycler then ran 35 PCR cycles, whereby one cycle consisted of:

1. Denaturation at 95°C for 30 seconds
2. Annealing at the optimal primer pair annealing temperature for 1 minute
3. Extension at 72°C for 20-30 seconds per kilobase of DNA to be amplified

After the 35th cycle, a final long extension at 72°C was performed for 10 minutes.

3.2.1.5 Agarose gel electrophoresis

To confirm that target sequences had been successfully amplified, PCR products were separated by agarose gel electrophoresis (1% w/v agarose, 1X TAE buffer, 0.1X SYBR® safe) for 45 minutes at 90 V. The samples were run alongside a 1 kB DNA ladder (Promega) to permit size estimation of amplicons. Subsequently, a UV transilluminator was used to visualise the gel.

3.2.1.6 PCR clean-up

Following agarose gel electrophoresis, the QiaQuick PCR purification kit (QIAGEN) was used to clean-up PCR products. DNA concentration of cleaned-up products was measured using a NanoDrop Spectrophotometer (Thermo Fisher).

3.2.1.7 Restriction digest and ligation

Purified plasmids and inserts generated via PCR (section 3.2.1.4) were digested by two different NEB restriction enzymes for 1 hour at 37°C. To check the success of restriction digest, digested and undigested plasmid were separated by

agarose gel electrophoresis as detailed in section 3.2.1.5. Subsequently, a scalpel was used to extract the plasmid from the gel. The QiaQuick gel extraction kit and protocol (Qiagen) were then used to clean-up all digested products. DNA concentration was measured on a NanoDrop Spectrophotometer (Thermo Fisher).

Ligation of the digested insert and plasmid was performed by incubation with T4 DNA ligase (NEB) overnight at 16°C. A 1:7 vector to insert ratio was used. The quantity of insert required to achieve this ratio, when using 100ng plasmid DNA, was calculated using the following equation:

$$Ng\ of\ insert = \frac{ng\ of\ vector\ (100\ ng)}{vector\ (kbp)}\ x\ ratio\ (1:7)\ x\ insert\ size\ (kbp)$$

3.2.1.8 Single-restriction digest cloning

As an alternative means of cloning to generate fragments of a full-length gene, the vector containing the full-length gene was used as a template for PCR amplification. Primers used to generate said fragments are detailed in **table 3.3.**

Following PCR amplification, the plasmid was digested using a single restriction enzyme (at 37°C for 1 hour) to generate complementary ends for ligating the plasmid back together, excluding the undesired regions of the gene. Digestion products were cleaned up using the QiaQuick gel extraction kit (Qiagen), excluding the initial gel extraction step from the corresponding protocol. The DNA concentration of samples was measured using a NanoDrop Spectrophotometer (Thermo Fisher).

For ligation, approximately 200 ng of plasmid DNA was incubated with T4 DNA ligase (NEB) overnight at 16°C.

3.2.1.9 Preparation of competent cells

Competent cells were prepared using rubidium chloride, as described in the Promega Protocols and Applications Guide (3rd Edition).

3.2.1.10 Bacterial transformation

Ligation products were incubated with competent DH5α *E. coli* cells for 30 minutes on ice. Subsequently, cells were subjected to a 45 second heat shock at 42°C. Following heat shock, the cells were grown in LB, with shaking (170 rpm), at 37°C for 45 minutes. The transformed cells were then pelleted by centrifugation for 1 minute at 13000 rpm. Pellets were resuspended in LB and spread on LB agar plates containing the appropriate antibiotic. Plates were incubated at 37°C overnight.

3.2.1.11 Colony PCR

To confirm the presence of the insert in the plasmid, transformants were added to the PCR reaction detailed in section 3.2.1.4. The initial 2-minute denaturation at 95°C lyses the bacteria, releasing the plasmid DNA for use as the PCR template. Primers used in colony PCR were those originally used to amplify each insert ('insert-specific' primers). Subsequently, the presence of the insert was verified through agarose gel electrophoresis, as described in section 3.2.1.5.

3.2.1.12 Sequencing

Plasmid DNA samples were sent to Eurofins Genomics for sequencing of inserts. To confirm success of cloning, sequencing results were input into bioinformatics platforms CLC Genomics Workbench 20 and nucleotide BLAST for alignment to the desired sequence. To translate the nucleotide sequence of the insert to a protein sequence for further analysis, bioinformatics tool Expasy translate was used.

3.2.2 Biochemical Methods

3.2.2.1 SDS-PAGE

Tris-Tricine or Tris-Glycine SDS-PAGE was used to separate proteins by their molecular weight. Samples were resuspended in 2X Laemmli sample buffer (375 mM Tris-Cl pH 6.8, 40% v/v glycerol, 9% w/v SDS, 0.03% m/v bromophenol blue, 13 μL β-mercaptoethanol per 1 mL sample buffer) and then loaded into the wells of an SDS-PAGE gel. The gel was placed in a tank containing upper tricine buffer (100 mM Tris-HCl, 100 mM tricine, 0.1% w/v SDS – adjusted to pH 8.25) and lower tricine buffer (200 mM Tris-HCl – adjusted to pH 8.9). Tris-tricine gels were run at 120 V for 20 minutes, allowing proteins to pass through the stacking gel. Voltage was then increased to 150V, and the gel run for a further 90 minutes. Tris-glycine gels were run at 130V for approximately an hour. The components of tris-tricine and tris-glycine SDS-PAGE gels are shown in **table 3.5 and 3.6** respectively. Following SDS-PAGE, proteins were transferred from the gel to a nitrocellulose membrane for Western Blotting or the gel was Coomassie stained.

Table 3.5: Recipe for casting Tris-Tricine SDS-PAGE gels in 0.75mm plates

	3% Stacking Gel	**12% Separating Gel**
40% (v/v) Acryl/Bis-acryl	0.375 mL	3 mL
Tricine Gel Buffer	0.75 mL	3.3 mL
87% (v/v) Glycerol	-	1.3 mL
ddH20	1.82 mL	2.29 mL
10% (v/v) ammonium persulfate	50 μL	100 μL
TEMED	5 μL	10 μL
= total volume	3 mL	10 mL

Table 3.6: Recipe for casting Tris-Glycine SDS-PAGE gels in 0.75mm plates

	5% Stacking Gel	**12% Separating Gel**
30% (v/v) Acrylamide	0.67 mL	5 mL
1M Tris pH 6.8	0.5 mL	-
1.5M Tris pH 8.8	-	2.5 mL
10% (w/v) SDS	0.04 mL	0.1 mL

ddH20	2.7 mL	2.3 mL
10% (v/v) ammonium persulfate	0.1 mL	0.1 mL
TEMED	0.01 mL	0.01 mL
= total volume	4 mL	10 mL

3.2.2.2 Western blotting

The Bio-Rad semi-dry transfer system was used to transfer proteins from a gel to a nitrocellulose membrane. The nitrocellulose membrane, gel and Whatmann paper were each soaked in 1X transfer buffer (25 mM Tris, 190 mM glycine, 20% (v/v) methanol, 0.1% (w/v) SDS) and then placed in the transfer system such that the gel and membrane were sandwiched between Whatmann paper. Subsequently, the transfer was performed at 25V for 25 minutes. To confirm protein transfer, the membrane was stained using Ponceau-S (5% (v/v) acetic acid, 0.1% (w/v) ponceau stain). The stain was washed off using ddH_2O before proceeding with blocking.

To block non-specific binding, the nitrocellulose membrane was submerged in 5% (w/v) MilkFresh skimmed milk in 1X TBST (100 mM TRIS-HCl pH 7.4, 150 mM NaCl, 0.01% (v/v) Tween® 20 detergent) and gently shaken on a Stuart See-Saw rocker SSLA4 for an hour. The 5% (w/v) Milk TBST solution was removed, and the nitrocellulose membrane incubated in primary antibody solution overnight at 4°C. The following day, the membrane was washed in 1X TBST for 10 minutes at room temperature, with gentle rocking. The wash was repeated three times. The membrane was then incubated in secondary antibody solution at room temperature for an hour (for fluorescent detection) or 2 hours (for chemiluminescent detection), on the rocker. The membrane was washed three times, for 10 minutes each time, in 1X TBST or 1X TBS (100 mM TRIS-HCl pH 7.4, 150 mM NaCl) for fluorescent and chemiluminescent detection respectively. Fluorescent antibodies were visualised using the LI-COR odyssey CLX. HRP-conjugated antibodies were incubated with SuperSignal™ West Pico PLUS Chemiluminescent Substrate (Thermo Fisher) and visualised by using X-ray film and the Kodak X-OMAT processor.

3.2.2.3 Coomassie staining

If proteins were to be visualised after SDS-PAGE, the gel was incubated in Coomassie buffer (10% (v/v) acetic acid, 0.2% (w/v) Coomassie blue R-250, 30% (v/v) methanol) for 5 minutes, with gentle rocking. The Coomassie buffer was then removed, the gel rinsed with ddH_2O and de-stained by incubating in de-staining buffer (10% (v/v) acetic acid, 15% (v/v) methanol) for an hour, with shaking.

3.2.2.4 Recombinant protein expression

pET28 and pRSET plasmids containing genes detailed in **table 3.2** were transformed into BL21 (DE3) *E. coli* cells. Transformed cells were plated on LB agar plates containing kanamycin (for pET28) or ampicillin (for pRSET) and grown overnight at 37°C. Single transformed colonies from each plate were inoculated in 5 mL LB supplemented with the appropriate antibiotic and grown for ~6 hours at 37°C (with shaking). Subsequently, ~100 μL of the culture was added to a larger volume of LB (50 mL) with antibiotic and grown at 37°C overnight. The following day, the culture was added to 2 L of fresh LB with antibiotic and incubated at 37°C (with shaking) until OD_{600} of the culture reached ~0.8. At this point, 0.4 mM IPTG was added to induce protein expression and the culture incubated at 37°C for an hour. The culture was then moved to a 25°C incubator and left overnight. Cells were pelleted via centrifugation at 4000g for 10 minutes, in a JLA 8.1000 rotor, and stored at -20°C.

3.2.2.5 Histidine-tagged protein purification

Cell pellets prepared in section 3.2.2.4 were resuspended in buffer A (0.3 M NaCl, 0.05 M Tris pH 7.4, 10% (v/v) glycerol) and 0.2 M PMSF. To lyse the bacterial cell membrane, Lysozyme (1 mg/mL) was added, and two rounds of French press performed at a pressure of 750 PSI. Lysed cells were centrifuged at 21,000g for 34 minutes at 4°C to separate the soluble proteins (supernatant) and insoluble proteins (pellet) which aggregated into inclusion bodies. Proteins purified in this study were known to be present in the pellet, thus the supernatant was discarded.

To completely denature the inclusion bodies, pellets were resuspended in buffer B (0.15 M NaCl, 0.05 M Tris pH 7.4, 8 M Urea) and the solutions dounced. The solutions were incubated at room temperature for two hours (with shaking) and then centrifuged at 21,000g for 34 minutes at 20°C. Following the spin, the supernatant was retained as it should contain protein released from the inclusion bodies. The concentration of urea in the supernatant was adjusted to 6 M using Buffer AP (0.15 M NaCl, 0.05 M Tris pH 7.4) and the imidazole concentration adjusted to 5 mM. The supernatant was added to an 8 mL Ni-NTA column, which had been previously equilibrated using equilibration buffer P (0.15 M NaCl, 0.05 M Tris pH 7.4, 0.005 M Imidazole, 6 M urea). The column was washed firstly with wash buffer 1P (0.15 M NaCl, 0.05 M Tris pH 7.4, 0.015 M imidazole, 4 M urea), secondly with wash buffer 2P (0.15 M NaCl, 0.05 M Tris pH 7.4, 0.015 M imidazole, 2 M urea) and finally with wash buffer 3P (0.15 M NaCl, 0.05 M Tris pH 7.4, 0.015 M imidazole). After washing, elution buffer P (0.15 M NaCl, 0.05 M Tris pH 7.4, 0.25 M imidazole) was added to the column to elute the protein of interest. Small (~10 μL) samples were taken of the pellet of denatured inclusion bodies, the supernatant containing the protein, the flow-through after each wash and the elution. These samples were analysed via SDS-PAGE, and the gel subsequently Coomassie stained to determine the location of the protein of interest.

The elution was then placed in a dialysis cassette, which was floated in 1 L of dialysis buffer (50 mM Tris pH 7.4, 150 mM NaCl) at 4°C overnight to dialyse the elution and remove the imidazole. The following day, the elution was added to a Vivaspin protein concentrator spin column (Cytiva) and the protein concentrated via centrifugation at 3500g for one hour at 4°C. The protein was then loaded on a GE Superdex 75 size exclusion column and fractionated according to molecular weight. Fractions were then analysed via SDS-PAGE and Coomassie staining to identify which fractions had a high protein concentration. The protein concentration was estimated using a NanoDrop Spectrophotometer (Thermo Fisher) and the purified protein stored at 4°C for up to 2 weeks. During this study, two proteins were purified and subsequently incubated together for 2 hours at 4°C to allow complex formation.

3.2.2.6 *In vitro* radiolabelled protein translation

^{35}S-Methionine radiolabelled proteins were synthesised using the vector pSP64, into which genes of interest had been cloned, and the TNT® SP6 quick coupled transcription/translation system (Promega) and protocol. Briefly, the T_NT mix was prepared as detailed in **table 3.7** and incubated in the dark at 30°C, for 90 minutes. Subsequently, to remove ribosomes from the TNT mix, the mix was ultracentrifuged for 15 minutes at 55,000g (at 4°C) in a TLA-100 rotor. The supernatant was transferred to a fresh Eppendorf and placed on ice until use in yeast mitochondrial protein import experiments.

Table 3.7: Components of the TNT mix, for a final reaction volume of 50μL.

T_NT Mix Component	**Volume (μL)**
Flexi® Rabbit reticulocyte lysate	25
H_2O	x
T_NT reaction buffer	2
^{35}S Methionine (1000 Ci/mmol, 10mCi/mL)	2
SP6 RNA polymerase (1 U/μL)	1
Amino acid mixture (minus methionine) (1 mM)	1
Ribonuclease inhibitor (40 U/μL)	1
Purified plasmid (1 μg)	x

3.2.2.7 Digital autoradiography and quantification

Radioactive proteins within nitrocellulose membranes were visualised by 48-hour incubation of the membrane with autoradiographic film (Fujifilm). Following incubation, a phosphoimager (Fujifilm FLA-7000) was used to scan the film.

3.2.2.8 Peptide spot array

104 13-amino acid peptides, with a 10 amino acid overlap, were synthesised for the protein sequence of human SFXN3 and covalently bound to a cellulose membrane (JPT). The peptide membrane was prepared according to the JPT protocol and then incubated with ~300 nM purified Tim9/10 complex in protein

incubation buffer (0.1 M KCl, 30 mM Tris pH 8, 5% (w/v) sucrose, 0.5% (v/v) Tween® 20 detergent, 0.5% (w/v) bovine serum albumin (BSA)) overnight at 4°C. The following day, the peptide membrane was washed in 1X TBST (50 mM TRIS, 137 mM NaCl, 2.7 mM KCl, 0.05% (v/v) Tween® 20 detergent, adjusted to pH 8) for 60 seconds, three times.

A blot sandwich was prepared in a semi-dry transfer system (Bio-Rad) as shown in **fig. 3.1**. Six pieces of Whatmann paper (0.34 mm thickness) were soaked in anode buffer 2 (300 mM TRIS, 20% (v/v) methanol) and laid on the anode plate. Six pieces of Whatmann paper soaked in anode buffer 1 (30 mM TRIS and 20% (v/v) methanol) were placed on top of this. A PVDF membrane was prepared according to the JPT protocol and laid on top, followed by the peptide membrane. Finally, the peptide membrane was overlaid by 6 pieces of Whatmann paper soaked in cathode buffer 1 (25 mM TRIS, 40 mM 6-aminohexanoic acid and 20% (v/v) methanol - adjusted to pH 9.2).

Three transfers (two at 25V for 30 minutes, and one at 25V for 1 hour) were performed using this set up, using fresh PVDF membrane and Whatmann paper for each transfer. Subsequently, proteins on the PVDF membrane were detected via Western blotting as described in section 3.2.2.2.

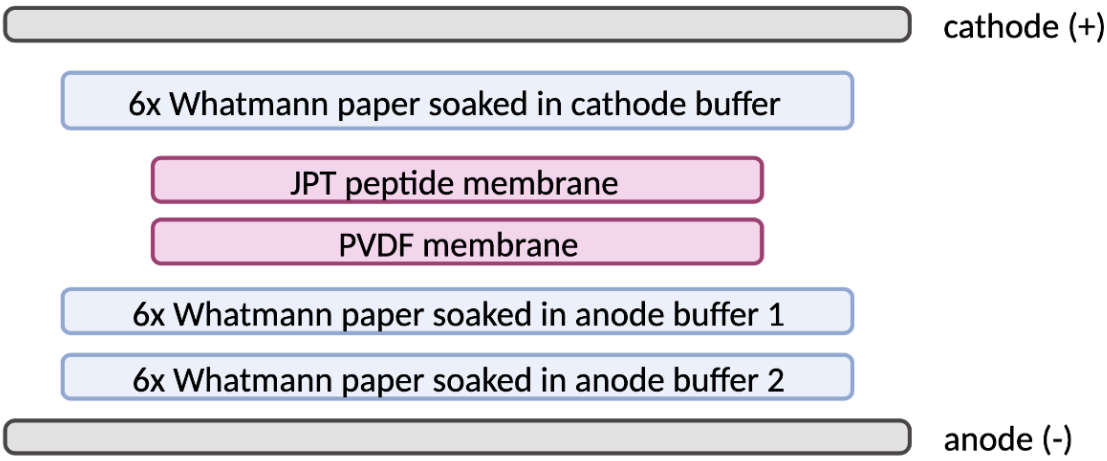

Fig. 3.1: Blotting sandwich for electrotransfer of protein from the peptide membrane to a PVDF membrane.

3.2.3 *In organello* assays

3.2.3.1 Isolation of crude yeast mitochondria

Purification and isolation of mitochondria from yeast was performed as described in the protocol published by Benjamin Glick (Glick, 1991). Yeast cells detailed in section 3.1.6 were grown in YPLac at 30°C overnight, with shaking. The following day, ten litres of fresh YPLac were inoculated with the overnight yeast culture at an OD_{600} of 0.1. The ten-litre culture was then incubated at 30°C, with shaking, for approximately 16 hours. Yeast cells were pelleted via centrifugation at 3000g for 5 minutes, at room temperature, in a JLA8.1000 rotor. Subsequently, the pellets were washed using 300 mL ddH_2O and the solution added to 250 mL buckets. The cells were then pelleted again via centrifugation at 1850g for 5 minutes at 4°C, in a JA-14 rotor. Following centrifugation, the supernatant was removed, and the weight of the cells (pellets) measured.

Cells were resuspended in Tris- 1,4-Dithiothreitol (DTT) buffer (Tris-SO_4 pH 9.4, 10 mM DTT) and incubated at 30°C for 30 minutes with shaking (150 rpm) to weaken the yeast cell wall. Yeast cells were pelleted via centrifugation in the JA-14, at 1850g for 5 minutes at 4°C. The cells were then washed by resuspending in sorbitol buffer (1.2 M sorbitol, 20 mM KP_i pH 7.4) and pelleting as described previously. Pellets were resuspended in sorbitol buffer (5 mL per gram of cells) and zymolyase (3.5 mg per gram of cells) (AmsBio) and the solution incubated at 30°C for 45 minutes, with shaking (120 rpm). This results in the complete degradation of the yeast cell wall and thus the formation of spheroplasts. The spheroplasts were pelleted via centrifugation at 1480g for 5 minutes. To wash the pellets, they were twice resuspended in sorbitol buffer and centrifuged at 1480g for 5 minutes. From this point onwards, the spheroplasts were kept on ice.

Spheroplasts were resuspended in breaking buffer pH 6 (0.6 M sorbitol, 20 mM MES-KOH pH 6) with 2 mM phenylmethylsulfonyl fluoride (PMSF). Subsequently, the solution was transferred to a PTFE Dounce homogenizer, and the cells

broken via 15 passes of a type B pestle. The dounced solution was centrifuged at 1480g for 5 minutes at 4°C to pellet the unbroken cells and collect the broken cells in the supernatant. The pellet was again resuspended in breaking buffer pH 6 and 2 mM PMSF, and douncing repeated as before to break the unbroken cells. The second dounced solution is centrifuged at 1480g as described previously, and the pellet discarded. Supernatants from the first and second round of douncing were combined and the resultant solution of broken cells centrifuged at 12000g for 10 minutes at 4°C to pellet organelles. Subsequently, the pellet was resuspended in breaking buffer pH6 and dounced. The dounced solution was centrifuged at 1480g for 5 minutes at 4°C to pellet any remaining unbroken cells which may be present. The supernatant was carefully removed and centrifuged at 12,000g for 20 minutes to pellet the crude mitochondria. Subsequently, the concentration of the crude mitochondria was determined by measuring OD_{280} of the mitochondria (in breaking buffer pH 6) and using the equation 0.21 OD_{280} = 10 mg/mL mitochondrial protein.

3.2.3.2 Purification of crude mitochondria

To further purify the crude mitochondria prepared as detailed in section 3.2.3.1, nycodenz gradient ultracentrifugation was used. Crude mitochondria were loaded on top of a nycodenz gradient consisting of a 20% (w/v) nycodenz solution (1X breaking buffer pH 6, nycodenz and ddh_2O) overlaid by a 14.5% (w/v) nycodenz solution. The solution was centrifuged at 283,800g for one hour at 4°C in a SW-40Ti rotor (Beckman Coulter). Subsequently, a 19-gauge needle was used to extract the purified mitochondria, which appeared as a brown band between 18% and 14.5% within the gradient. The pure mitochondria were washed by suspending in breaking buffer pH 7.4 (0.6 M sorbitol, 20 mM HEPES-KOH pH 7.4) and centrifuging at 12,500g for 10 minutes at 4°C. The concentration of pure mitochondria was determined by measuring OD_{280} and using the conversion factor 0.12 OD_{280} = 10 mg/mL mitochondrial protein. Subsequently, 10 mg/mL BSA was added to 20 mg/mL aliquots of pure mitochondria (in breaking buffer pH 7.4) and aliquots flash frozen in liquid nitrogen for storage at -80°C.

3.2.3.3 Yeast mitochondrial protein import

Pure mitochondria (~20 mg/mL) were pelleted via centrifugation at 14000 rpm for 5 minutes, at 4°C. Pellets were resuspended in breaking buffer pH 7.4 (0.6 M sorbitol, 20 mM HEPES-KOH pH 7.4). Subsequently, the concentration of mitochondria was estimated by measuring OD_{280} of mitochondria in 0.6% (w/v) SDS and using the conversion factor 0.12 OD_{280} = 10 mg/mL mitochondrial protein.

Mitochondria were added to the import mixes shown in **table 3.8**. Two import mixes were prepared. Carbonyl cyanide m-chlorophenyl hydrazone (CCCP) was added to import mix 2 to deplete the mitochondrial membrane potential, and NADH was omitted.

Table 3.8: Import mix components, for import reactions in the presence (ΔΨ+) and absence (ΔΨ-) of the inner mitochondrial membrane potential.

Components for Import Mix 1 (ΔΨ+)	Components for Import Mix 2 (ΔΨ-)
Import Buffer (2X)	Import Buffer (2X)
ATP (0.1 M)	ATP (0.1 M)
NADH (0.5 M)	CCCP (2.5 mM)
H_2O	H_2O
Mitochondria (50% w/v)	Mitochondria (50% w/v)

The TNT mix containing the radiolabelled protein of interest (section 3.2.2.6) was then added to the import mix (5 μL TNT mix per 50 μg mitochondria). To import the radiolabelled protein into the mitochondria, the import mix was incubated in a water bath at 30°C for timepoints specified elsewhere. To terminate the import reaction, samples were placed on ice for 5 minutes and then centrifuged at 14000 rpm for 5 minutes at 4°C. Pellets were resuspended in trypsin (0.1 mg/mL in breaking buffer pH 7.4) and incubated on ice for 30 minutes to degrade any unimported material. As a control, pellets were also resuspended in trypsin and 1% (v/v) Triton-X100 (in breaking buffer pH 7.4).

Triton-X will permeabilise all mitochondrial membranes, allowing trypsin to degrade all mitochondrial proteins. Following trypsin (+/- Triton-X) incubation, the samples were centrifuged at 14000 rpm for 5 minutes (at 4°C). Pellets were resuspended in soybean trypsin inhibitor (1 mg/mL) and incubated on ice for 10 minutes, terminating trypsin activity. Mitochondria were then pelleted by centrifugation at 14000 rpm for 5 minutes, and pellets resuspended in 10 μL 2X Laemmli buffer. Samples were boiled at 95°C for 5 minutes and then loaded into the wells of a tris-tricine SDS-PAGE gel as described in section 3.2.2.1. Following SDS-PAGE, radiolabelled proteins were transferred to a nitrocellulose membrane as in section 3.2.2.2 and visualised as per section 3.2.2.7.

3.2.4 *In vivo* assays

3.2.4.1 Yeast spot tests

Yeast colonies were grown overnight in YPD liquid media at 30°C (with shaking). Subsequently, the optical density at 600 nm (OD_{600}) of each yeast culture was measured. Yeast cells were then diluted in sterile ddH_2O to achieve an OD_{600} of 0.1. Ten-fold serial dilutions of the 0.1 OD yeast were performed (from 0.1 to $1x10^{-5}$). 5 μL of each serial dilution was spotted onto YPD, YPLac, or YPGal plates and cells were grown for 48 hours at 30°C or 37°C. Plates were visualised using the Bio-Rad ChemiDoc Imager.

3.2.4.2 Stressor sensitivity assays

YPLac was prepared and autoclaved at 121°C for 15 minutes. One of the following stressors were then added to the molten agar: DTT, hydrogen peroxide (H_2O_2), 1,10-Phenanthroline or egtazic acid (EGTA). Yeast spot tests were then performed, as in section 3.2.4.1, with serially diluted yeast being spotted onto the stressor plates.

3.2.4.3 shRNA transient transfection

Hek293 cells were seeded into a 6-well plate at a seeding density of $0.3x10^6$ cells and grown overnight at 37°C in DMEM (Gibco). The following day, the media was replaced with 1 mL fresh DMEM. 1 μg of purified plasmid DNA was diluted in Opti-MEM™ reduced serum medium (Gibco) in an Eppendorf. Subsequently, FuGENE® HD transfection reagent (Promega) was added to the Eppendorf, at a 3:1 FuGENE® HD transfection reagent:DNA ratio. The mixture was then incubated at room temperature for 30 minutes. Following the incubation, 500 μL FuGENE® HD transfection reagent/plasmid DNA mixture was added to the fresh media in each well of the 6-well plate. Cells were incubated at 37°C for 48 hours.

2 days post-transfection, the media was aspirated from the Hek293 cells and replaced with DMEM supplemented with 1 μg/mL puromycin (selective media). Cells were maintained in selective media for approximately 2 weeks, with the media being replaced every 2-3 days to remove any dead cells. Cell viability was examined regularly using the Countess® II Automated Cell Counter. After 2 weeks, 'islands' of alive Hek293 cells were visualised under the microscope. At this point, to check if the shRNA transfection was successful, the cells were transferred to a T75 flask and grown to ~70% confluency. Subsequently, cells were lysed for Western blotting as described in section 3.2.2.2. Due to issues with the cell lysis, the transfection could not be repeated, and a monoclonal population could not be generated.

3.2.4.4 Lysate preparation

Proteins were extracted from Hek293 cells through cell lysis. Hek293 cells were grown to ~70-80% confluency in a 6-well plate. The old media was removed, and cells carefully washed two times using ice-cold phosphate-buffered saline (PBS) (Gibco). 100 μL ice-cold lysis buffer was then added to each well of the 6-well plate. Three lysis buffers were used throughout this report. Foremost, cells were lysed using a Triton-X100 lysis buffer (1% (v/v) TritonX-100, 150 mM NaCl, 20 mM TRIS (pH 7.4), 1 mM EDTA, 1 cOmplete™ mini protease inhibitor cocktail tablet (Roche)). Subsequently, with the aim of more efficiently extracting membrane proteins, RIPA buffer (Sigma) and 2% (w/v) dodecyl beta-D-maltoside (DDM) (in

PBS) were used for cell lysis. Following addition of the lysis buffer, the cells were harvested from each well using a cell scraper and added to an Eppendorf. The Eppendorf was then placed on an orbital shaker at 4°C for 15 minutes (for DDM lysis) or 1 hour (for RIPA and TritonX lysis) to further promote cell lysis. Subsequently, tubes were centrifuged at 10,000g for 10 minutes at 4°C to pellet cell debris and non lysed cells, thus clarifying the lysate. Protein concentration of lysates was estimated using a NanoDrop Spectrophotometer (Thermo Fisher) where DDM or TritonX had been used for cell lysis. To measure protein concentration of lysates where RIPA lysis buffer had been used, a Bradford Assay was performed by adding Coomassie G-250 (Bio Rad) to lysates and measuring OD_{595} of the samples. Equal amounts of protein were then added to 2X Laemmlli sample buffer and loaded into the wells of a Tris-tricine gel for protein separation (as per section 3.2.2.1). Following this, Western blotting was performed as previously described to assess levels of specific proteins.

3.2.5 *In silico* analysis

All protein sequences used throughout the '*in silico* analysis' section were obtained from UniProt and downloaded in FASTA format.

3.2.5.1 Sequence alignment

Multiple sequence alignments (MSA) were performed using EMBL-EBI MSA programme Clustal Omega. Pairwise sequence alignments were performed using bioinformatics tool nucleotide BLAST or EMBL-EBI tool EMBOSS Needle.

3.2.5.2 Transmembrane topology prediction software

To predict transmembrane topology, protein sequences were input into the following online tools: HMMTOP 2.0 (Tusnády and Simon, 2001), TOPCONS (Tsirigos et al., 2015), MEMSAT-SVM (Nugent and Jones, 2009) and PHOBIUS (Käll, Krogh and Sonnhammer, 2004).

3.2.5.3 MTS prediction software

For MTS prediction, protein sequences were entered into MTS prediction software packages TargetP 2.0 (Armenteros et al., 2019) and MitoFates (Fukasawa et al., 2015).

3.2.5.4 Three-dimensional (3D) structure visualisation

3D structure predictions were downloaded in PDB format from the AI database AlphaFold (Jumper et al., 2021; Varadi et al., 2021). For visualisation and analysis of protein structures, PDB files were input into UCSF ChimeraX (Petterson et al., 2021). For superimposition of structures in ChimeraX, the MatchMaker command was used.

3.2.5.5 Illustration

Illustrations in this report were created using web-based tool BioRender or Adobe illustrator (version 16.0) and Adobe photoshop (version 13.0).

3.2.5.6 Graphs

Graphs in this report were produced in Microsoft Excel.

Chapter 4: *In silico* analysis of the structure and sequence of human SFXN3

4.1 Introduction

As discussed in the introduction (section 1.5.1), SFXNs localise to a mitochondrial membrane and are predicted to possess multiple TMs (Fleming et al., 2001; Mon et al., 2019; Acoba et al., 2021; Jackson et al., 2022). Thus, SFXNs have been proposed as a non-canonical MC family. Despite the recent increase in research focusing on this family, their experimental structure has not been solved. Consequently, information regarding structure and topology of SFXNs is sparse.

Early study by Fleming and colleagues (2001) stated that sideroflexin-1 (SFXN1) harboured five putative TMs. Due to their high sequence similarity, SFXN3 has been presumed to also possess five TMs (Chen et al., 2022). A few papers have analysed the SFXN3 sequence for TMs via topology prediction tools, hydropathy analysis and the Kyte-Doolittle scale. However, TM predictions for SFXN3 are inconsistent across platforms (Miyake et al., 2002; Yoshikumi et al., 2005; Miotto et al., 2007; Li et al., 2010; Mon et al., 2019; Acoba et al., 2021). Additionally, Ledahawsky and colleagues (2022) confirmed that SFXN3 followed the carrier pathway for import into the IMM. However, the orientation of the N- and C-terminus of SFXN3 at the IMM has not been explored by prediction or experimental means. Therefore, this chapter aimed to use topology and 3D structure prediction tools to provide a more detailed analysis of the sequence and structure of human SFXN3.

4.2 Results

4.2.1 TM structure of SFXN3

Foremost, study focussed on the TM structure of SFXN3. As an experimental structure of SFXN3 was not available, topology prediction programs were used to predict number and location of TMs within the sequence of SFXN3 (**fig. 4.1**). Raw data generated by each prediction program can be found in **appendix fig. 1** and is summarised in **appendix table 2**.

As shown in **fig. 4.1,** SFXN3 was consistently predicted to have four TMs and a short (~33 amino acid) C-terminal extension. Three of the four programs (HMMTOP 2.0, MEMSAT-SVM and PHOBIUS) identified TMs at similar segments of the SFXN3 sequence, increasing confidence that a TM does lie at such positions. These programs did not identify any TM within the first 144 residues of SFXN3, giving the protein a large N-terminal domain which is not membrane-embedded. In contrast, TOPCONS identified a TM within the N-terminal domain. As this TOPCONS prediction was not supported by any other prediction tool, the study progressed by compiling the sequence regions underlined in **fig 4.1** (as shown in **appendix table 3)** to identify four transmembrane regions (TR) of SFXN3 which will be referred to as TR1-4. TR is used when referring to the collective results of the four prediction tools. TM is used in every other instance.

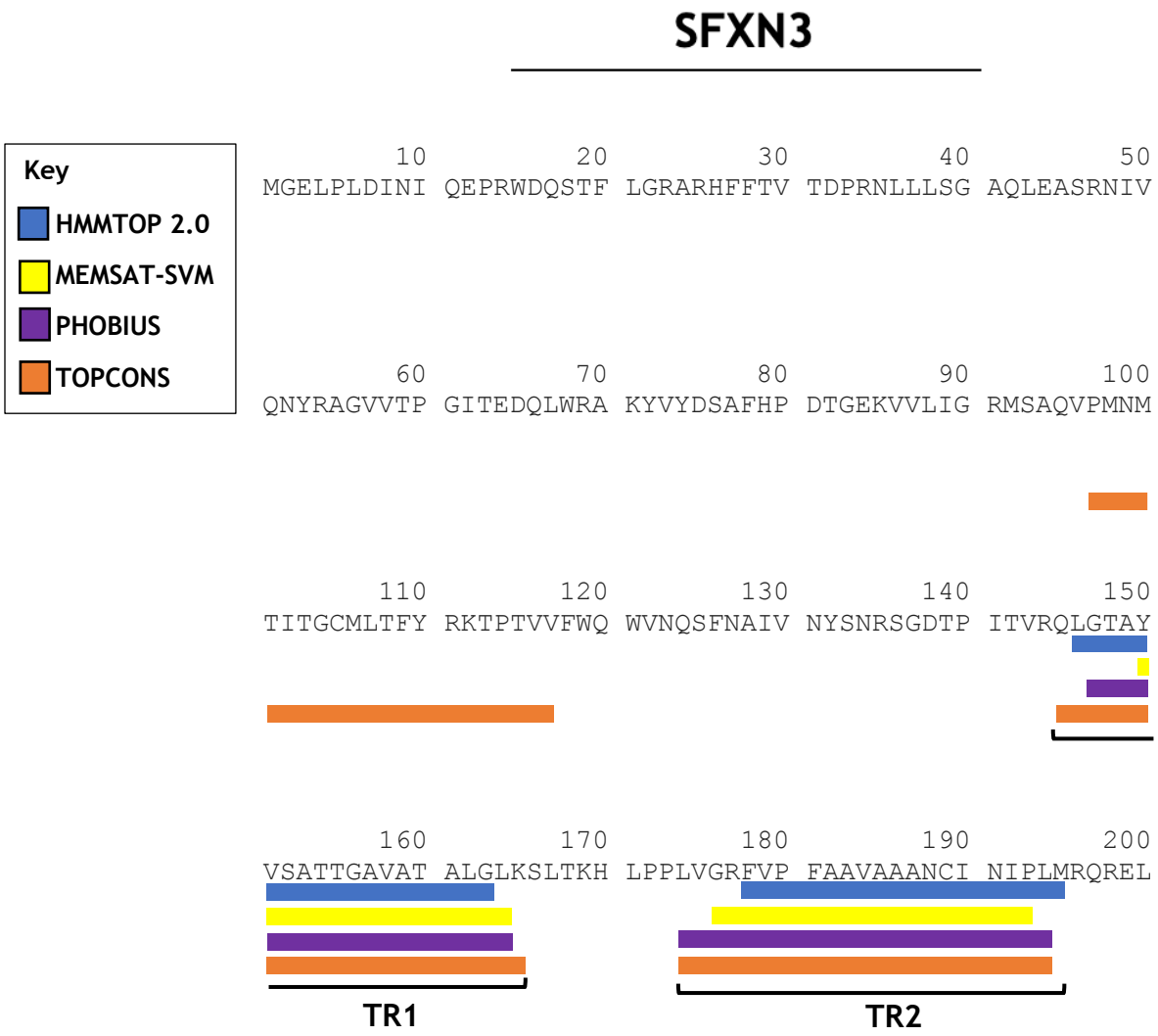

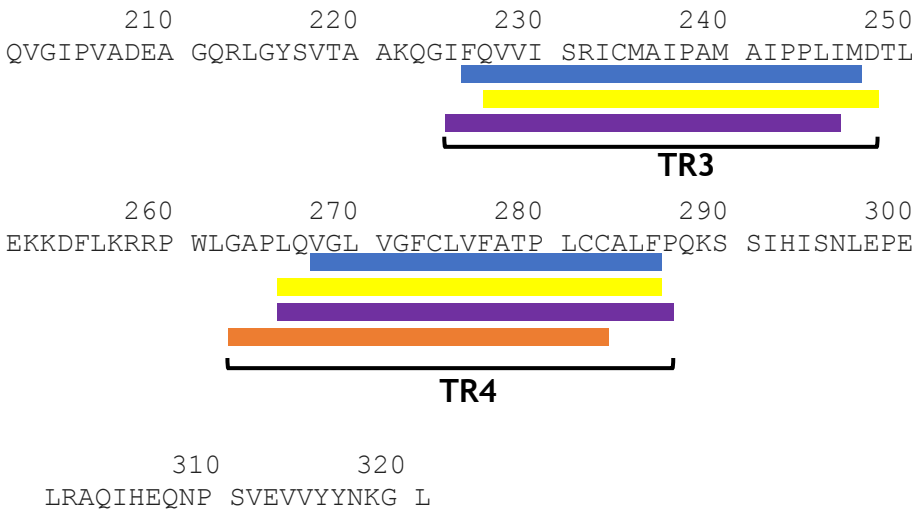

Fig. 4.1: Location of predicted TMs within the protein sequence of human SFXN3. *The protein sequence of human SFXN3 (UniProt ID: Q9BWM7) was input into four online TM prediction tools (HMMTOP 2.0, MEMSAT-SVM, PHOBIUS, TOPCONS). According to the key shown, HMMTOP 2.0 TM predictions are marked by a blue line, MEMSAT-SVM by a yellow line, PHOBIUS by a purple line and TOPCONS by an orange line. TRs are underlined with a solid black line and labelled TR1-4.*

To examine sequence conservation of TRs, protein sequences of each human SFXN family member were aligned using MSA tool Clustal Omega. Positions of SFXN3 TRs were then mapped to the alignment, as shown in **fig. 4.2**. SFXN3 predicted TRs were not particularly well-conserved, with the exception of TR2 which contained several conserved residues and TR4 which contained a well-conserved sequence region towards the C-terminal end (**fig. 4.2**). Both TR2 and TR4 included a conserved proline residue (P180 and P280 respectively), which may indicate the location of a kink of structural importance. The lack of conservation of TR1 and 3 may be explained by the fact that certain SFXN family members show low sequence identity with SFXN3 – for instance, SFXN4 showed only 20.90% identity with SFXN3 (**table 4.1**). Nonetheless, two highly conserved sequence motifs were observed, found in the large N-terminal domain (HPDT/S) and short C-terminal extension ((F/Y)NKGL) of SFXN3. High conservation of these motifs may suggest importance for function.

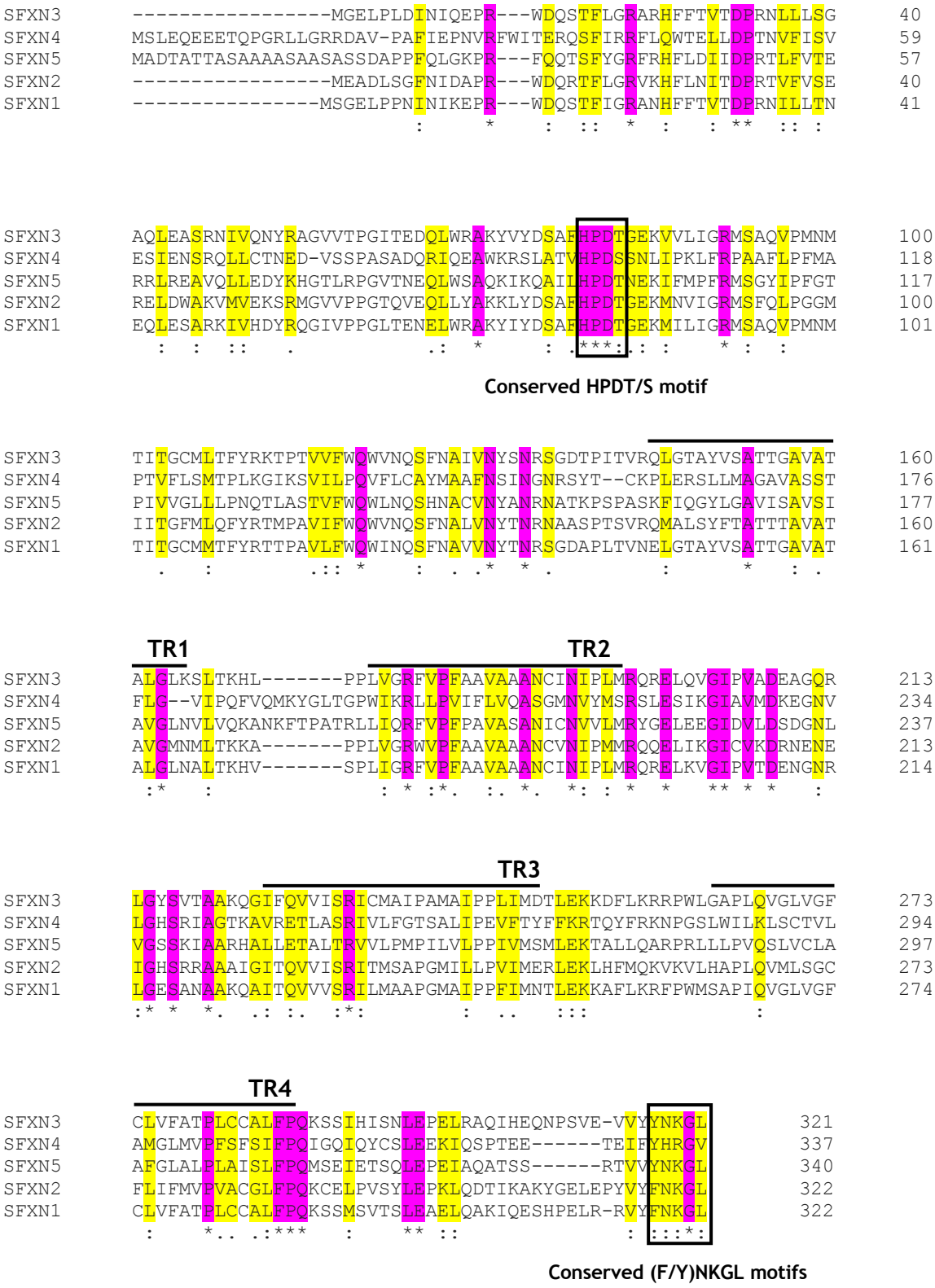

Fig. 4.2: Multiple sequence alignment of human SFXN1-5, showing location of SFXN3 predicted TRs. *Protein sequences of SFXN1 (UniProt ID: Q9H9B4), SFXN2 (UniProt ID: Q96NB2), SFXN3 (UniProt ID: Q9BWM7), SFXN4 (UniProt ID: Q6P4A7) and SFXN5 (UniProt ID: Q8TD22) were aligned using MSA tool Clustal Omega.*

Fully conserved residues are indicated by an asterisk (*) and are shaded in pink. Conserved residue properties are shaded in yellow and indicated by a colon (:), where residue properties are highly similar, or a period (.), where residue properties are weakly similar. Conserved motifs are labelled. Location of predicted TRs are shown by a solid black line above the sequence of SFXN3 and are labelled as TR1-4.

Table 4.1: Percentage identity between pairs of human SFXN family members. *Protein sequences of SFXN1 (UniProt ID: Q9H9B4), SFXN2 (UniProt ID: Q96NB2), SFXN3 (UniProt ID: Q9BWM7), SFXN4 (UniProt ID: Q6P4A7) and SFXN5 (UniProt ID: Q8TD22) were obtained from UniProt. Pairwise alignments were performed using BLASTp to determine percentage identity. Identity refers to the percentage of identical matches of residues across two sequences. Output is shown as percentages (%).*

Proteins		**Identity (%)**
SFXN1	SFXN2	56.05
SFXN1	SFXN3	76.56
SFXN1	SFXN4	22.04
SFXN1	SFXN5	38.77
SFXN2	SFXN3	55.87
SFXN2	SFXN4	22.15
SFXN2	SFXN5	38.51
SFXN3	SFXN4	20.90
SFXN3	SFXN5	39.81
SFXN4	SFXN5	27.39

To visualise the secondary structure of TRs, TR1-4 were mapped to the AlphaFold predicted 3D structure of SFXN3 **(fig. 4.3).** TOPCONS predicted TM1 was considered separately. **Fig. 4.3** demonstrates that each TR largely mapped to a single helix. To strengthen this result, AlphaFold generates a per-residue confidence score (pLDDT) whereby a score of 0 represents low confidence and a score of 100 represents high confidence that the structure predicted accurately represents the 3D structure of the protein (Jumper et al., 2021). pLDDT of

AlphaFold predicted structures corresponds to the structures local Distance Difference Test (lDDT) score, which is a measure of backbone accuracy computed by calculating the distance between carbon α (Cα) atoms within the structure (Mariani et al., 2013). AlphaFold computed a high confidence score between 70 and 100 for all helical regions of SFXN3.

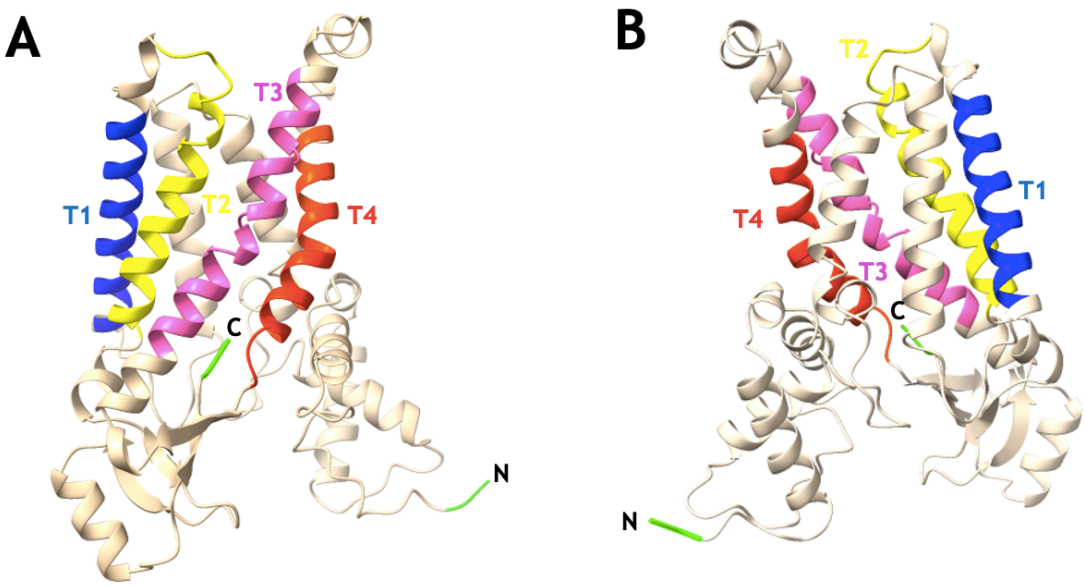

Fig. 4.3: AlphaFold-predicted structure of human SFXN3, showing location of predicted TRs *(A) Structure prediction of human SFXN3 was obtained from AlphaFold and downloaded as a PDB file. The structure was edited in ChimeraX to add the location of predicted TRs. TR1 (T1) is coloured blue, TR2 (T2) coloured yellow, TR3 (T3) coloured pink and TR (T4) coloured red. N- and C-termini are labelled and shown in green. (B) 180° rotation of (A).*

To visualise the structure of the 144aa N-terminal domain of SFXN3, its sequence was mapped to the SFXN3 AlphaFold structure (**fig. 4.4**). As shown in **fig. 4.4A**, the N-terminal domain spanned three smaller (α1, α2, α3) and two larger alpha helices (α4, α5). Based on the overall structure, α4, α5 appear to form a bundle-like structure with the four predicted TRs of SFXN3 **(fig. 4.4B).** In addition, TOPCONS-predicted TM1 mapped to α4 and α5 and the loop connecting these helices (**fig. 4.4C**). Therefore, it is tempting to speculate that α4 and α5 represent two additional TMs of SFXN3, bringing the total to six.

Overall, TR and AlphaFold predictions suggest that SFXN3 traverses the IMM via four alpha-helical TMs and that the protein possesses a large N-terminal which may (1) protrude into the IMS, (2) protrude into the mitochondrial matrix or (3) harbour additional transmembrane helices. The highly conserved HPDT/S and (F/Y)NKGL motifs map to the N- and C-termini domains respectively and may be important for function or targeting.

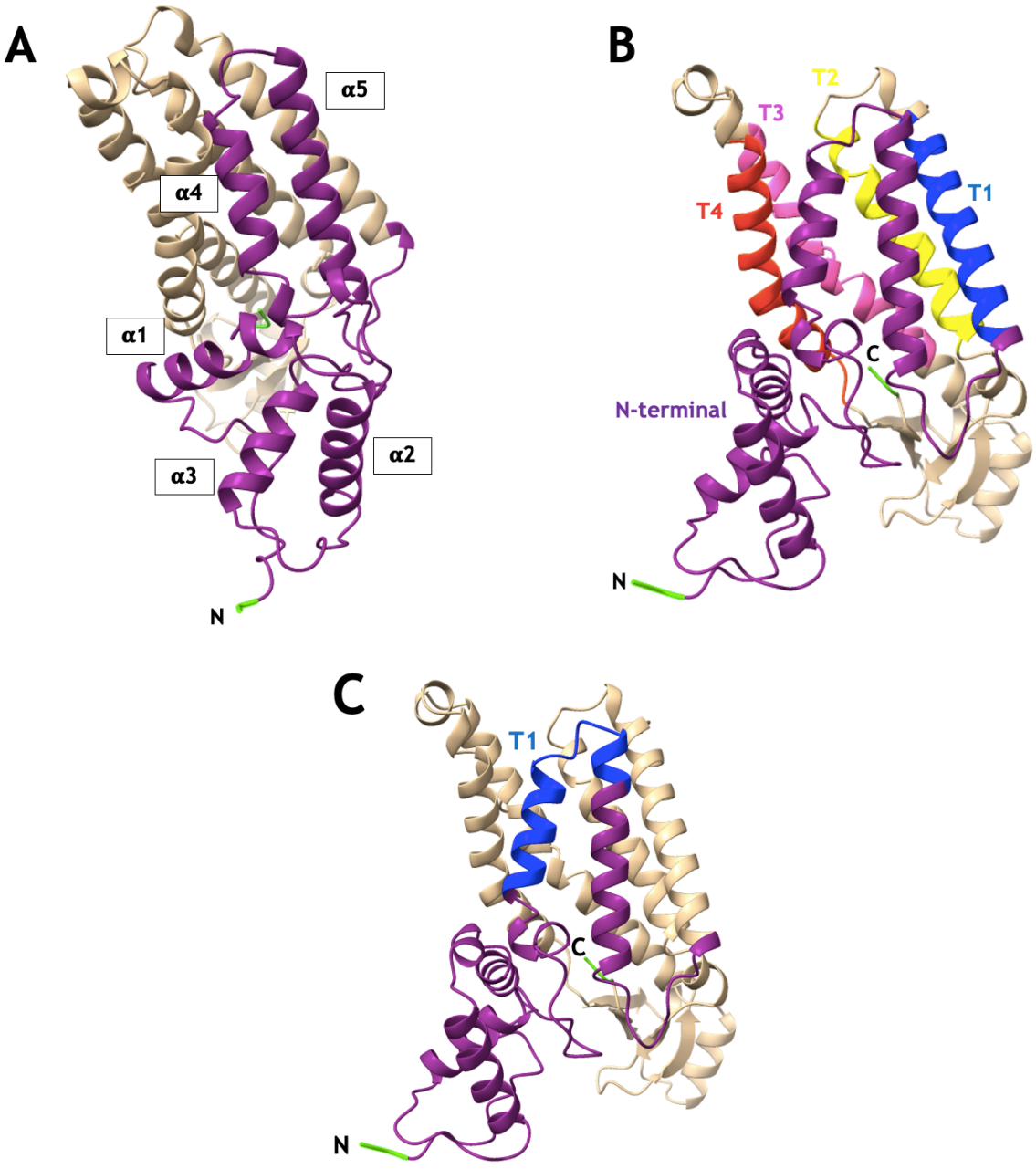

Fig. 4.4: AlphaFold-predicted structure of human SFXN3, showing (A) Large N-terminal domain, (B) N-terminal domain and predicted TRs 1-4 and (C) TOPCONS predicted TM1 within the N-terminal region. *The predicted structure of human SFXN3 was downloaded from AlphaFold as a PDB file. The structure was edited in UCSF ChimeraX to add the location of the large N-*

terminal and predicted TRs. N-terminal domain (residues 1-145) is coloured purple. TR1 (T1) is coloured blue, TR2 (T2) is coloured yellow, TR3 (T3) coloured pink and TR4 (T4) coloured red. N- and C-termini are coloured green and labelled.

4.2.2 AlphaFold-predicted secondary structure of SFXN3

Similar to defined carriers of the SLC25 family, SFXN3 was found to be largely helical (**fig. 4.5**). However, when analysing the predicted structure of SFXN3, it became apparent that SFXN3 possessed four beta-strands (**fig. 4.5**) – a structural element which AlphaFold gave a high confidence score. Two beta-strands were observed in the loop between predicted TR2 and TR3 and the additional two in the C-terminal extension. This feature was found structurally conserved across the SFXN family yet is not typically seen of MCs (**appendix fig. 2**). Overall, results demonstrate that SFXN carriers may bear likeness to classical MCs due to their predicted helical structure. SFXN structural uniqueness appears to lie in a beta-strand region of potential assembly or functional importance.

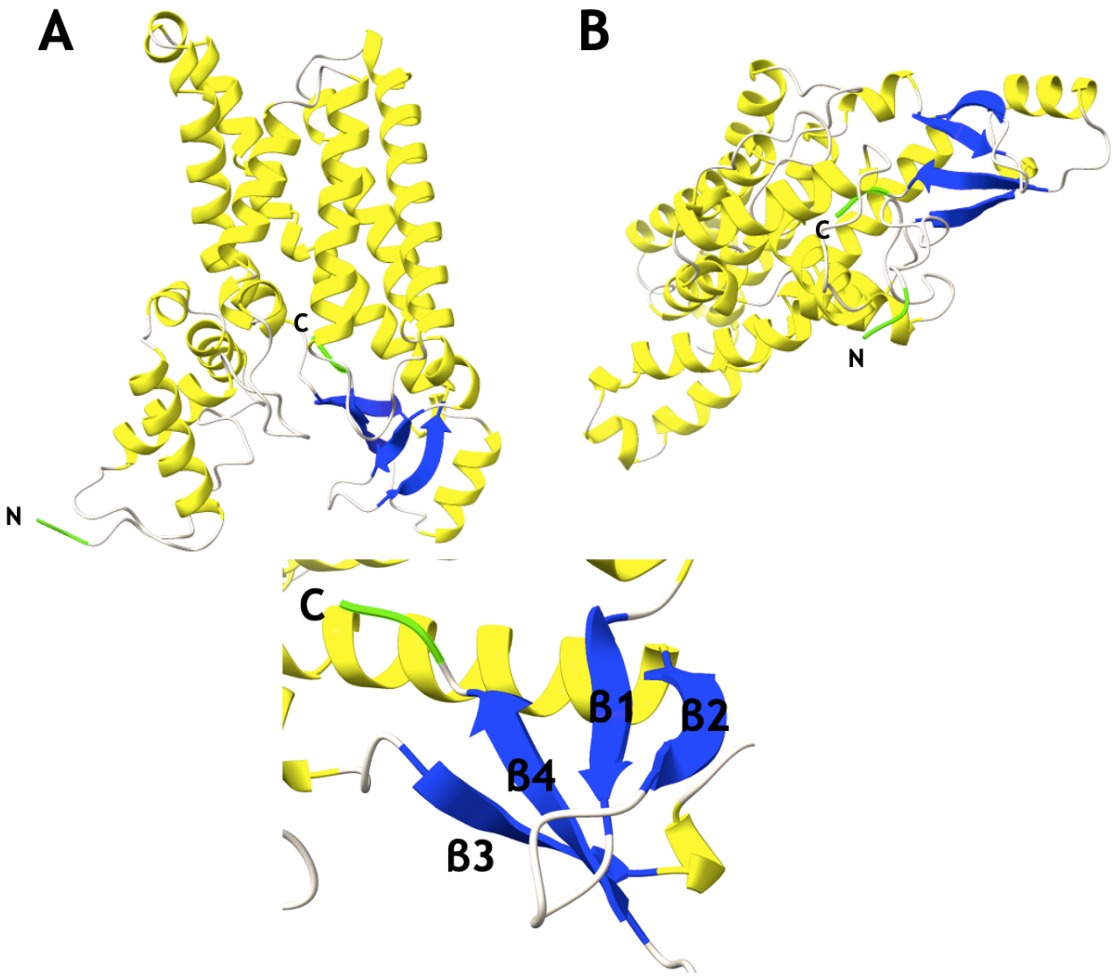

Fig. 4.5: Alpha helices and beta-sheets of human SFXN3 *(A) The location of alpha helices (yellow ribbons) and beta strands (blue arrows) was highlighted on the AlphaFold human SFXN3 structure using ChimeraX. (B) 180° rotation of (A). (C) Beta-strands of SFXN3, labelled β1, β2, β3 and β4 from N- to C-terminal.*

4.2.3 Orientation of SFXN3 at the IMM

To investigate orientation of the N- and C-termini of SFXN3 at the IMM, topology prediction programs were again utilised. Results are shown schematically in **fig. 4.6** and raw data presented in **appendix fig. 1**. As is evident in **fig. 4.6**, there were conflicting results across topology prediction programs. MEMSAT-SVM and TOPCONS predicted that the N- and C-termini of SFXN3 reside in the matrix (**fig. 4.6A**). In contrast, PHOBIUS and HMMTOP 2.0 predicted IMS-localisation of the N- and C-termini (**fig. 4.6B**). It should be noted that these predictions are reliant on the 4-TM structure of SFXN3 being correct.

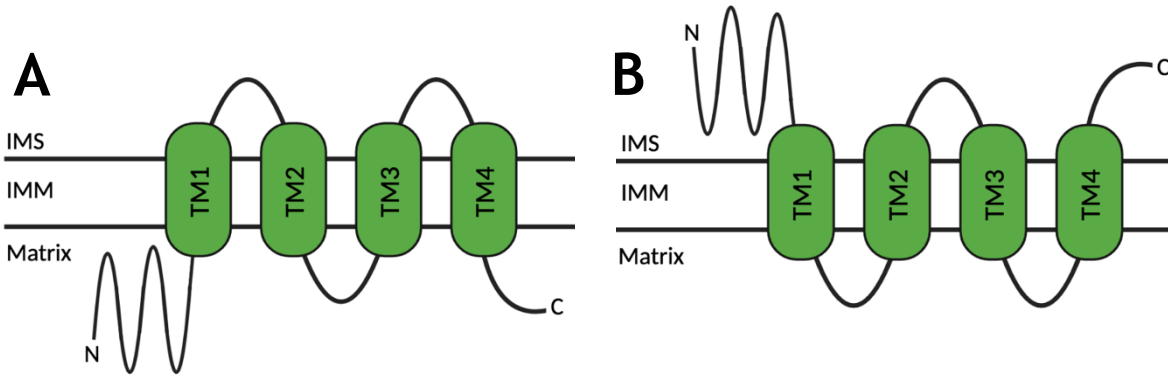

Fig. 4.6: Predicted orientation of SFXN3 N- and C-termini at the IMM *(A) Orientation of SFXN3, predicted by MEMSAT-SVM and TOPCONS. (B) Orientation of SFXN3, predicted by PHOBIUS and HMMTOP 2.0. TMs 1-4 are labelled and coloured green. IMS = intermembrane space.*

As topology predictions were inconclusive, an alternative means of investigating IM orientation was taken. Few IMM proteins harbour an N-terminal pre-sequence which is targeted to the matrix via the stop-transfer pathway (section 1.3.2.2). Therefore, to determine if the N-terminal domain of SFXN3 is matrix-localised, pre-sequence prediction was performed using TargetP 2.0 and MitoFates (**fig. 4.7**). Despite MitoFates' identification of sequence characteristics similar to

typical pre-sequences, such as a possible MPP cleavage site and a Tom20 recognition motif within a predicted amphipathic helix, TargetP and MitoFates did not identify a pre-sequence within the first 144 residues of SFXN3 (**fig. 4.7 A and B**). Additionally, the amphipathic helix identified by MitoFates mapped to a helix on the predicted structure of SFXN3. However, further analysis shown in **fig. 4.8** revealed that this helix was not amphipathic, as there was no separation of hydrophobic and positively charged residues at either side of said helix. Lack of a pre-sequence may suggest that the N-terminus is not matrix-localised and rather resides in the IMS. Nonetheless, this model is speculative and requires support from actual experimental evidence.

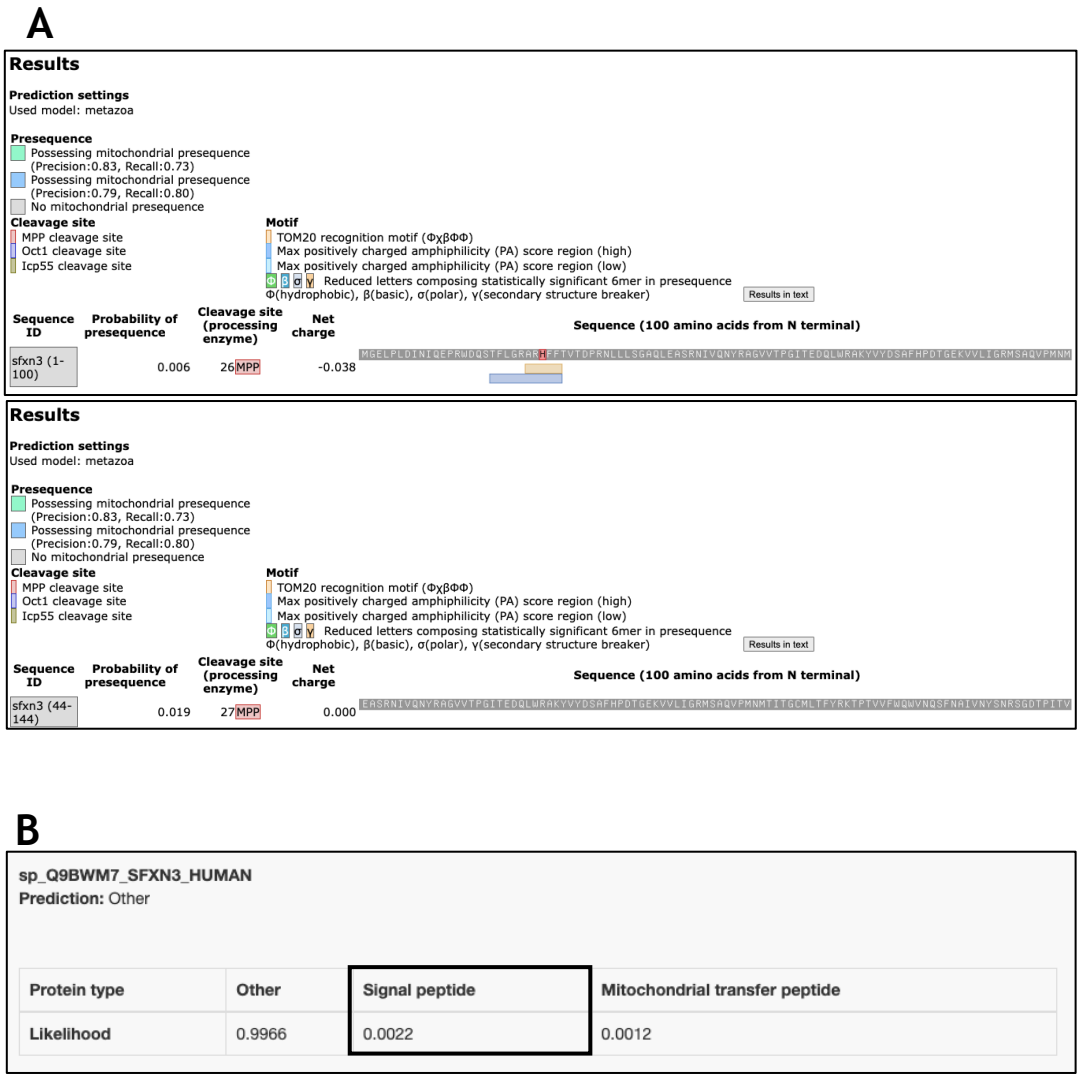

Fig. 4.7: Mitochondrial pre-sequence prediction for human SFXN3 N-terminal domain (residues 1-144). *The presence of a pre-sequence within residues 1-144 of human SFXN3 (UniProt ID: Q9BWM7) was predicted using TargetP 2.0 and MitoFates. (A) MitoFates presents the probability of SFXN3 containing a*

mitochondrial pre-sequence. The yellow underline beneath the SFXN3 sequence represents a potential Tom20 recognition motif. MitoFates analysis was run twice as the software only searches 100 residues in a single run. (B) Target P 2.0 presents the likelihood of the SFXN3 sequence containing a pre-sequence, where 0 is unlikely and 1 is very likely.

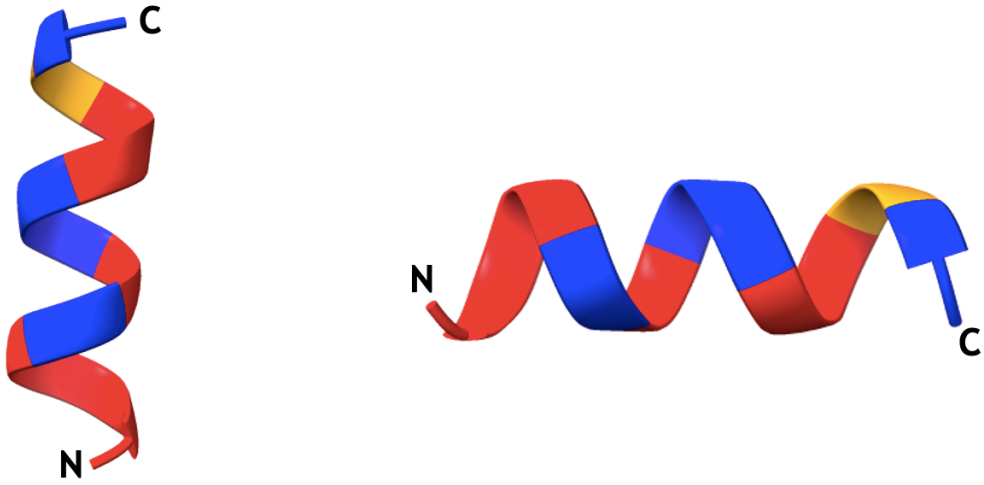

Fig. 4.8: MitoFates predicted amphipathic helix, visualised on human SFXN3 AlphaFold structure. *SFXN3 predicted structure was obtained from AlphaFold. The structure was edited in ChimeraX to highlight only the helix predicted by MitoFates to be amphipathic and harbour the Tom20 recognition motif. Two orientations of the helix are shown. N- and C- termini are labelled. Red indicates position of hydrophobic residues. Blue indicates position of positively charged polar residues. Orange indicates position of uncharged polar residues.*

As a further method of assessing orientation of SFXN3 at the IMM, the study focused on a comparison to SLC25 carriers. Typically, matrix-localised loops of SLC25 MCs are more positively charged than IMS-localised loops. Positively charged loops are drawn into the matrix as this mitochondrial compartment carries a negative charge due to the creation of a membrane potential ($\Delta\Psi$) across the IMM. Therefore, by taking the sequence of predicted TMs from each topology prediction program aforementioned, the sequence and thus charge of loops connecting each TM could be deduced (**appendix table 4 and fig. 4.9**). The N-terminal domain of SFXN3 carried the most positive net charge of all loop regions (**fig. 4.9**). This would suggest that the N-terminus is drawn towards the

negatively charged side of the IMM facing the matrix, supporting a model whereby the N- and C-termini are both matrix-localised. However, as aforementioned, it is possible that further TMs lie in the N-terminal domain. If this were the case, charge of the N-terminal domain would be altered. For interest, charges were considered with the exception of the N-terminus. In this case, matrix loops were more positively charged than those in the IMS in **fig. 4.9A and B** whereas the opposite was true for **fig. 4.9 D**. **Fig. 4.9C** shows little differences in loop charges at either side of the IMM. Thus, if the N-terminus harbours additional TMs, charge predictions may support a model whereby the N- and C-termini of SFXN3 lie in the IMS.

Overall, results of topology analysis were highly contradictory. An overall conclusion regarding the orientation of the N- and C-terminus cannot be reached without (1) knowing the true TM structure of the protein or (2) *in organello* exploration of membrane orientation.

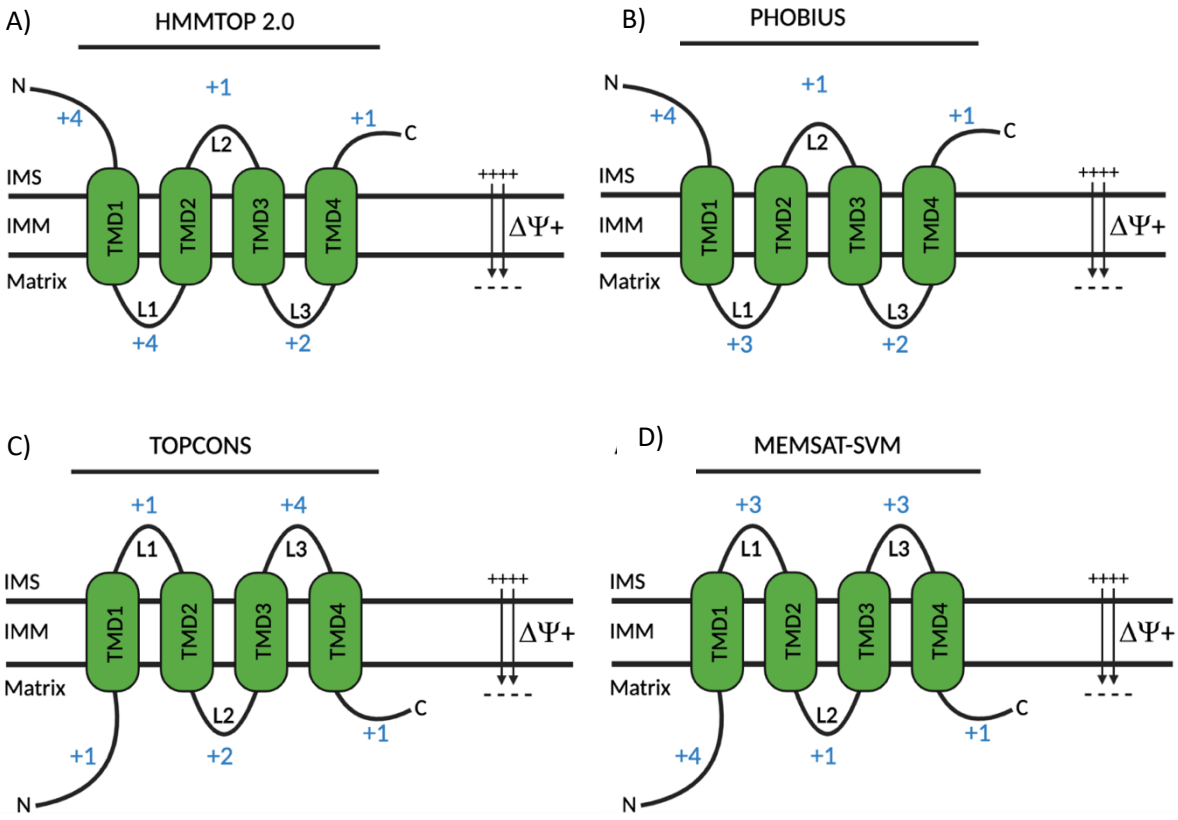

Fig. 4.9: Schematic of SFXN3 showing charges of N- and C-terminal domains and IMS- and matrix-localised loops (labelled L1-3 from N- to C-termini). *Orientation of SFXN3 at the IM was predicted using online tools MEMSAT-SVM,*

TOPCONS, HMMTOP 2.0, PHOBIUS. Using the output of these tools, the protein sequence and thus, overall amino acid charge, of the loop regions and N- and C-termini was determined. Charges are shown in blue based on sequence predictions from (A) MEMSAT-SVM, (B) TOPCONS, (C) HMMTOP 2.0 and (D) PHOBIUS. $\Delta\Psi$+ = IMM potential, showing negatively charged matrix. Loops are labelled from N- to C-termini as loop 1 (L1), loop 2 (L2) and loop 3 (L3).

4.3 Discussion

Prior to this study, information regarding the structure and topology of SFXN3 had been obtained via use of single prediction tools. The present study builds upon this by combining output of sequence conservation analysis, several topology prediction programs and AlphaFold structure predictions to create a more detailed overview of human SFXN3 sequence and structure.

4.3.1 SFXN3 is likely a 4-TM domain protein

HMMTOP 2.0, TOPCONS, MEMSAT-SVM and PHOBIUS are online software tools which predict the orientation of proteins in membranes and the location of TMs (Tusnády and Simon, 2001; Tsirigos et al., 2015; Nugent and Jones, 2009; Käll, Krogh and Sonnhammer, 2004). All tools assess differences in amino acid composition across segments of a protein sequence, search for hydrophobic stretches of ~15-30 residues, and incorporate signal peptide and globular protein predictions to allow these to be distinguished from TMs. Prediction tools diverge in their additional features which are included to improve accuracy, for instance HMMTOP 2.0 incorporates information from experimentally solved structures; TOPCONS combines output from several prediction programs, runs a BLAST search to identify similar sequences with known structures, and uses a prediction tool (ZPRED) to assess distance of each amino acid from the most central point of the membrane; MEMSAT-SVM uses several support vector machines to perform predictions, which evidence suggests can predict TMs with 89% accuracy (Nugent and Jones, 2009); PHOBIUS runs a BLAST search, and uses similar sequences in a MSA before making TM predictions.

TM predictions in **fig. 4.1** identified four TRs which each mapped to a single helix on the SFXN3 Alpha-Fold predicted structure (**fig. 4.3**). These results support TM predictions made by Acoba et al. (2021) and Mon et al. (2019), suggesting that SFXN3 may be a 4-TM protein. In addition, TM predictions support belief that SFXNs are non-canonical MCs as their structure differs from SLC25 carriers (6 TM proteins) and MPCs (2-3 TM proteins) (Cunningham and Rutter, 2020).

Nonetheless, additional findings of the study may point towards SFXN3 harbouring an additional 1-2 TMs. For instance, TM prediction program TOPCONS identified a TM at a sequence region which went undetected by other programs (**fig 4.1**). Perhaps TOPCONS results diverge from that of other prediction tools due to the aforementioned additional ZPRED prediction. By assessing this physical property of membrane proteins, it may provide a more representative prediction of the protein native structure. Additionally, a study comparing TM prediction programs found that TOPCONS had a greater prediction accuracy relative to MEMSAT-SVM and PHOBIUS (Tsirigos et al., 2015). Thus, perhaps TOPCONS predictions are correct and SFXN3 harbours an additional TM – bringing the total to five. Supporting this, hydropathy and Kyte-Doolittle analysis demonstrated that Xenopus and mammalian SFXN1-5 harbour 5 TMs, respectively (Yoshikumi et al., 2005; Li et al., 2010). Adding further support, protease-protection assay demonstrated that closest homolog of SFXN3, SFXN1, has an odd number of TMs, as its N- and C-terminus localised to opposing sides of the IMM (Acoba et al., 2021).

Further to this, it is possible that the TOPCONS-identified TM represents two individual TMs as it maps to two separate helices on the SFXN3 structure shown in **fig 4.4**. If this were true, SFXN3 would take on a 6-TM structure which bears a likeness to the six-helical bundle-like structure of classical SLC25 carriers – such as bovine AAC (**fig. 4.10**). The helical bundle structure of SLC25 carriers creates a central pore which the substrate can enter and ultimately pass through upon conformational change (Pebay-Peyroula et al., 2003). Thus, this helical arrangement may be crucial for facilitating substrate translocation by SFXN3.

In addition, analysis of TR sequence conservation in **fig 4.2** highlighted further resemblance to SLC25 carriers as SFXN3 harboured a conserved proline residue in TR2 and TR4. SLC25 carriers possess a conserved proline in their odd-numbered helices, introducing a sharp kink in the helical structure which permits the tight packing of helices which aids the closing of the carrier to prevent entry to the matrix side (Pebay-Peyroula et al., 2003; Schmidt, Situ and Ulmer, 2016). Therefore, perhaps said proline residues are conserved in SFXN family members as they are vital for the mechanism of substrate translocation.

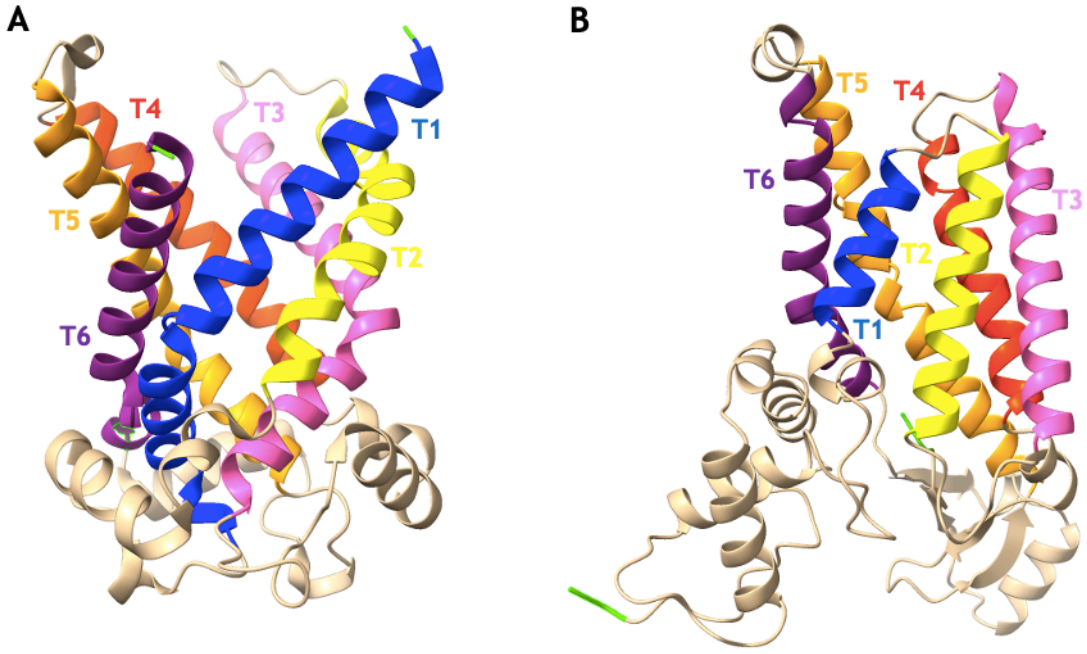

Fig. 4.10: Comparison of the known TM-structure of bovine AAC and the predicted TM-structure of human SFXN3. *(A) Bovine AAC structure. The crystal structure of AAC was obtained from PDB (PDB ID: 1OKC) and edited in UCSF ChimeraX to highlight its six TMs, labelled T1-T6 from the N- to C-terminus. (B) Human SFXN3 structure. The predicted structure of SFXN3 was obtained from AlphaFold and edited in UCSF ChimeraX. T1 and T2 represent the potential transmembrane domains identified by TOPCONS. T3-T6 correspond to TRs 1-4. N- and C-termini are coloured green.*

4.3.2 SFXN3 has a large N-terminal domain and short C-terminal domain which contain highly conserved motifs

Three of the four TM topology prediction programs utilised in chapter 4 show SFXN3 to have a large, ~144 amino acid N-terminal domain (**fig. 4.1 and fig. 4.4**). In contrast, the C-terminus of SFXN3 is relatively short at ~33 amino acids. It is reasonable to suggest that the N-terminal domain of SFXN3 may act to sense levels of its substrate, as has previously been shown for a proline/alanine mitochondrial transporter (Schlisselberg et al., 2015). However, as SFXN1 and SFXN3 show functional redundancy (with respect to serine transport) and SFXN3 is the sole mammalian SFXN predicted to harbour such a long N-terminal domain, it seems unlikely that SFXN3 would possess a substrate-sensing ability which SFXN1 lacks (Kory et al., 2018; Acoba et al., 2021). Perhaps this result points towards SFXN3 having a distinct function relative to the other SFXN carriers, but further investigation is required to clarify. Additionally, plant MCs and MCs which follow the stop-transfer pathway for import often have large N-terminal domains which are cleaved by MPP as the protein is integrated into the IMM (Haferkamp and Schmitz-Esser, 2012; Edwards, Eaglesfield and Tokatlidis, 2021). However, molecular weight of SFXN3 is unchanged upon import into mammalian and yeast mitochondria (Ledahawsky et al., 2022), which suggests that such a cleavage event does not occur, and the N-terminal region is possessed by the mature protein. It may be more likely that the N-terminal domain improves translocation efficiency, as will be discussed in chapter 5 of this study.

The N- and C-termini of SFXN3 harbour HPDT/S and F/YNKGL motifs, respectively (**fig. 4.2**), which are conserved across human SFXN paralogs. However, no functional role has been assigned to said motifs (Tifoun et al., 2021). It could be suggested that the conserved motifs are involved in substrate binding as they both lie at the same end of the predicted helical bundle region of SFXN3 (**fig. 4.11**). ATP/ADP bind AAC at the bottom of the pore created by the helical-bundle structure of the protein (Pebay-Peyroula et al., 2003). The experimental structure of SFXN3 is required to understand if the conserved motifs of SFXN3 mediate similar contacts. With what is currently known regarding SFXNs, perhaps a structural or targeting role of the motifs is more conceivable as all SFXNs possess a similar TM structure and are targeted to the

mitochondria (Mon et al., 2019; Acoba et al., 2021; Jackson et al., 2022; Ledahawsky et al., 2022).

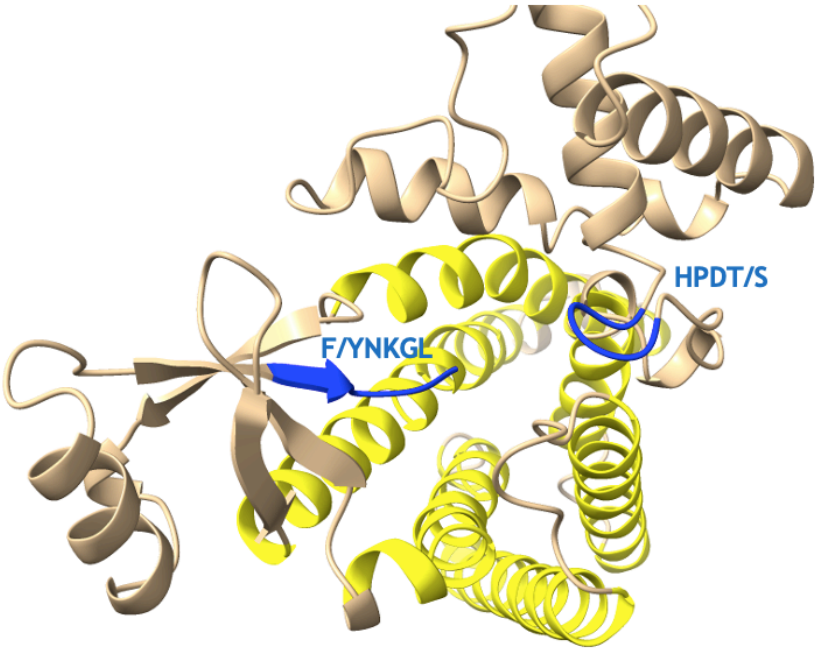

Fig. 4.11: Predicted structure of human SFXN3, showing the location of conserved motifs. *Predicted structure of SFXN3 was obtained from AlphaFold and edited in UCSF ChimeraX. The location of HPDT/S and F/YNKGL motifs is highlighted in blue and labelled. The six helices which form a bundle-like structure are highlighted in yellow.*

4.3.3 SFXN3 structure analysis reveals an unusual beta-strand region

Visualisation of the predicted structure of SFXN3 revealed the protein as largely alpha helical (**fig 4.5**), a feature seen consistently across all identified MC families (Pebay-Peyroula et al., 2001; Miotto et al., 2007; Bender, T., Pena, G. & Martinou, J., 2015). Yet distinct from other MC families, SFXNs possessed four beta-strands (**fig 4.5 and appendix fig. 2**). Similarly, Miotto and colleagues (2007) identified four beta-strands of SFXN5 via hydrophobic cluster analysis, and trRosetta modelling of SFXN1 revealed two beta-strands (Tifoun et al., 2021). This finding raises the question of why have the SFXN family evolved to possess such a secondary structure?

Study by Watkins and Arora (2014) demonstrated that protein-protein interactions at beta-strand motifs contributed to the formation of protein complexes. Generally, MCs tend to function as monomers. However, it is known that the SLC54 family function as heterodimers and aspartate-glutamate carriers function as homodimers (Herzig et al., 2012; Tavoulari et al., 2019). As SFXN1 has been shown to form a ~132 kDa complex at the inner membrane via BN-PAGE, it may be possible that the SFXNs also function as multimers (Jackson et al., 2022). Therefore, perhaps beta-strands are involved in mediating protein-protein interactions of SFXN monomers to permit multimerization. Nonetheless, the most likely explanation for the presence of beta-strands is due to their importance in protein folding and assembly.

4.3.4 SFXN3 N- and C-terminus orientation remains an unknown

As aforementioned, orientation of the N- and C-termini of SFXN3 at the IMM is unknown. Topology prediction did not shed any light on this as programs used produced opposing results (**fig 4.6**). The N-terminus of the protein carries a net positive charge which could be a driving force for matrix localisation (**fig 4.7**). However, without testing if additional TMs reside in the N-terminal domain, we cannot confirm that the charge calculated is accurate. Additionally, pre-sequence analysis shown in **fig 4.7** was inconclusive. Via protease-protection assay, SFXN1 was shown to have a matrix-localised C-terminus and an IMS-localised N-terminus (Acoba et al., 2021). Due to the high sequence similarity of SFXN1 and SFXN3, we could hypothesise that SFXN3 follows the same orientation. However, SFXN topology was recently disputed – with Jackson and colleagues (2021) finding that the C-terminus of SFXN1-3 was exposed to the IMS rather than the matrix. Thus, similar to the present study, experimental evidence is contradictory.

4.3.5 Overall conclusions

Topology predictions presented in this chapter suggest that SFXN3 most likely has four transmembrane regions and a large N-terminal domain, the localisation of which is unknown. The large N-terminal domain may contain an additional 1-2 TM regions, or alternatively may play an isoform (SFXN3)-specific functional role

as other sideroflexins do not harbour this long domain. Sequence analysis demonstrated that SFXN3 harbours conserved proline residues likely of structural importance, potentially playing a role in substrate translocation. The N- and C-terminus harbour conserved HPDT/S and F/YNKGL motifs respectively. Structure predictions led to the discovery of a structurally conserved beta-strand region of the SFXN family. The function of these conserved motifs and secondary structure elements is unknown and warrants further study.

It must be said that all conclusions reached in this chapter are speculative as they are based on prediction programs. Therefore, findings must be accompanied by the further experimental evidence suggested below to provide a more complete overview of SFXN3 structure. Nonetheless, the present chapter compiles data from various different online sources to provide the most detailed *in silico* analysis of SFXN3 to date.

4.3.6 Future study

The most valuable and detailed analysis of SFXN3 structure would come from a Cryo-EM/crystal structure of the protein. This would allow us to (1) confirm presence of beta-strands in SFXN3, (2) confirm presence of a helical bundle, (3) uncover the mechanism of substrate binding, determining if this occurs in close proximity to the conserved motifs and whether conserved prolines play a role. However, as SFXN3 is a small (~35 kDa) membrane protein, obtaining a cryo-EM structure may prove difficult. Several issues could be encountered, including low expression of the protein, and low contrast of images obtained when using detergents for extracting protein from the IMM (Nygaard, Kim and Mancia, 2021). It may be beneficial to determine if SFXN3 forms a complex in the IMM (e.g., via use of BN-PAGE) and focus efforts on determining structure of said complex. If large enough, use of the complex may circumvent size issues for cryo-EM.

Due to the cryo-EM challenges discussed, alternative experimentation could be done to explore SFXN3 topology. Topology could be confirmed by epitope tagging SFXN3 at the N- or C-termini and performing a protease protection assay as described previously (Kory et al., 2018). Additionally, to confirm location of TM

regions, predicted TRs and the N-terminal domain should be imported into isolated mitochondria, mitoplasts created, and sodium carbonate extraction performed to distinguish IM-integrated and soluble proteins. If each predicted TR and the N-terminal domain integrates into the membrane, this can be used as evidence that a TM does in fact lie here. Complex formation of SFXNs could be explored *in vitro* via BN-PAGE or *in vivo* via bioluminescence resonance energy transfer as described previously (Zhang and Fernie, 2020). It would be interesting to mutagenize or remove the predicted beta-strand region and determine if this alters complex formation or mitochondrial import.

Chapter 5: Investigating the mitochondrial targeting of human SFXN3

5.1 Introduction

As aforementioned, SFXN3 is targeted to the IMM via TIM22 and the carrier import pathway (Ledahawsky et al., 2022). SFXNs lack a mitochondrial pre-sequence (Fleming et al., 2001; Mon et al., 2019). Therefore, it is generally assumed that the SFXNs localise to mitochondria via one or more internal targeting signals within TMs. However, no such signals have been characterised for SFXN3. Therefore, this chapter aimed to identify said internal targeting information of SFXN3.

In addition, carrier pathway substrates are bound at exposed hydrophobic TM regions by the Tim9/10 complex in the IMS to protect from aggregation whilst being delivered to TIM22 complex (Curran et al., 2002; Vaseljev et al., 2004; Vergnolle et al., 2005; Weinhäupl et al., 2018). Recently, the NMR structure of Tim9/10 bound to MCs Ggc1/Aac3 revealed that carriers interact with the chaperone complex by sampling several Tim9/10 binding clefts during the course of import (Weinhäupl et al., 2018). In the absence of IMS chaperones, import of MCs becomes impaired (Ryan, Müller and Pfanner, 1999; Weinhäupl et al., 2018). Ledahawsky et al. (2022) established a relationship between SFXN3 and Tim9/10 by demonstrating that Tim9 knockdown impaired levels of SFXN3 import *in organello*. However, the interaction of SFXN3 and Tim9/10 has not yet been characterised. Therefore, this chapter sought to identify SFXN3 sequence regions required for Tim9/10 complex interaction, and thus required for efficient import via the carrier pathway.

5.2 Results: Uncovering mitochondrial targeting information of human SFXN3 via transmembrane domain deletion

5.2.1 Design of SFXN3 truncation proteins

To uncover internal targeting signals of SFXN3, truncations of the full-length protein were designed based on TRs identified in chapter 4 **(fig. 5.1)**. The sequence of SFXN3 was truncated such that each truncation included one less TR

than the previous. For instance, SFXN3-T4 included all 4 predicted TRs, SFXN3-T3 included TR1-3, SFXN3-T2 included TR1-2 and SFXN3-T1 included only TR1. The final truncation encompassed the N-terminal domain of SFXN3, spanning residues 1-144 of the protein (SFXN3-NT). To aid visualisation, the truncations were mapped to a schematic structure of SFXN3 (**fig. 5.2).** Additional TOPCONS-identified TM(s) (**fig. 4.1**) were not included in truncation design as they were not supported by any other platform, and as the SFXN3-NT truncation itself could be used to determine whether this region of SFXN3 is in fact membrane embedded (e.g., via mitoplasting and sodium carbonate extraction).

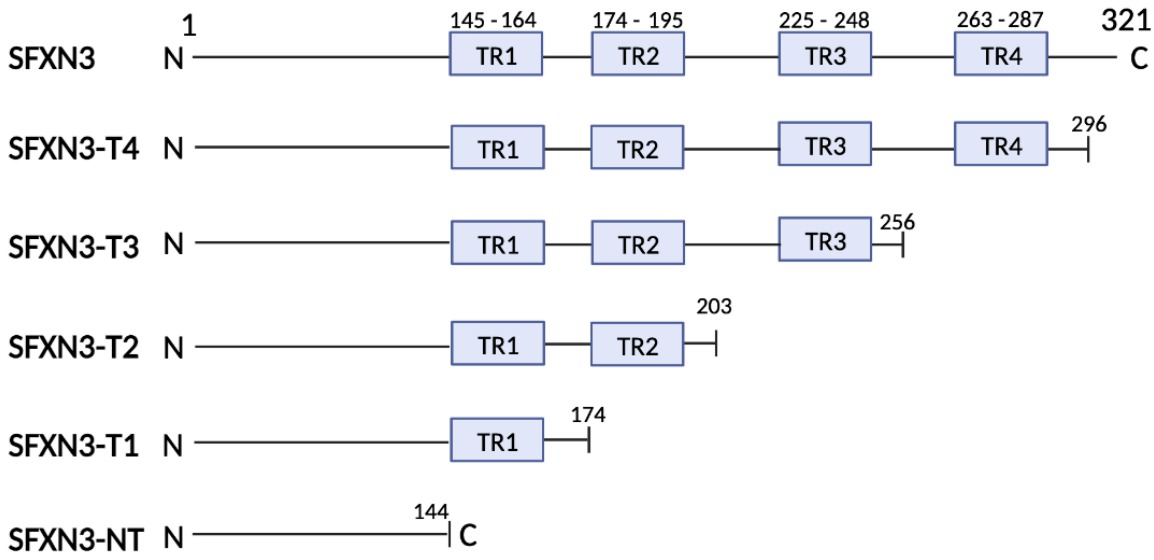

Fig. 5.1: Truncations of the sequence of SFXN3 generated. *(A) Complete sequence of SFXN3 (UniProt ID: Q9BWM7), showing predicted TR1-4 in light blue boxes. The amino acid residues which constitute each TR are shown. (B) The name of each truncation of the SFXN3 sequence generated is shown on the left. SFXN3-NT spans the large N-terminal region of SFXN3 (residue 1-144). SFXN3-T1 consists of residues 1-174 of SFXN3, including TR1. SFXN3-T2 consists of residues 1-203 of SFXN3, including TR1 and 2. SFXN3-T3 consists of residues 1-256 of SFXN3, including TR1, 2 and 3. SFXN3-T4 consists of residues 1-296 of SFXN3, including all TRs but lacking the C-terminal 25aa.*

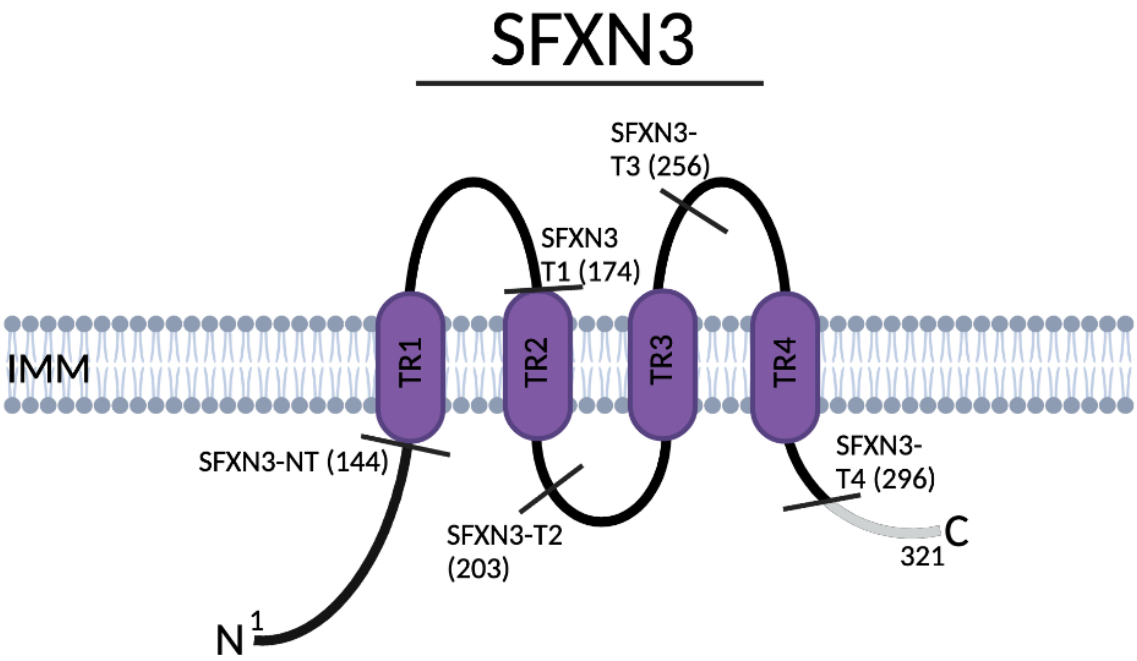

Fig. 5.2: Truncations of SFXN3 mapped to the predicted 4-TR structure. *The C-terminal boundary of each truncation is labelled and depicted by a solid black line. Numbers in brackets correspond to the amino acid residue at which each truncation was made. The orientation of SFXN3 (N- and C-termini) at the membrane is unknown.*

5.2.2 Cloning of SFXN3 truncations into pSP64 vector

To allow truncations to be used in *in vitro* ^{35}S-radiolabelled transcription/translation experiments, they were to be cloned into the pSP64 vector. To initiate the cloning process, SFXN3 truncations were amplified through PCR and subsequently digested using Xba1 and Sal1 restriction enzymes. pSP64 vector was successfully digested using the same restriction enzymes, as verified via gel electrophoresis of the cut and uncut pSP64 vectors. However, subsequent gel purification of the digested plasmid consistently led to complete loss of plasmid DNA. Attempts were made to troubleshoot gel purification by increasing the amount of plasmid DNA digested (to ~2 μg), minimising UV light exposure time and ensuring agarose was completely dissolved via increased incubation time at 50°C. Ultimately, this led to recovery of a low amount of plasmid DNA (~30 ng/μL) and ligation could proceed.

Following ligation of pSP64 to each SFXN3 truncation, the product was transformed into competent *E. coli* cells. Transformed cells showed growth on ampicillin plates, yet the amount of growth was comparable to that on the vector alone (plus ligase) control plate, indicating that there had been self-ligation of the vector. The inability to easily distinguish between single and double-digested pSP64 due to the close proximity of Sal1 and Xba1 restriction sites in pSP64 multiple cloning site (MCS) may have contributed to self-ligation.

5.2.3 Optimising the cloning of SFXN3 truncations

To optimise cloning, EcoR1 and BamH1 were selected as new restriction sites as they do not lie in close proximity within the MCS of pSP64. Additionally, as an alternative to gel purification, the decision was made to PCR amplify pSP64 excluding the region of the MCS between BamH1 and EcoR1 restriction sites. As demonstrated in **fig. 5.3,** pSP64 was successfully amplified using this method.

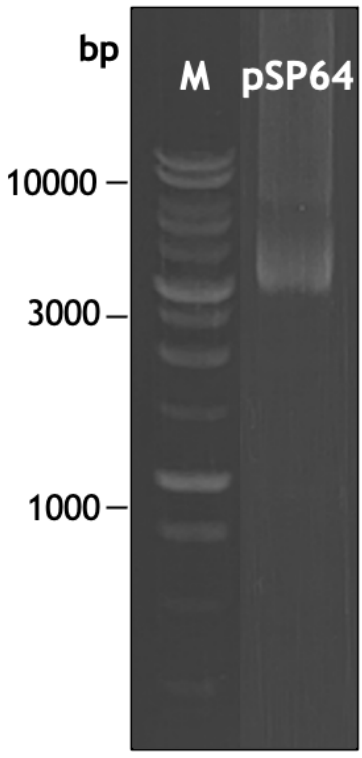

Fig. 5.3: Agarose gel electrophoresis of PCR amplified pSP64 vector. *pSP64 was amplified through PCR using appropriate forward (ID: FRW_PSP64_ECOR1) and reverse primers (ID: REV_PSP64_BAMH1), such that one end of the PCR product was flanked by a BamH1 restriction site and the other by an EcoR1 restriction sites. PCR products were separated via agarose gel electrophoresis.*

1kB DNA ladder (Promega) was run in the lane marked 'M'. Selected bp markers are labelled. Amplified pSP64 was run in the lane marked 'PSP64'. Image was cropped to exclude lanes 2-5 after DNA ladder, with pSP64 being run in lane 6.

pSP64 was then digested and cleaned-up by excluding the initial gel extraction step in the QIAGEN protocol. This provided approximately ~80 ng/μL plasmid DNA, a sufficient amount of DNA to allow ligation to proceed. However, as before, self-ligation was detected. In attempt to troubleshoot this, the ligation reaction was repeated using fresh T4 DNA ligase, a high insert to vector ratio (7:1) and the reaction was incubated under different conditions: 16°C overnight or 4°C for 2 days. Additionally, fresh competent cells were prepared and the viability of these checked using uncut pSP64. In spite of these alterations, a large degree of self-ligation continued to occur.

The decision was made to perform colony PCR to determine if any colonies on the insert (SFXN truncation) + vector transformation plates expressed the insert of interest. Colony PCR was first run using colonies on the SFXN3-T3 truncation + pSP64 transformation plate (**fig. 5.4**). Briefly, as **fig. 5.4** shows, few colonies selected did contain the SFXN3-T3 insert (~780 bp). Therefore, plasmid DNA isolated from said colonies was sent for sequencing. However, sequencing results consistently returned negative – showing only the complete sequence of pSP64 with no insert. It is possible that colony PCR retrieved false positive results as the agar plates on which colonies were selected from were very overcrowded. Perhaps neighbouring colonies contained the insert of interest, and a signal was being detected due to the close proximity of said colonies and high sensitivity of the PCR reaction. In attempt to reduce crowding on plates after transformation, fewer competent cells were transformed, and a lower volume of the transformation spread on agar plates. Nonetheless, colony PCR and subsequent sequencing results showed the same trend as aforementioned. An additional repeat of colony PCR run using SFXN3-T4 is shown in **appendix fig. 3**.

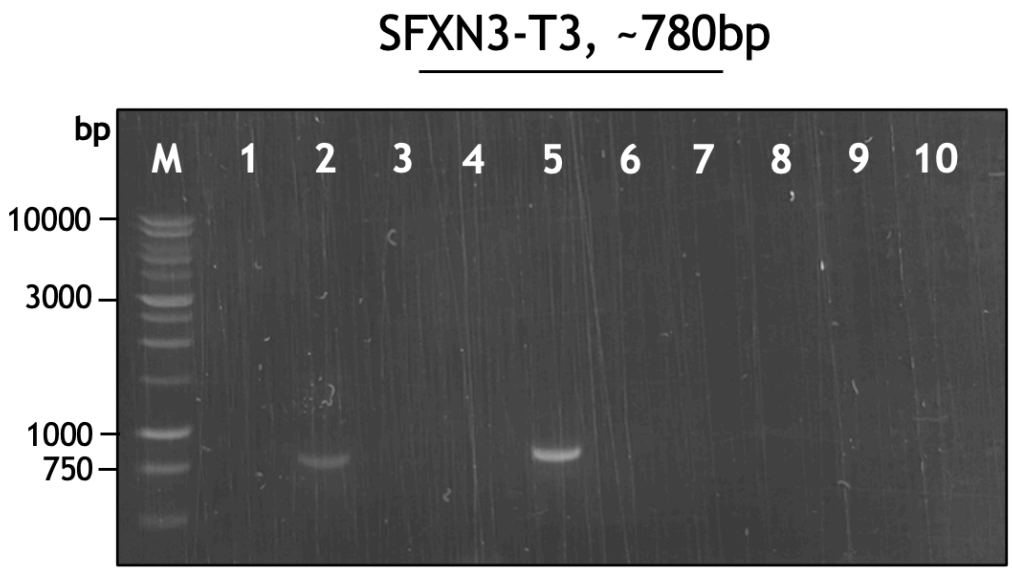

Fig. 5.4: Agarose gel electrophoresis of SFXN3-T3 truncation, amplified through colony PCR. *DNA ligase was used to ligate SFXN3-T3 and pSP64. Ligated product was transformed into competent E. coli cells and grown on LB agar plates overnight at 37℃. To verify that SFXN3-T3-pSP64 was expressed by the bacteria, ten colonies were selected from the plates for use in colony PCR reactions. PCR products were separated via agarose gel electrophoresis. 1kB DNA Ladder (Promega) was run in lane 'M'. Selected bp markers along the ladder are labelled. Lanes 1-10 represent products from 10 individual PCR reactions, one for each colony selected.*

As conventional means of cloning appeared unsuccessful, an alternative approach was taken. A member of the Tokatlidis Lab, Dr. Ruairidh Edwards, had previously cloned the full-length SFXN3 protein into pSP64. Therefore, we decided to create truncations from this vector as shown in **fig. 5.5**. Briefly, primers were designed to amplify the vector such that unwanted regions of SFXN3 were excluded. For instance, SFXN3-NT was to be amplified by excluding the 177 C-terminal residues of SFXN3 to leave only residues 1-144. These primers were also designed such that they would incorporate EcoR1 sites flanking the amplified vector. As demonstrated in **fig. 5.6,** pSP64-SFXN3 truncations were successfully amplified through PCR. Subsequent restriction digest with EcoR1 generated compatible ends which could be re-ligated together. Ultimately, sequencing showed this method of SFXN3 truncation cloning to be successful.

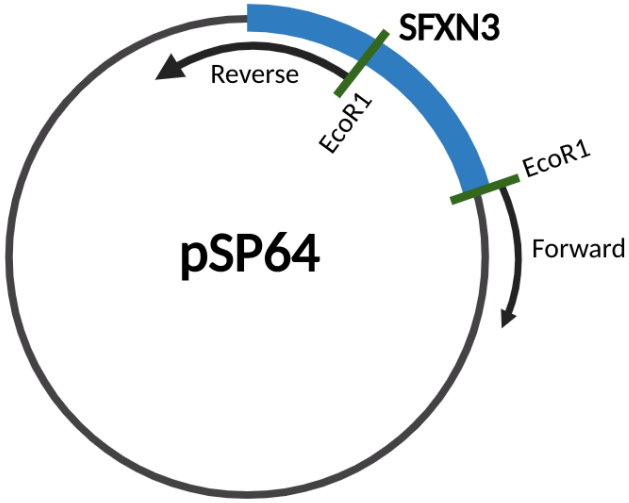

Fig. 5.5: Schematic of pSP64-SFXN3 vector, showing how truncations of the SFXN3 sequence were made. *pSP64-SFXN3 was used as template DNA for PCR. As shown in the schematic, primers were designed to amplify pSP64-SFXN3, excluding the region of SFXN3 to be removed for each truncation. In the schematic shown, the region between the two solid green lines would be removed. An EcoR1 restriction site was added at the 5' end of primers.*

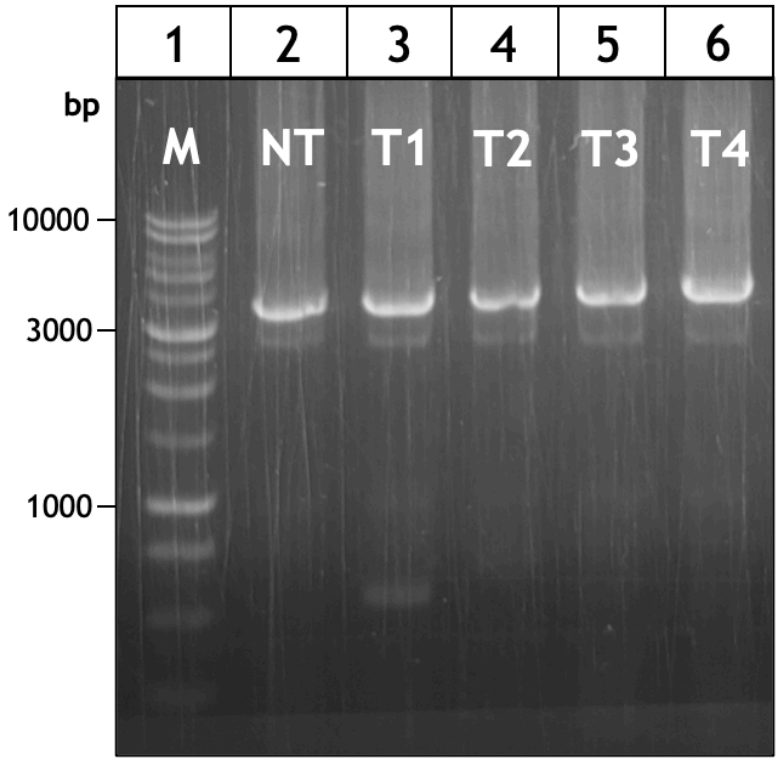

Fig. 5.6: Agarose gel electrophoresis of pSP64-SFXN3 truncations. *pSP64-SFXN3 was amplified via PCR using primers which exclude the unwanted region of SFXN3 for each truncation. The same forward primer was used for each*

amplification (ID: FRW_SFXN3_ECOR1). To generate each truncation, the following reverse primers were used, as detailed in table 3.3: for NT (ID: REV_SFXN3NT_ECOR1), T1 (ID: REV_SFXN3T1_ECOR1), T2 (ID: REV_SFXN3T2_ECOR1), T3 (ID: REV_SFXN3T3_ECOR1) and T4 (ID: REV_SFXN3T4_ECOR1). PCR products were visualised via agarose gel electrophoresis. A 1kB DNA ladder was run in lane 2, labelled 'M'. 1000, 3000 and 10000bp markers are labelled. SFXN3 truncations were run in lanes 2-6.

5.2.4 Import of SFXN3 truncations into wild-type mitochondria

Following cloning into pSP64, SFXN3 truncations were transcribed and translated as ^{35}S-radiolabelled precursors. To test if SFXN3 truncations could be imported into mitochondria, radiolabelled proteins were incubated with isolated wild-type mitochondria (from *S. cerevisiae* strain D273-10B) for 15 minutes at 30°C. As demonstrated in **fig. 5.7A-E** (lane marked 3%), the full-length protein (SFXN3-WT), SFXN3-NT, and SFXN3-T3 truncations were successfully translated. SFXN3-WT ran at the correct size of 35.4kDa, SFXN3-NT ran at ~17kDa and SFXN3-T3 at ~28kDa. For SFXN3-WT and SFXN3-T3, lower molecular weight products were visualised (**fig. 5.7 A and C**). These may have been caused by degradation of the protein.

Furthermore, **fig. 5.7** demonstrates that all truncations and SFXN3-WT were successfully imported into wild-type mitochondria in the presence of the membrane potential ($\Delta\Psi$+). Loss of the membrane potential ($\Delta\Psi$-) reduced level of SFXN3-WT import by ~75% (**fig. 5.8**), suggesting efficient import of SFXN3 relies on the IMM potential. In contrast, loss of the membrane potential did not appear to hinder import of SFXN3-NT and SFXN3-T3 truncations to the same extent (**fig. 5.8**). Thus, suggesting said truncations are less reliant on the IMM potential for mitochondrial import. However, further study must be conducted to confirm this, in most cases, truncation import quantifications shown in **fig 5.8** are based on single repeats and may not be reproducible.

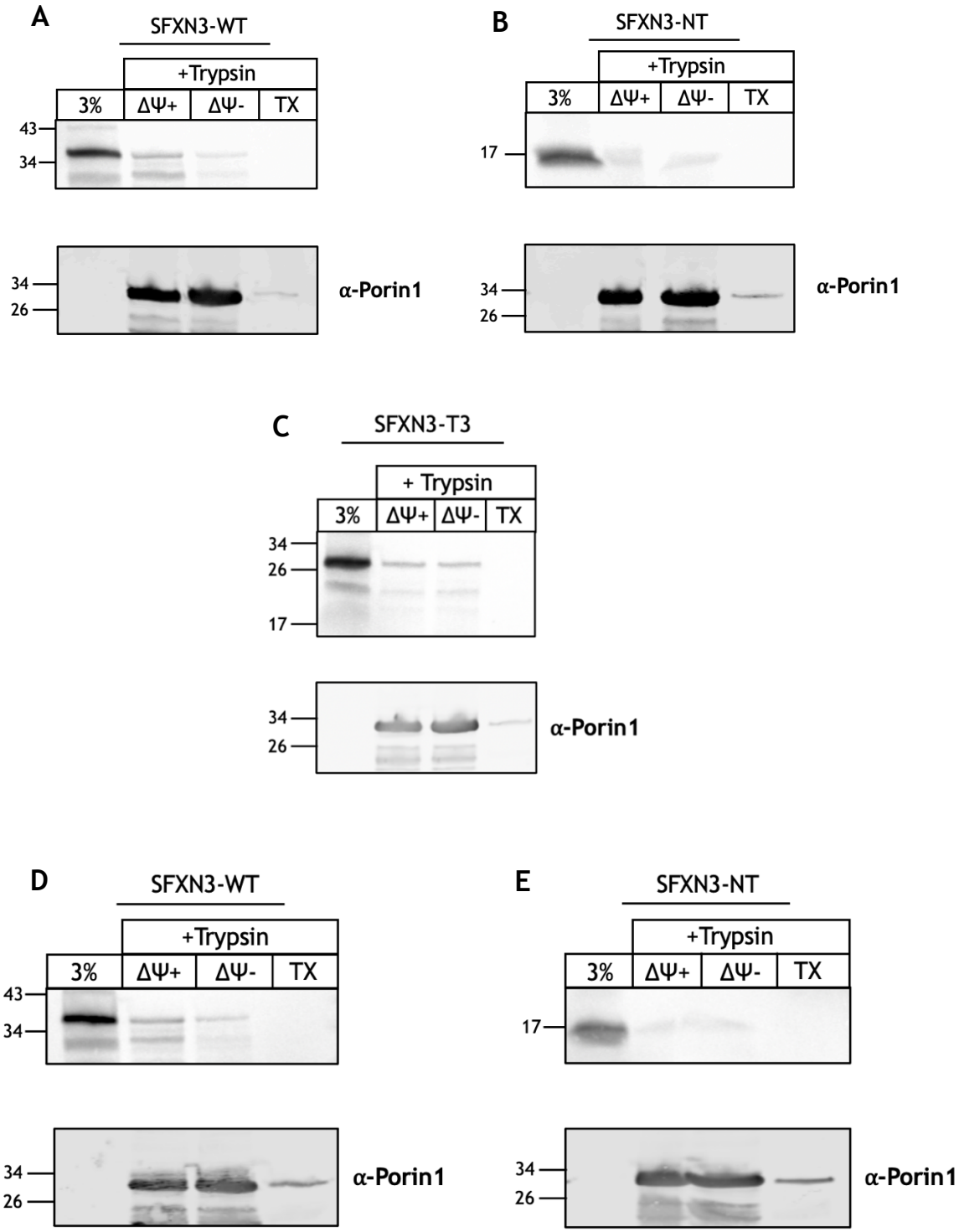

Fig. 5.7: Import of (A) wild-type SFXN3, (B) SFXN3-NT, and (C) SFXN3-T3 truncations into WT mitochondria. *S^{35}-radiolabelled SFXN3, SFXN3-NT and SFXN3-T3 were imported into WT mitochondria for 15 minutes in the presence ($\Delta\Psi$+) or absence ($\Delta\Psi$-) of the IMM potential. To remove unimported material, mitochondria were treated with trypsin. Mitochondria loaded in lane TX were treated with triton-X after import in the presence of the membrane potential ($\Delta\Psi$+), which shows that imported material can be completely degraded if the mitochondria are solubilised with a strong detergent. 3% of the radiolabelled*

protein added to each import reaction was run in the lane marked '3%'. Yeast Porin1 levels were probed for via Western Blotting to assess protein loading across lanes. (D) and (E) show results of an independent repeat of SFXN3-WT and SFXN3-NT import.

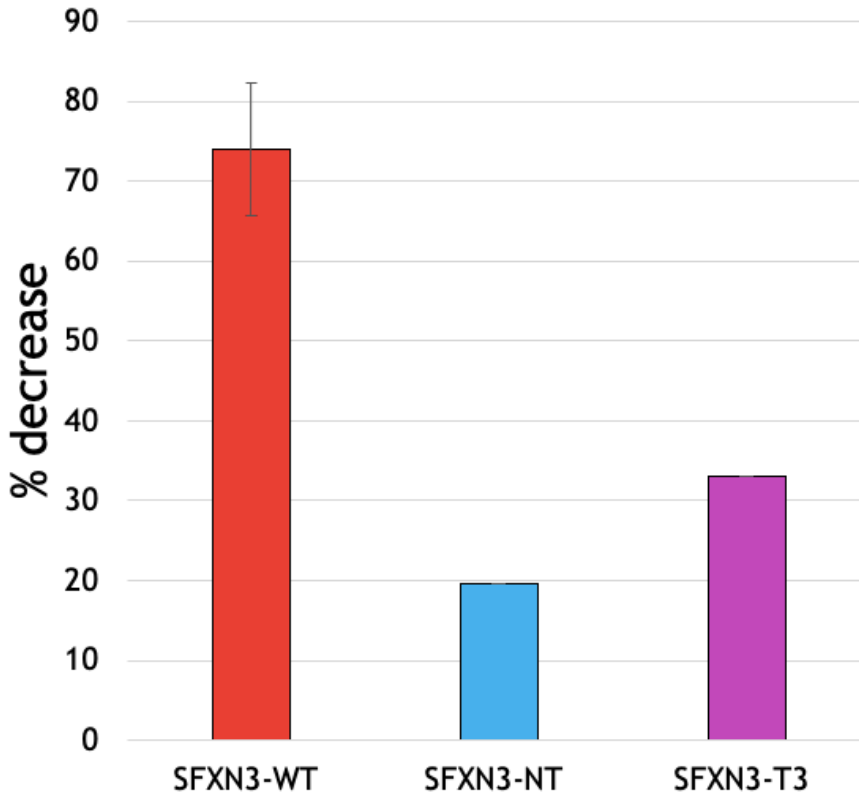

Fig. 5.8: Percentage decrease in import of SFXN3-WT and SFXN3 truncations upon dissipation of the membrane potential. *The intensities of radioactive bands in $\Delta\Psi$+ and $\Delta\Psi$- lanes of fig. 5.7A-E were normalised to that of the loading control (α-Porin1). Percentage of protein imported was measured relative to band intensity in corresponding '3%' lanes, and % decrease in import upon dissipation of the membrane potential calculated via comparison of $\Delta\Psi$+ and $\Delta\Psi$- lanes for each import. % decrease for the WT is an average of 2 repeats (n = 2), error bar is SEM. All other % decreases shown are from a single repeat (n = 1). NT (first repeat) showed an increase in import in the absence of the membrane potential, but this result was not reproducible thus it was excluded.*

To compare import of truncations to SFXN3-WT import, import levels were quantified using ImageJ **(fig. 5.9)**. As shown in **fig. 5.9,** SFXN3-T3 import was

only slightly reduced relative to SFXN3-WT import. This suggests that predicted TR4 and the C-terminal extension of SFXN3 are not necessary for efficient import into mitochondria. In contrast, SFXN3-NT import was reduced by ~50% in comparison to the wild-type protein. This suggests that the region between TR1 and TR3 may play a role in SFXN3 import. However, as SFXN3-NT did import into mitochondria, it must contain some targeting information.

Nonetheless, overall, these results suggest that TR4 and the C-terminal extension are dispensable for import whereas the N-terminal domain and TR1-TR3 possess mitochondrial targeting information. However, due to the discussed problems with cloning, there was not enough time to complete repeats of these experiments or import the additional truncations shown in **fig. 5.1.** It must be acknowledged that reproducibility of results has to be assessed before we can reach any definitive conclusions here.

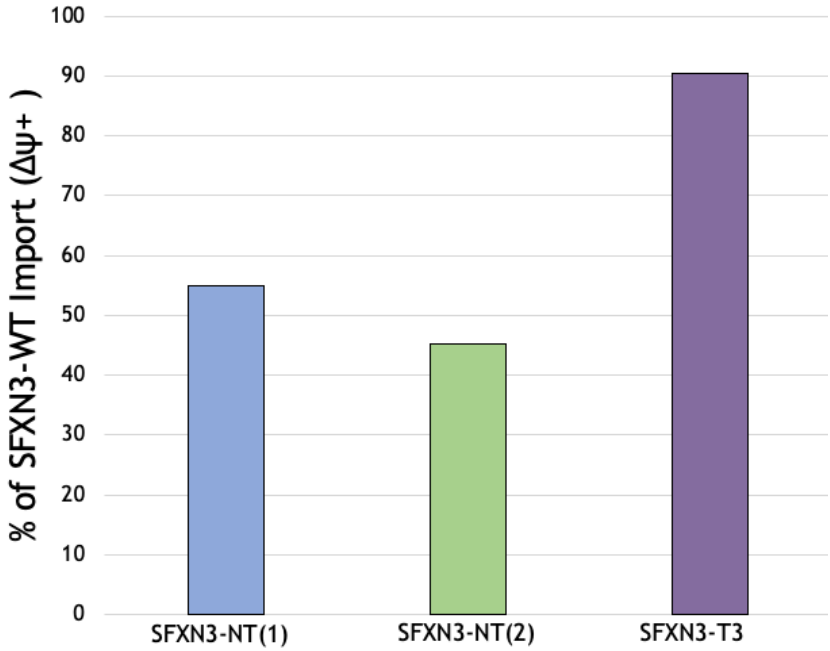

Fig. 5.9: Quantification of import of SFXN3 truncations shown as a percentage of SFXN3-WT import (%). *Radioactive bands were quantified using ImageJ and import of each truncation (in the presence of the membrane potential, $\Delta\Psi$+) is shown as a percentage of SFXN3-WT import (also $\Delta\Psi$+). SFXN3-NT (1) and (2) represent two independent repeats of SFXN3-NT import. Error bars (representing standard deviation) should be included to understand*

the amount of variation in data collected, yet this could not be done due to lack of time to repeat experiments.

5.3 Results: Interaction of human SFXN3 and the Tim9/10 complex

5.3.1 Purification of yeast Tim9/10 complex

Previous work utilised a peptide spot array to characterise interaction of AAC and Tim9/10 (Curran et al., 2002; Vergnolle et al., 2002). Therefore, due to cloning difficulties, the decision was made to simultaneously perform a peptide spot array to identify sequence regions of SFXN3 involved in mitochondrial import by an alternative means.

To initiate study into the Tim9/10-SFXN3 interaction, yeast Tim9 and Tim10 proteins were purified from *E.coli*. 6x-His-tagged Tim9 and Tim10 were overexpressed from pET28 and pRSET plasmids respectively. Tim9 and Tim10 proteins were known to aggregate into inclusion bodies, thus they must be released before progressing with purification. Purification of Tim9 via affinity chromatography on an Ni-NTA column saw success, as indicated by the band visualised in the elution (E) column of **fig. 5.10**. Subsequently, Tim9 was further purified via fast protein liquid chromatography (FPLC) (**fig. 5.11**). The additional band observed at ~26kDa was likely contaminating chaperone GrpE. GrpE may have co-purified with Tim9 due to protein misfolding.

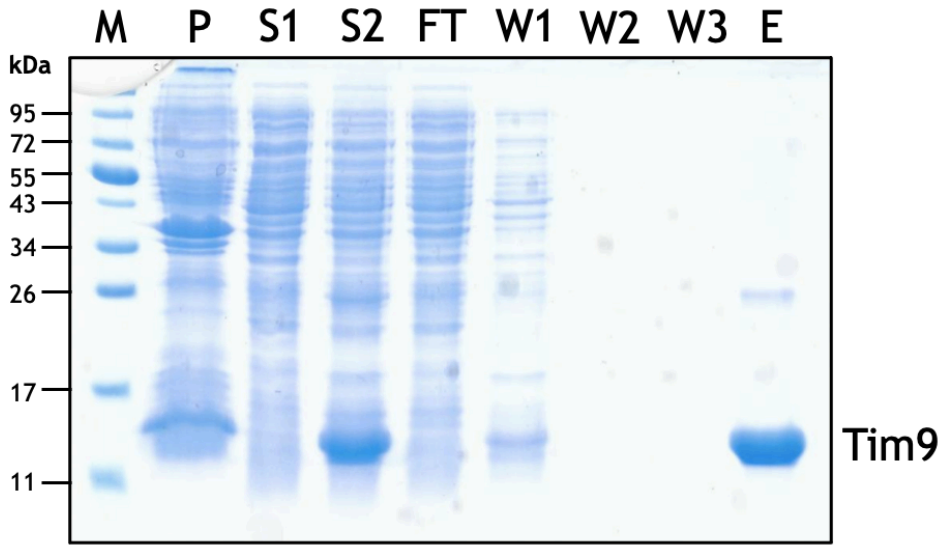

Fig. 5.10: Purification of 6xHis-tagged Tim9 from inclusion bodies, using Ni-NTA beads. *Inclusion bodies were denatured, incubated in the shaking incubator for two hours and then centrifuged to collect released protein in the supernatant. A sample was taken from the pellet (P) and supernatant (S1, S2). The supernatant was then added to an Ni-NTA column and the flow through (FT) collected. The column was washed three times and each elution collected (W1, W2, W3). Tim9 was then eluted from the column (E). Supernatant, pellet, and a sample of each elution was run on an SDS-PAGE gel and the gel Coomassie-stained for protein visualisation. Protein blue standard (Promega) was run in the lane marked 'M' to allow size estimation of bands.*

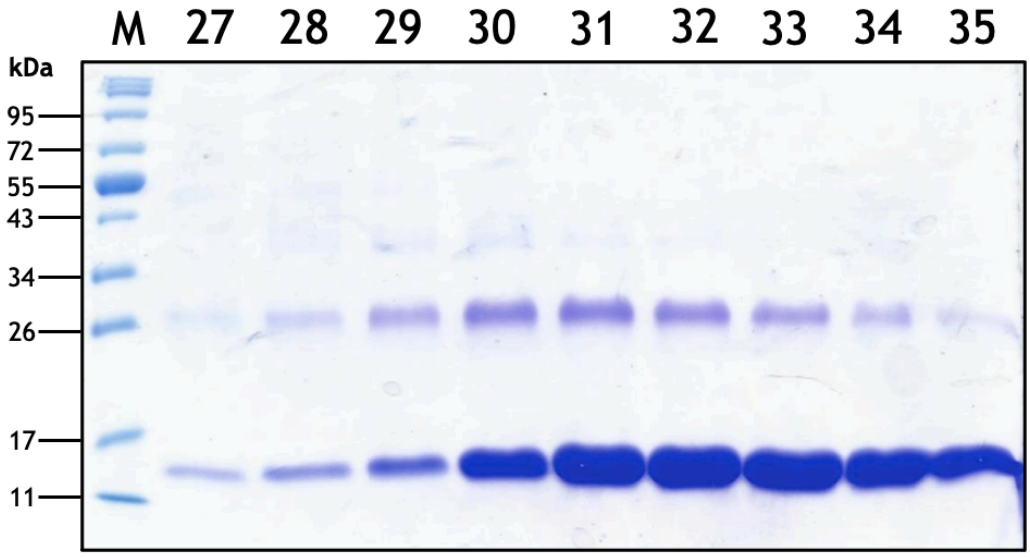

Fig. 5.11: FPLC fractions of 6xHis-tagged Tim9 which showed peaks on the FPLC chromatogram. *The elution containing Tim9 was further purified via size-exclusion chromatography using a Superdex 75 column. Samples were taken from fractions which showed high peaks (absorbance at 280nm) and were run on and SDS-PAGE gel which was subsequently Coomassie stained. Protein blue standard (Promega) was run in the lane marked 'M' to allow size estimation of protein bands. Subsequent lanes are numbered according to fraction numbers.*

The purification of Tim10 was not so straightforward. Following release from inclusion bodies, as for Tim9, Tim10 was purified by affinity chromatography on Ni-NTA beads **(fig. 5.12)**. In contrast to Tim9, a very faint band representing

Tim10 was observed in the elution column **of fig. 5.12.** Most of the protein was lost in the flow through, which would suggest that the 6xHis-tag was not binding to the nickel ions of the Ni-NTA beads. To confirm that Tim10 was his-tagged, samples were taken as for fig. 5.12, an SDS-PAGE gel run, and proteins transferred to a nitrocellulose membrane for immunoblotting with anti-His tag antibody (**fig. 5.13**). As shown in the 'E' lane of **fig. 5.13**, the 6x-His tag was detected at a molecular weight which appears to correspond to Tim10 (~13 kDa). However, this band is very faint and not detected in any other lane, which may indicate a problem with his-tagging. It should be noted that bands at ~10kDa in each lane are an anomaly and were continually seen any time an SDS-PAGE gel was run in the Tokatlidis lab, regardless of the antibody used for detection.

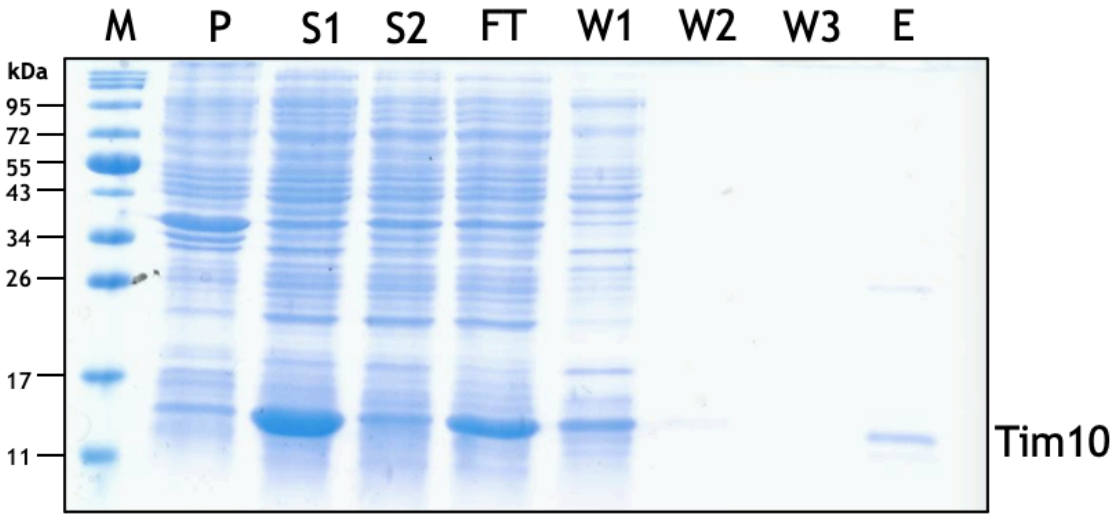

Fig. 5.12: Purification of 6xHis-tagged Tim10 from inclusion bodies, using Ni-NTA beads. *Inclusion bodies were denatured, incubated in the shaking incubator for two hours and the released protein (Tim10) collected in the supernatant via centrifugation. Samples were taken from the supernatant (S1, S2) and pellet (P) before adding the supernatant to an Ni-NTA column and collecting the flow through (FT). The column was washed three times and each elution collected (W1, W2, W3). Tim10 was eluted from the column (E). P, S1, S2 and a sample of each elution was run on an SDS-PAGE gel which was subsequently stained using Coomassie blue. Protein blue standard (Promega) was run in the lane 'M' to permit size estimation of bands.*

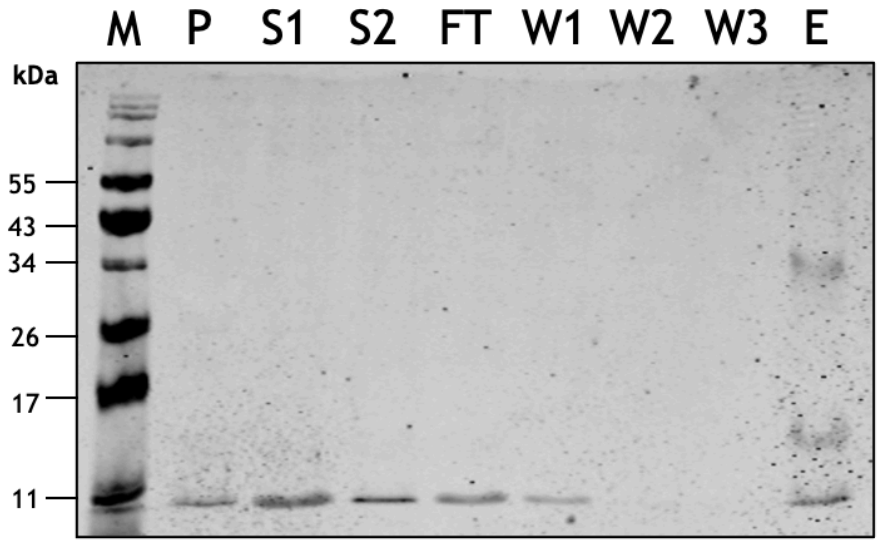

Fig. 5.13: Immunoblot for presence of the 6xHis-tag on Tim10. *Inclusion bodies were denatured, incubated at 30℃ for 2 hours and centrifuged to collect his-tagged Tim10 in the supernatant. Ni-NTA beads were used to affinity purify Tim10. Due to issues with purification, samples from the pellet (P), supernatant (S1, S2) and each elution step of the affinity purification (flow-through (FT), washes 1-3 (W1, W2, W3), protein elution (E)) were run on an SDS-PAGE gel. Protein from the gel was transferred to a nitrocellulose membrane and the membrane probed using anti-His tag antibody. Protein blue standard (Promega) was run in the lane marked 'M'.*

Following on from the immunoblot, the decision was made to send the Tim10-His-pRSET vector for sequencing. Sequencing results were aligned to the sequence of yeast Tim10 using Clustal omega (**fig. 5.14)**. The alignment revealed that there had likely been alternative translation, as the his-tag was not placed after the first methionine of the Tim10 sequence. Therefore, in the interest of time, Tim10 which had previously been prepared in the Tokatlidis lab was incubated with purified Tim9 for 2 hours at 4°C (at pH 8). This led to purification of the Tim9/10 complex, verified via FPLC (**appendix fig. 4).** 0.4mg/mL of the complex was obtained by this means, a sufficient amount for downstream applications.

Affinity chromatography, immunoblotting and sequencing were performed independently. Recombinant protein expression and FPLC were conducted in collaboration with Erik Lacko, a technician in the Tokatlidis lab.

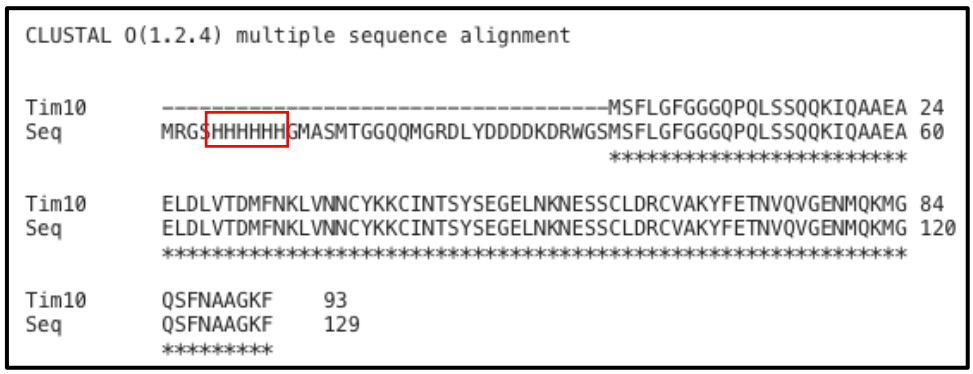

Fig. 5.14: Alignment of sequenced pRSET-Tim10 to S. cerevisiae Tim10 sequence (SGD ID: S000003530). *pRSET-Tim10 was sequenced by Eurofins Genomics. Sequencing results were translated to the corresponding protein sequence using ExPasy translate. The protein sequence ('Seq') was then aligned to that of S. cerevisiae Tim10 ('Tim10') using Clustal Omega. Conserved residues are indicated by the presence of an asterisk (*). Position of the 6xHis-tag is indicated by a red box.*

5.3.2 Sequences of SFXN3 recognised by the Tim9/10 complex

Following purification of the Tim9/10 complex, a peptide spot array was then used to identify the sequences of SFXN3 recognised by the complex. Briefly, the peptide spot array consisted of 104 13-amino acid peptides (which overlapped by 10 amino acids) covering the entire 321-aa sequence of SFXN3, immobilised on a cellulose membrane. A schematic of the peptide spot array is shown in **fig. 5.15 A** and the sequence of each peptide can be found in **appendix fig. 5.**

Purified Tim9/10 complex was incubated with the SFXN3 peptide spot array. Subsequently, Tim9/10 which had bound to the array was transferred to a PVDF membrane and detected via Western blotting using anti-Tim10 and fluorescent secondary antibodies (**fig. 5.15B**). As demonstrated in **fig. 5.15,** binding of Tim9/10 to the array was undetectable. The complex bound to a peptide 23 but

did not bind to any neighbouring peptides (which overlap in sequence). Thus, this spot is likely indicative of non-specific binding of Tim9/10.

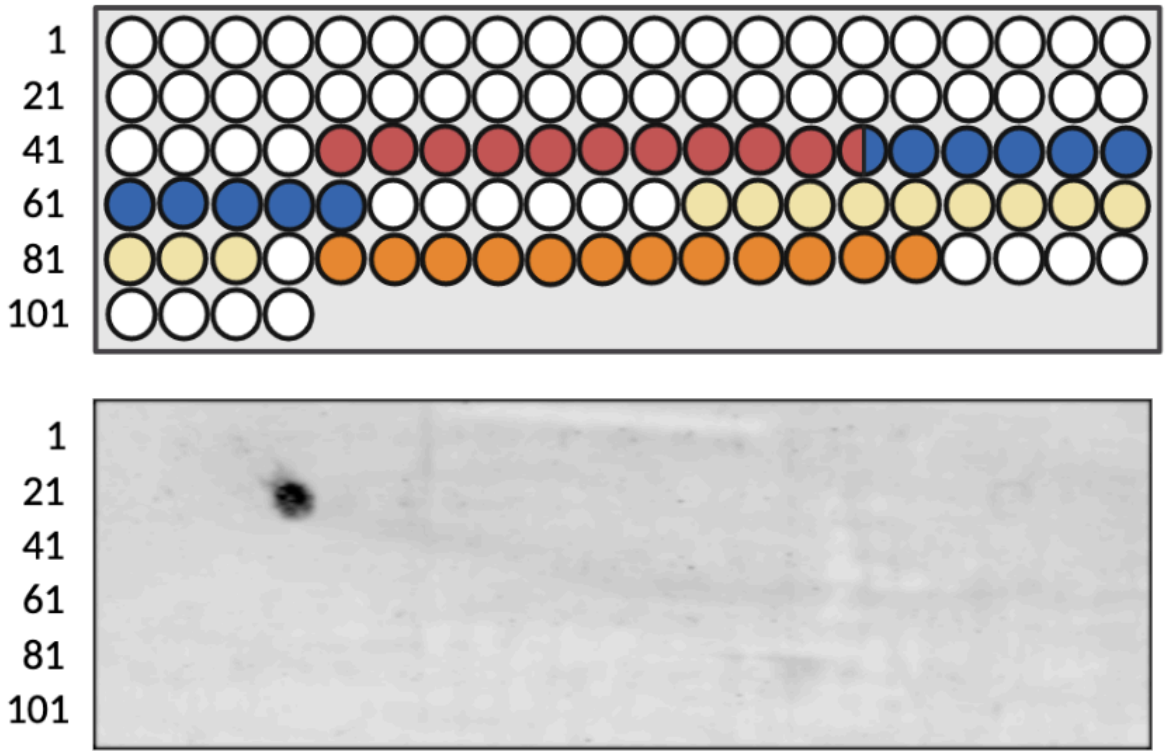

Fig. 5.15 Binding of yeast Tim9/10 complex to human SFXN3 peptide spot array. ***(A)*** *Schematic of SFXN3 peptide spot array. Each spot in the diagram corresponds to one 13mer peptide on the peptide spot array, of which there are 104 in total. Number of the first spot in each row is labelled at the left. Numbers correspond to peptide sequences provided in appendix fig. 5. Spots which include residues of predicted TRs are coloured red (for TR1), blue (for TR2), yellow (for TR3) or orange (for TR4).* ***(B)*** *Results of SFXN3 peptide spot array assay. Tim9/10 complex was incubated with SFXN3 peptide membrane for 1 hour at 4℃. Bound Tim9/10 was transferred from the peptide membrane to a PVDF membrane three times. Tim9/10 was detected via Western blotting using anti-Tim10 primary antibodies and fluorescent detection. Results shown are from first PVDF transfer. See appendix fig. 6 for results of additional transfers.*

The peptide spot array was repeated several times to no avail. Therefore, attempts were made to troubleshoot the protocol. Foremost, ability of anti-Tim10 to detect the complex was assessed by spotting purified Tim9/10 on a

PVDF membrane and immunoblotting with anti-Tim10 (**fig. 5.16**). As shown in **fig. 5.16**, Tim10 antibody successfully detected presence of the Tim9/10 complex. This suggests that lack of signal detection on the peptide spot array was not due to issues with the antibody or antibody concentration. Therefore, it was thought that perhaps the Tim9/10 complex was not binding the peptides.

Fig. 5.16: Tim9/10 complex detection on PVDF membrane using anti-Tim10 antibodies and fluorescent detection. *An arbitrary volume of purified Tim9/10 complex was spotted onto a PVDF membrane. The membrane was incubated with anti-Tim10 antibody overnight at 4°C. To detect anti-Tim10 antibody, the membrane was incubated with fluorescent secondary antibody and fluorescence visualised using the LI-COR odyssey CLX.*

To aid binding, Tim9/10 complex was incubated with the peptide spot array in protein incubation buffer described by Vergnolle et al. (2005) for an increased amount of time (overnight at 4°C). As demonstrated in **fig. 5.17,** binding of the Tim9/10 complex to additional peptides was detected by this means. This increased confidence that Tim9/10 was binding SFXN3, however the signal detected was very weak. Therefore, the decision was made to visualise Tim10 antibody binding via HRP-conjugated secondary antibodies and chemiluminescent detection due to the increased sensitivity of this method relative to fluorescent detection.

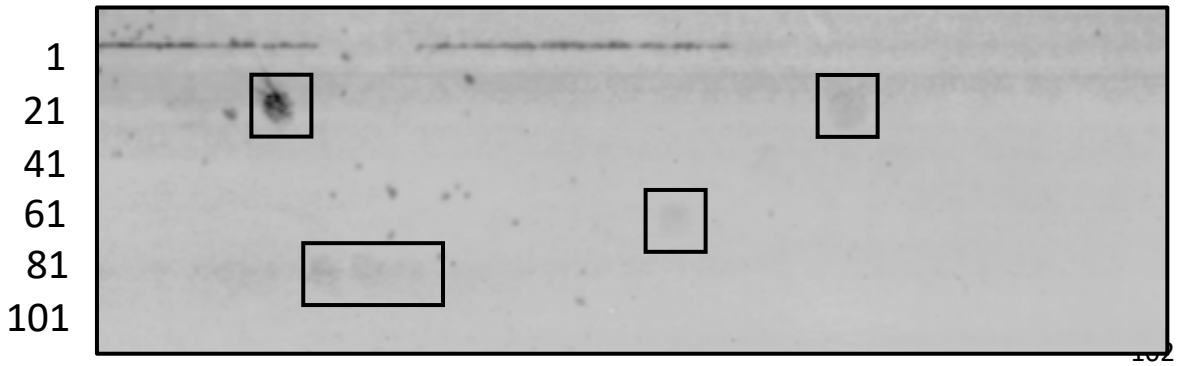

Fig. 5.17: Binding of yeast Tim9/10 complex to human SFXN3 peptide spot array after troubleshooting of assay protocol. *Tim9/10 complex was prepared in protein incubation buffer and incubated with the SFXN3 peptide membrane overnight at 4℃. Tim9/10 complex was transferred from the peptide membrane to a PVDF membrane, three times. Anti-Tim10 antibody and fluorescent detection were utilised to determine which spots of the peptide membrane the Tim9/10 complex bound to. Results shown are from the third transfer. First and second transfer images are shown in appendix fig. 7.*

As shown in **fig. 5.18,** chemiluminescent detection demonstrated that the Tim9/10 complex bound several peptides. Tim9/10 appeared to bind SFXN3 at the N-terminal domain (peptides 5-8 and 35-37). This may suggest that the N-terminal domain plays a role in mediating interactions of the carrier and Small Tims and/or that an additional TM lies here. Of note, the HPDT/S motif (residues of which are located in spots 23-28) did not appear to interact with Tim9/10. Thus, suggesting that said motif is not a requirement for stage III of carrier import, the step at which IMS Tim9/10 chaperones bind. In addition, binding of Tim9/10 was also detected in TR4 of SFXN3 and the loop connecting TR3 and 4 (peptides 84-87). This region contained several hydrophobic residues which the complex may bind to protect from aggregation (**fig. 5.19**). Interestingly, Tim17, a 4-TM substrate of the carrier pathway, harbours a pre-sequence-like region between its third and fourth TM which, when fused to a non-mitochondrial protein, can direct said protein to the mitochondrial matrix (Káldi et al., 1998). Therefore, sequence and predicted structure of SFXN3 were used to determine if any similar pre-sequence-like region could be identified at the Tim9/10 bound loop. A short sequence within said loop formed an amphipathic helix (**fig. 5.20**). Therefore, it is tempting to speculate that the amphipathic helix bound by Tim9/10 is involved in mitochondrial targeting of SFXN3.

On the other hand, the Tim9/10 complex did not bind to TR1, TR2 or TR3 of SFXN3 (**fig. 5.18**). Finally, it should be noted that no neighbouring peptides of peptide 23 were bound by Tim9/10, confirming previous beliefs that this spot was the result of non-specific binding. Unfortunately, after the second repeat using chemiluminescent detection, there was an insufficient amount of purified

Tim9/10 complex to complete a third repeat of the assay. Overall, results of this section demonstrate that Tim9/10 may interact with SFXN3 at its the N-terminal domain, a predicted amphipathic helix between TR3 and TR4, and TR4 itself.

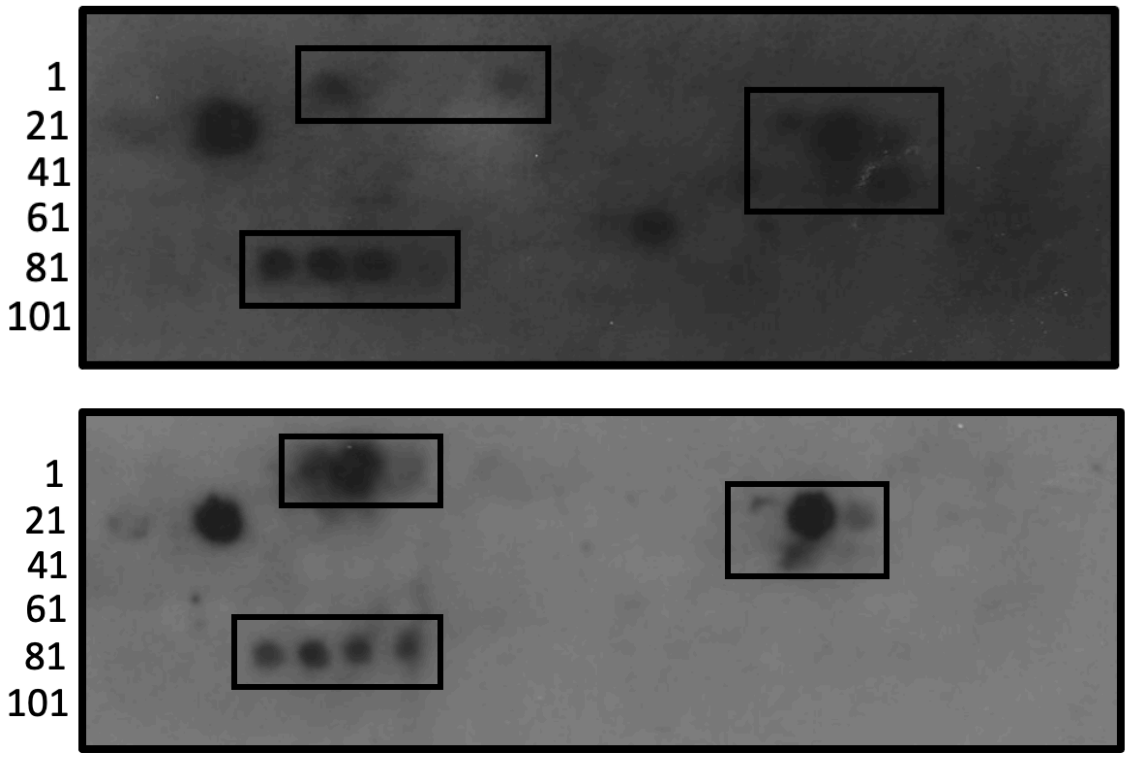

Fig. 5.18: Binding of the yeast Tim9/10 complex to human SFXN3 peptide spot array, visualised using chemiluminescent detection of HRP-labelled secondary antibodies. *Tim9/10 complex was incubated with the SFXN3 peptide membrane overnight at 4℃. Tim9/10 which had bound to the peptides was then transferred to a PVDF membrane three times. PVDF membranes were incubated with anti-Tim10 antibodies and HRP-conjugated secondary antibodies. The membrane was then incubated with chemiluminescent substrate and subsequently exposed to X-ray film to allow the spots bound by Tim9/10 to be visualised. Results shown are from transfer three of two independent repeats.*

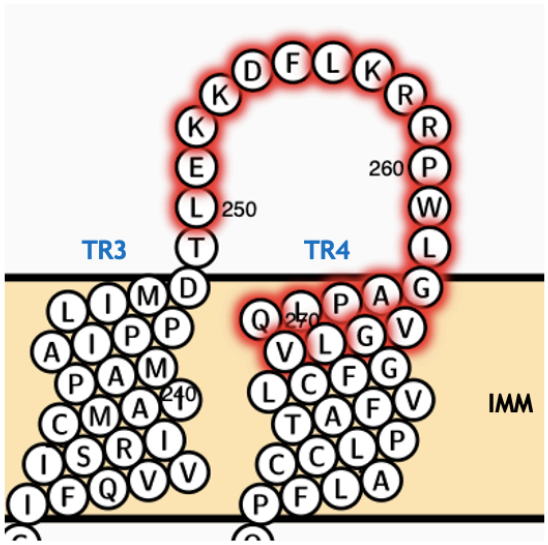

Fig. 5.19: Yeast Tim9/10 binds human SFXN3 at TR4 and the preceding loop region. *Image was created by mapping the sequence of peptide spots 84-87 to the predicted 4TR structure of SFXN3 in Protter (Omasits et al., 2014). Said sequence is highlighted in red. IMM is labelled. Matrix and IMS are not labelled as orientation of the protein at the membrane is unknown.*

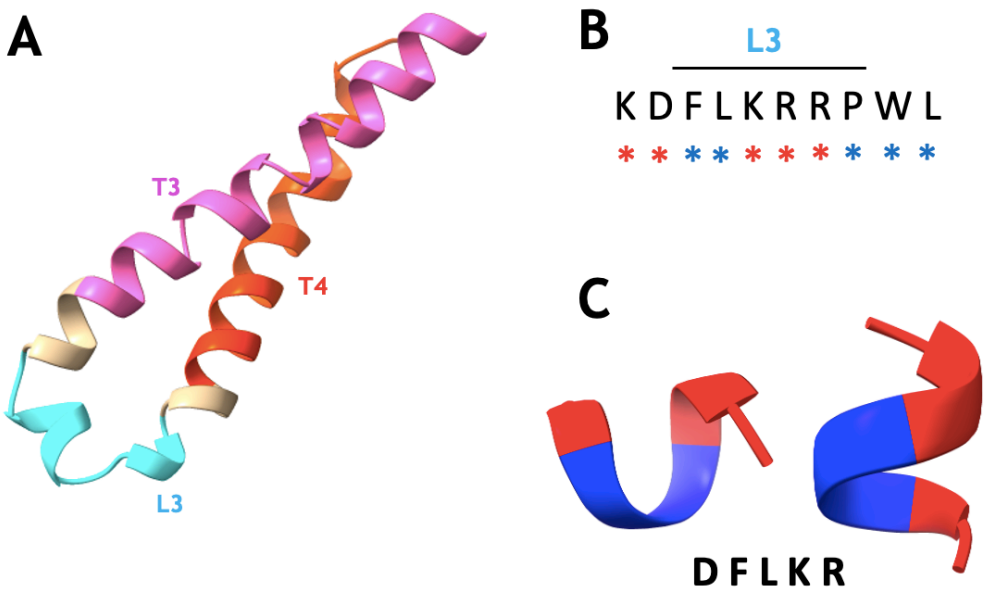

Fig. 5.20: Alpha-Fold predicted structure and sequence of the loop region between TR3 (T3) and TR4 (T4). *AlphaFold structure of SFXN3 was downloaded in PDB format and edited in ChimeraX to show (A) the loop region between TR3 TR3 and TR4, designated L3 as it is the third predicted loop from the N- to C-terminus of SFXN3. The sequence of the entire loop is presented in (B). Polar*

residues are highlighted with a red asterisk (*) whereas hydrophobic residues are shown with a blue asterisk. This is visualised on two orientations of the helix of L3 in (C) and the sequence of this region provided.

5.4 Discussion

It has long been known that SFXN3 does not harbour a mitochondrial pre-sequence (Fleming et al., 2001). Consequently, it has become widely accepted that SFXN3 must possess internal targeting sequences, yet this has not been experimentally explored. Therefore, the aim of this chapter was to identify mitochondrial targeting information of human SFXN3.

5.4.1 Difficulties faced when cloning SFXN3 truncations

Issues with cloning of SFXN3 truncations into pSP64 largely halted the progress of this study. The initial issue encountered was self-ligation of the vector following Sal1 and Xba1 double digest. As aforementioned, the restriction sites of said enzymes lie in close proximity within the MCS of pSP64. Such close proximity can be problematic for a number of reasons. For instance, one restriction enzyme can block the binding of the other. Additionally, after one restriction enzyme has cut at its restriction site, it will remove a number of bases flanking the second restriction site to be cleaved, which can reduce efficiency of cutting. It was difficult to identify when/if either of these issues had arisen, as there would be little difference in molecular weight between a single and double-cleaved plasmid when using Sal1 and Xba1. Thus, it is possible that pSP64 was only cleaved by one restriction enzyme, which would account for the self-ligation seen. To progress, new primers were designed incorporating BamH1 and EcoR1 as restriction sites and the pSP64 vector PCR-amplified to overcome issues with gel extraction (**fig 5.3**). Nonetheless, transformation and colony PCR continuously revealed a high degree of self-ligation. Finally, SFXN3 truncations were cloned from pSP64-SFXN3 as detailed in **fig. 5.5 and 5.6.** Overall, this method is more rapid than conventional PCR cloning and proved relatively fail-proof, seeing success on the second attempt.

5.4.2 Loss of the IMM potential has minimal effect on the mitochondrial import of SFXN3 truncations

Import of full-length SFXN3 into yeast mitochondria shown in **fig. 5.7** supported the prior finding that SFXN3 import requires the IMM potential (Ledahawsky et al., 2022). As a substrate of the carrier import pathway, this result would be expected as the IMM potential is necessary for insertion of carrier proteins into the IMM (Ryan, Müller and Pfanner, 1999).

Relative to wild-type SFXN3, loss of the IMM potential had less impact on import of the N-terminal domain of SFXN3 (SFXN3-NT) and SFXN3 lacking TR4 (SFXN3-T3) (**fig 5.8**). The fact that N-terminal domain import was also largely decreased in the presence of the IMM potential may be responsible for said lesser impact of $\Delta\Psi$ loss (**fig 5.9**). This suggestion cannot be used to explain reduced dependence of SFXN3-T3 on the membrane potential, as $\Delta\Psi$+ import of SFXN3 lacking TR4 only saw a slight decrease relative to wild-type SFXN3 (**fig 5.9**). As a potential explanation, perhaps SFXN3 lacking TR4 is imported into mitochondria but only reaches stage III of the carrier import pathway whereby the carrier protein has been translocated through the TOM complex and is bound by Tim9/10 chaperone complex in the IMS (Ryan, Müller and Pfanner, 1999). Import of SFXN3 to this stage can occur in the absence of the membrane potential (Ledahawsky et al., 2022). Therefore, if SFXN3-T3 only reaches membrane potential-independent stage III, loss of the membrane potential would not alter level of SFXN3 import. To confirm this hypothesis, future study should perform BN-PAGE after SFXN3-T3 import to determine which stage of the carrier import pathway SFXN3-T3 accumulates at. Accumulation at stage III would imply that TR4 is essential for IMM integration.

5.4.3 SFXN3 harbours mitochondrial targeting information in the N-terminal domain and transmembrane regions 1-3

The present study revealed that the N-terminal domain of SFXN3 alone could import into mitochondria and thus must harbour mitochondrial targeting information (**fig 5.7 and 5.9**). This is in stark contrast to SFXN2 targeting, as the N-terminal domain of SFXN2 could not localise to mitochondria *in vivo* (Mon et

al., 2019). Interestingly, the investigation by Mon and colleagues identified mitochondrial targeting information solely in predicted TMs of SFXN2. To my knowledge, this is the only study which has explored SFXN targeting in detail. Perhaps the results of this study differ as an additional TM lies within the N-terminal domain of SFXN3, and it is in fact said TM which contains the information sufficient for mitochondrial targeting. Further to this, loss of TR1 and TR3 impaired efficiency of mitochondrial targeting (**fig 5.7 and 5.9**). This suggests a complexity of SFXN3 targeting, whereby there are various internal mitochondrial signals which work in concert to achieve IMM integration of the protein. This is highly conceivable as targeting signals in all three helix-loop-helix motifs of SLC25 carriers collaborate to permit passage through the carrier import pathway (Wiedemann, Pfanner and Ryan, 2001; Horten, Colina-Tenorio and Rampelt, 2020). Building on this, TR4, the ~33 amino acid C-terminal extension of SFXN3 and F/YNKGL motif within this region were dispensable for import into mitochondria (**fig 5.7 and 5.9**). Similarly, the C-terminal 40 amino acids of SFXN2 could not target mitochondria *in vivo* (Mon et al., 2019).

5.4.4 Issues faced when purifying recombinant yeast Tim9/10 complex

In the present study, Tim9 was successfully purified from *E. coli* in collaboration with Tokatlidis' lab technician Erik Lacko (**fig. 5.10 and 5.11**). However, Tim10 purification was far more troublesome and time-consuming due to incorrect his-tagging of the protein (**fig 5.14**). Without time constraints, Tim9 and Tim10 would have been cloned into expression vectors as part of this study to ensure correct placement of the 6xHis-tag after the start codon of the protein sequences. Nonetheless, recombinant Tim9/10 complex was generated by incubating freshly prepared Tim9 with previously purified Tim10.

Purified Tim9/10 complex was to be used in peptide spot array experiments. In the first instance, 0.4 mg/mL Tim9/10 complex was purified. Ultimately, the study would have benefited from obtaining a higher yield of protein to permit additional repeats of the spot array. As aforementioned, during the protein purification process, Tim9 and Tim10 aggregated into inclusion bodies - likely due to their high hydrophobicity (Mitraki et al., 1991) (**fig. 5.21**). Therefore,

Tim9 and 10 had to be released from inclusion bodies via solubilisation using urea and then subsequently re-folded. This process frequently retrieves a low yield of recombinant protein (Singh et al., 2015). Therefore, in future it may be beneficial to solubilise inclusion bodies using detergent rather than a chaotropic agent as this can improve yield (Kudou et al., 2011).

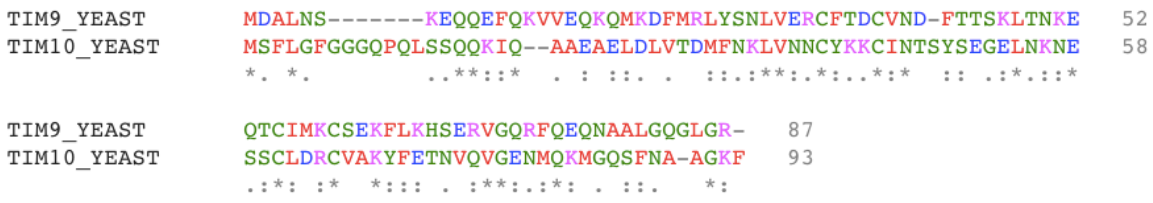

Fig. 5.21: Pairwise sequence alignment of yeast Tim9 and Tim10, showing residue properties. *Yeastgenome.org was accessed to retrieve the protein sequence of yeast Tim9 and Tim10. Protein sequences were aligned in Clustal Omega, and the residues coloured based on their properties. Of interest, red residues are hydrophobic.*

5.4.5 Recombinant yeast Tim9/10 complex binds SFXN3 N-terminal domain and loop region preceding transmembrane region 4

The Tim9/10 complex is required for import of SFXN3, as loss of the complex impairs SFXN3 import levels (Ledahawsky et al., 2022). The present study suggests that recombinant Tim9/10 complex binds the N-terminal domain of SFXN3 (**fig 5.18**). Studies by Vergnolle et al. (2005), Curran et al. (2002) and Vaseljev et al. (2004) all demonstrate that Tim9/10 binds mainly to TMs of AAC. Taking this into consideration, binding to the N-terminal domain of SFXN3 may suggest the presence of an additional TM here. Interestingly, TOPCONS-identified TM1 (**fig. 4.1),** which was not detected via other prediction tools, spans peptides 29-40, overlapping with the peptides bound by Tim9/10. This may suggest TOPCONS predictions were in fact correct and that SFXN3 has 5 TMs.

Moreover, Tim9/10 bound to TR4 and the loop region preceding this domain (**fig 5.18**). A similar pattern of Tim10 binding to TMs and a single loop domain of AAC was detected by Vergnolle and colleagues (2005). In the present study, structure

analysis showed that the loop preceding TR4 of SFXN3 formed an amphipathic helix **(fig 5.20)**. It was previously suggested that this helix could contain mitochondrial targeting information. However, the SFXN3-T3 fragment which targeted mitochondria successfully in **fig. 5.7** was designed such that it truncated this helix at the position shown in **fig. 5.22,** which would disrupt its amphipathic nature. Therefore, the entirety of the amphipathic helix preceding TR4 is not a requirement for mitochondrial import. Nonetheless, as suggested previously, SFXN3-T3 truncation may localise to stage III of the carrier import pathway – the stage at which SFXN3 interacts with the Tim9/10 complex. It may be possible that SFXN3-T3 does not import beyond stage III due to impairment of the Small Tim interaction as a result of the loss of some of the loop/TR4 residues identified to bind SFXN3 by the peptide spot array.

Interestingly, TR1-3 did not show Tim9/10 binding **(fig. 5.18)**. This does not rule out the possibility that the complex does interact with these TRs as it is known the Tim9/10 interacts with carrier proteins by sampling different conformations at its binding cleft (Weinhaupl et al., 2018). Yet, using a peptide spot array, we cannot assess binding to SFXN3 in its native state, potentially masking interactions of Tim9/10 with SFXN3 TMs which occur *in vivo*. To investigate rapid conformational dynamics of the SFXN3-Tim9/10 interaction, NMR should be used.

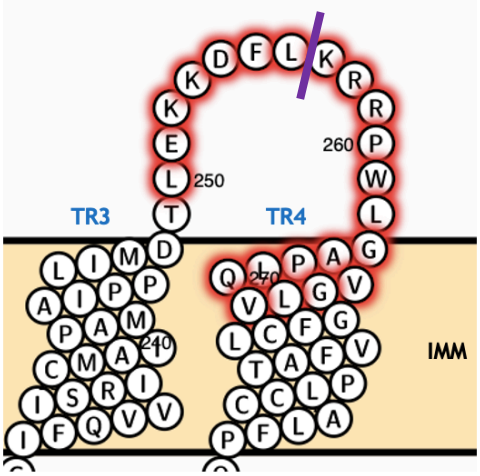

Fig. 5.22: Region of human SFXN3 bound by yeast Tim9/10, showing the location of SFXN3-T3 truncation. *Tim9/10 bound to the loop of SFXN3 at the residues highlighted in red. The purple solid line shows where the sequence was truncated to generate the SFXN3-T3 truncation.*

5.4.6 Overall conclusions

Import experiments and use of a peptide spot array suggest that there may be an additional TM within the N-terminal 144 amino acid domain of SFXN3, as previously predicted by TOPCONS**.** This must be confirmed via further study. The N-terminal domain likely contains mitochondrial targeting information and interacts with the Tim9/10 complex. In contrast, TR1, TR2, TR3 and the loop regions connecting such TRs do not appear to interact with Tim9/10 but do enhance import efficiency, and thus may contain mitochondrial targeting information. Finally, TR4 and the preceding loop region are dispensable for mitochondrial import of SFXN3 but do interact with Tim9/10 and thus may be required for completion of stage III of the carrier pathway and subsequent IMM integration (stage IV). Overall, this chapter has identified sequence regions involved in SFXN3 import. However, the further study suggested should be conducted to define the precise sequences required for IMM targeting of SFXN3.

5.4.7 Future study

Future study must perform import repeats and import of truncations SFXN3-T1, SFXN3-T2 and SFXN3-T4 detailed in **fig. 5.1** to validate results presented and narrow down the precise sequence regions which target SFXN3 to the mitochondria. Subsequently, results should be validated in mammals, via import into mammalian mitochondria, and *in vivo* by conjugating a fluorescent tag (e.g., mCherry) to each SFXN3 truncation and assessing localisation in a mammalian cell line (e.g., Hek293). Moreover, future study should add more detail to the targeting mechanism by determining the intramitochondrial localisation of each truncation as described previously (Vergnolle et al., 2005).

The N-terminal domain targeted mitochondria and contains conserved HPDT/S motif, which adds support to a potential targeting role of said motif. This could be investigated further by mutagenizing the HPDT/S motif to alter its properties (e.g., via alanine scanning mutagenesis) and determining how this alters import. Additionally, the present study demonstrated that the F/YNKGL motif was not vital for targeting nor Tim9/10 interaction. Therefore, a functional role may be

more likely. It would be interesting to mutagenize the F/YNKGL motif and determine if this alters SFXN3 serine transport ability *in vitro* (Kory et al., 2018).

Use of peptide spot arrays to investigate protein-protein interactions has several benefits, such as the low cost, simplicity of experimental procedures and requirement for a low amount of protein (~200 nM) (Szymczak, Kuo and Mrksich, 2017). However, drawbacks of the protocol must be acknowledged. For instance, peptide spot arrays cannot assess interactions as they would occur *in vivo* as we are not working with the 3D structure of a protein, rather we are solely using the primary structure. In addition, each peptide on the array is 13 amino acids in length. This may not be a sufficient size to permit Tim9/10 interaction. Each of these drawbacks could mask further Tim9/10 binding sites on SFXN3. Also, it can be hard to confirm purity of peptides on the peptide array. Therefore, follow-up investigation is often required to confirm location of peptide array-identified interaction sites (Kudithipudi et al., 2014). This may be done by assessing the interaction of SFXN3 and Tim9/10 via a biochemical approach such as isothermal titration calorimetry or surface plasmon resonance.

Chapter 6: Characterising the function of human SFXN3 and yeast FSF1

6.1 Introduction

An early study proposed that an SFXN1 loss-of-function mutation was causative for sideroblastic anaemia of flexed-tail (f/f) mice, a disorder characterised by accumulation of iron in the mitochondria (Fleming et al., 2001). Taking this into consideration alongside their predicted TM structure and IMM localisation, SFXNs were quickly presumed to be mitochondrial iron transporters. Transport of iron into the mitochondria is crucial for two key processes: Fe-S cluster and heme biosynthesis (Paul et al., 2017). Consequently, various studies hypothesised a role for SFXNs in said processes. However, the relationship between SFXNs and iron homeostasis has been challenged for reasons such as: the belief that Madh5 mutation, not SFXN1, is responsible for SA of f/f mice; contrasting results on the effect of SFXN KO on mitochondrial iron accumulation in cell lines; and the belief that individual SFXNs do not share the same function (Lenox, Perry and Paulson, 2005; Kory et al., 2018; Mon et al., 2019; Paul et al., 2019; Bao et al.,2021; Chen et al., 2022; Jackson et al., 2022). Similarly, the role of SFXNs in respiration has been disputed as the effect of KO/KD of individual SFXNs on mitochondrial respiration and respiratory complex activities differs across studies (Hildick-Smith et al., 2013; Amorim et al., 2017; Mon et al., 2019; Paul et al., 2019; Chen et al., 2022; Jackson et al., 2022; Tifoun et al., 2022). All contradictory results were identified using SFXN1, SFXN2 or SFXN4 KO/KDs. The effect of SFXN3 loss on respiration and mitochondrial iron homeostasis has not been investigated (Tifoun et al., 2021). Therefore, this chapter aimed to create a SFXN3 knockdown Hek293 cell line to specifically investigate SFXN3 function.

SFXN3 is the closest human homologue of the sole SFXN of *S. cerevisiae* - FSF1, with the two proteins sharing 37.73% amino acid similarity. FSF1 was originally proposed as an α-isopropylmalate transporter required for *de novo* leucine biosynthesis in yeast (Kovaleva et al., 2006). Further experimentation quickly disproved this, demonstrating rather that the mitochondrial oxalacetate carrier was responsible for α-IPM transport (Marobbio et al., 2008). As a member of the SFXN family, FSF1 is predicted to share function and localisation with

mammalian SFXNs. However, this has not been confirmed experimentally despite the ease and value of using yeast as a model organism. Therefore, a further aim of this chapter was to explore the function of yeast FSF1 as this could uncover a general SFXN family function.

6.2 Results

6.2.1 Knockdown of human SFXN3 expression in HEK293 cells

To initiate investigation into the function of SFXN3, MISSION® shRNA targeting SFXN3 was expressed in HEK293 cells via transient transfection of the pLKO.1-puro-SFXN3 shRNA vector. Following transfection, HEK293 cells were maintained in media containing 1 μg/mL puromycin. After 2 weeks of antibiotic selection, HEK293 cells were grown to ~70% confluency in a T75 flask and the cells lysed using Triton-X100 lysis buffer to allow knockdown success to be assessed via Western blotting **(fig. 6.1)**. As demonstrated in **fig. 6.1,** SFXN3 protein expression was undetectable in WT, non-transfected (TRO) and KD lysates. In contrast, mtHsp70 – a soluble matrix protein – was detectable. This suggests that perhaps Triton-X100 lysis buffer had released soluble proteins from the cell, but it had not completely solubilised the IMM to release membrane-bound proteins (such as SFXN3).

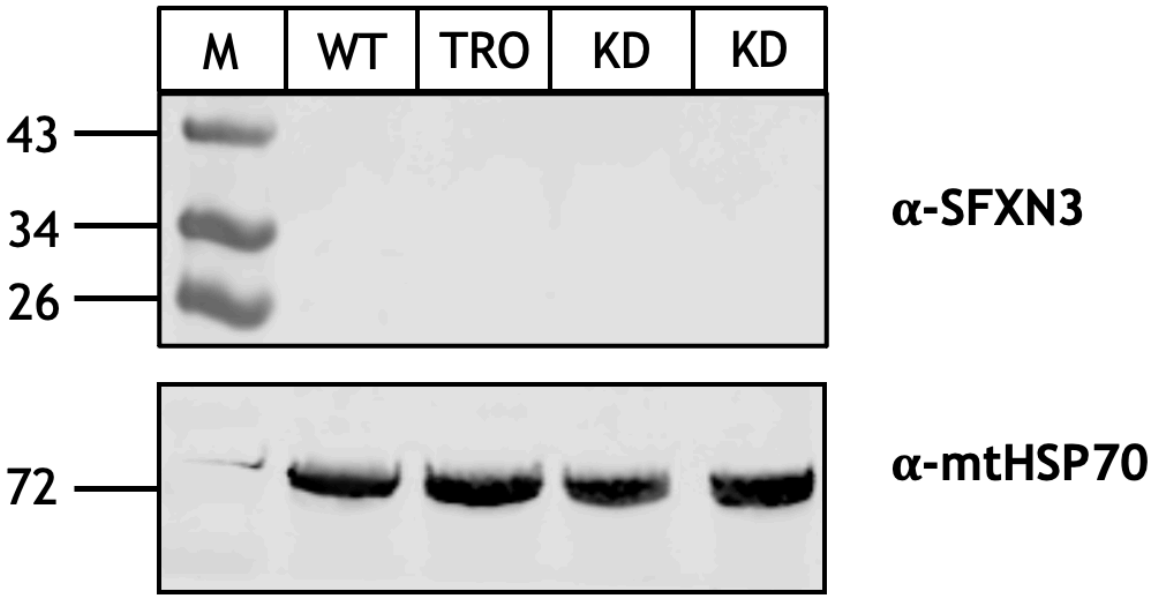

Fig. 6.1: Immunoblot showing protein levels of SFXN3 and mitochondrial (mt) Hsp70 in WT and SFXN3-knockdown HEK293 cells. *HEK293 cells were*

transfected with SFXN3-specific shRNA. Whole cell lysates were prepared by using Triton-X100. Samples were then centrifuged to pellet cell debris. The supernatant (cleared lysate) was analysed via Western blotting for SFXN3 and mtHsp70 protein expression. Proteins levels of non-transfected cells and cells treated with only transfection reagent (no shRNA) were assessed as controls. M = molecular weight marker; WT = non-transfected cells; TRO = transfection reagent only cells; KD = cells transfected with SFXN3-specific shRNA. Two KD lanes are biological replicates. Samples were not loaded in three lanes of the Tris-Tricine gel between the two KD lanes, thus these lanes were removed from the image shown.

In an attempt to completely extract SFXN3 from the IMM of HEK293 cells, RIPA buffer was used to lyse wild-type cells **(fig. 6.2)**. RIPA was selected as a lysis buffer as it contains SDS which is an anionic, denaturing detergent that completely disrupts membranes. In contrast, triton-X100 is non-ionic and non-denaturing. As shown in **fig. 6.2**, SFXN3 levels remained undetectable after Triton-X100 lysis. However, a low level of SFXN3 expression could be detected after RIPA lysis (represented by bands visualised at ~35kDa in lanes B1-B3). Therefore, RIPA lysis buffer was selected for further use. Additionally, as bands representing SFXN3 were very faint, chemiluminescent detection was utilised moving forward in attempt to improve the signal.

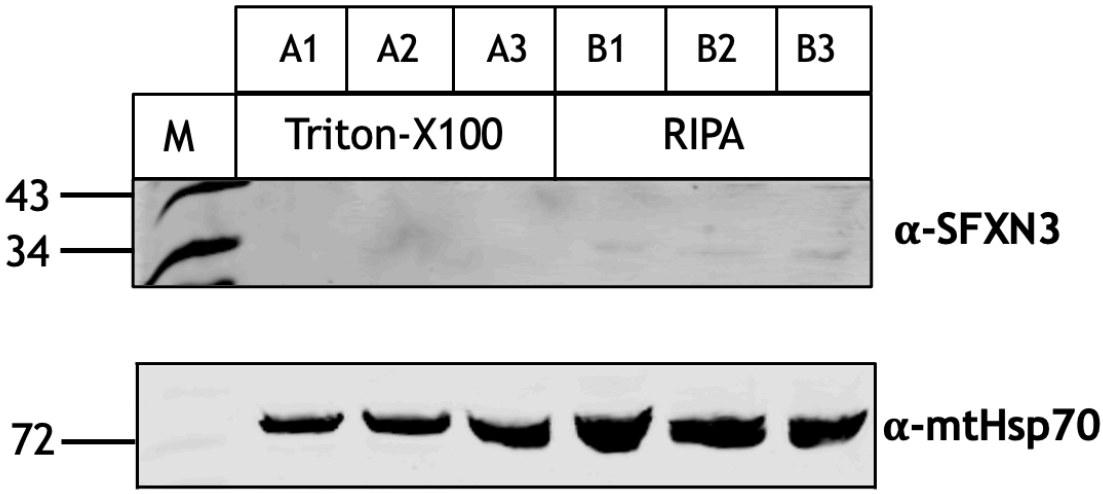

Fig. 6.2: Immunoblot showing protein levels of SFXN3 and mtHsp70 in WT HEK293 cells after lysis with Triton-X100 or RIPA lysis buffer. *HEK293 WT cells were grown to ~70% confluency in a 6-well plate. Cells in wells A1-3 were lysed*

by Triton-X100 lysis buffer whereas cells in wells B1-3 were lysed by RIPA buffer. Whole cell lysates were centrifuged, and the resulting supernatant (cleared lysate) was probed for levels of SFXN3 and mtHsp70 via Western blotting. Three biological replicates for each condition are shown. M = molecular weight marker.

Using RIPA lysis and chemiluminescent detection, levels of SFXN3 were assessed in WT and SFXN3-KD HEK293 cells (**fig. 6.3**). As shown in **fig. 6.3,** levels of SFXN3 may have been slightly reduced in KD cells. However, due to lysis issues, this result was obtained very near the end of the project, and there was no time to conduct independent biological repeats to confirm KD. Additionally, time constraints meant that KD could not be repeated in an alternative cell line (e.g., HeLa) nor investigated via qRT-PCR to assess success of mRNA degradation.

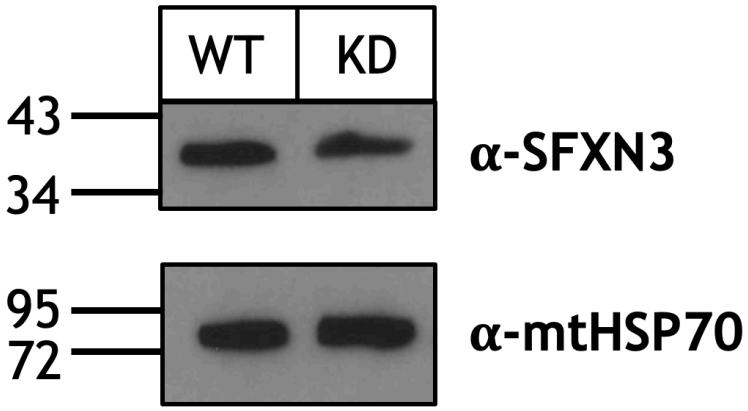

Fig. 6.3: Immunoblot showing protein levels of SFXN3 and mtHsp70 in WT and SFXN3-knockdown HEK293 cells, visualised using chemiluminescent detection. *shRNA-transfected (KD) and non-transfected (WT) HEK293 cells were lysed using RIPA buffer. Whole cell lysates were centrifuged to pellet cell debris. The resulting supernatants (cleared lysate) were probed for levels of SFXN3 and mtHsp70 via Western blotting using HRP-conjugated secondary antibodies and chemiluminescent detection.*

6.2.2 Structure and sequence comparison of human SFXN3 and *S. cerevisiae* FSF1

Due to issues in obtaining an SFXN3 knockdown cell line, our study prioritised characterising function of yeast FSF1. Before progressing with functional

analysis, sequence and structural elements of SFXN3 and FSF1 were compared to understand their similarities and where they diverge.

Foremost, to examine similarities in TM structure of FSF1 and SFXN3, the location of TMs within the sequence of FSF1 was determined using four independent prediction programs (**appendix fig. 8**). As described in chapter 4 (section 4.2.1), SFXN3 was predicted to possess 4 TMs. In contrast, **appendix fig. 8** demonstrates that FSF1 TM predictions varied from 3-5 TMs. The results of all TM predictions were compiled as demonstrated in **appendix table 4** to identify five TRs. Again, TR is used only to refer to these compiled sequence regions and TM used in every other instance.

To examine sequence similarity between SFXN3 and FSF1, the respective protein sequences were aligned using EMBOSS Needle and the position of predicted TRs mapped to the sequence alignment in **fig. 6.4**. As demonstrated in **fig. 6.4**, there were various conserved residues distributed throughout the protein sequences. The locations of TRs, with the exception of FSF1 TR1, were very similar across FSF1 and SFXN3 and contained various conserved residues. Similar to SFXN3, FSF1 harboured the conserved HPDT/S motif in its large N-terminal domain, demonstrating that this motif is conserved not just within, but across species. The F/YNKGL motif conserved across human SFXNs **(fig 4.2)** was not exactly conserved across species, but FSF1 was found to harbour a similar sequence whereby lysine and leucine have been exchanged for arginine and phenylalanine respectively (amino acids with highly similar properties).

```
SFXN3              1 -MGELPLDINIQEPRWDQSTFLGRARHFFTVTDPRNLLLSGAQLEASRNI     49
                       ...:|..|:::.|.|:|.|||:.|||.|||...:::|||..|||.:...|..:|.|
FSF1               1 MASSVPGPIDLPESRYDLSTYWGRIRHCAEISDPTMLLTTEKDLAHAREI     50

SFXN3             50 VQNYRAGVVTPGITEDQLWRAKYVYDSAFHPDTGEKVVLIGRMSAQVPMN     99
                       :..|||.|.:..  |..:.||||...|||..|||||:.|:|..|||:.|..|
FSF1              51 ISAYRHGELKE--TTPEFWRAKKQLDSTVHPDTGKTVLLPFRMSSNVLSN     98

SFXN3            100 MTITGCMLTFYRKTPTVVFWQWVNQSFNAIVNYSNRSGDTPITVRQLGTA    149
                       :.:|..|||.....|...||||||.|||.|..||.:|.:...|:::..|||.|.
FSF1              99 LVVTVGMLTPGLGTAGTVFWQWANQSLNVAVNSANANKSHPMSTSQLLTN    148
                                                  TR1
```

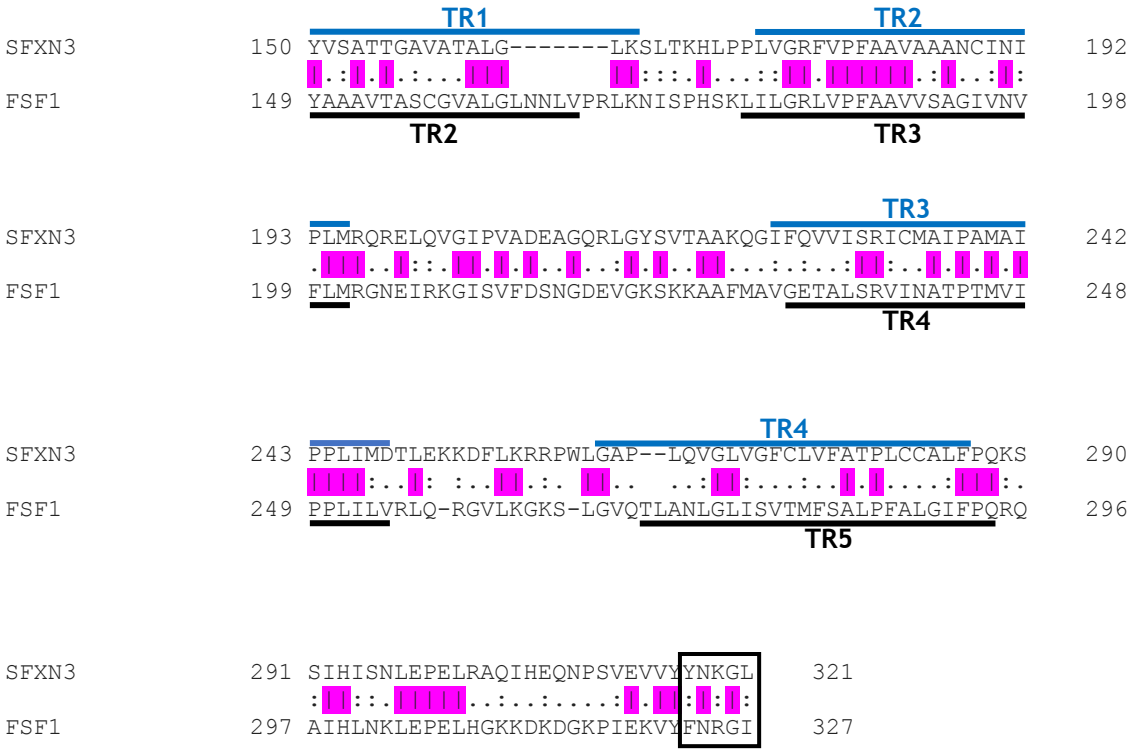

Fig. 6.4: Pairwise sequence alignment of human SFXN3 and S. cerevisiae FSF1 showing predicted TRs. *Protein sequence of SFXN3 (UniProt ID: Q9BWM7) and FSF1 (SGD ID: S000005797) were aligned using EMBL-EBI EMBOSS Needle. Fully conserved residues are indicated by a solid line and are highlighted pink. Conserved residue properties are indicated by a colon (:) where residue properties are highly similar, or a period (.) where residue properties are weakly similar. The position of the conserved HPDT/S and F/YNKGL motif is indicated. Transmembrane domain location was predicted using HMMTOP 2.0, PHOBIUS, MEMSAT-SVM and TOPCONS. The position of TRs within the sequence are shown in blue (for SFXN3) or black (for FSF1).*

To understand the extent of structural similarity, the predicted structure of *S. cerevisiae* FSF1 was determined using AlphaFold and compared to that of human SFXN3. As shown in **fig. 6.5A and B,** the structures of FSF1 and SFXN3 were largely alpha-helical. Interestingly and similar to human SFXNs (**fig 4.5; appendix fig. 2**), FSF1 harboured four beta-strands towards the C-terminal **(fig. 6.5)**. Therefore, suggesting that said structural element is conserved across species.

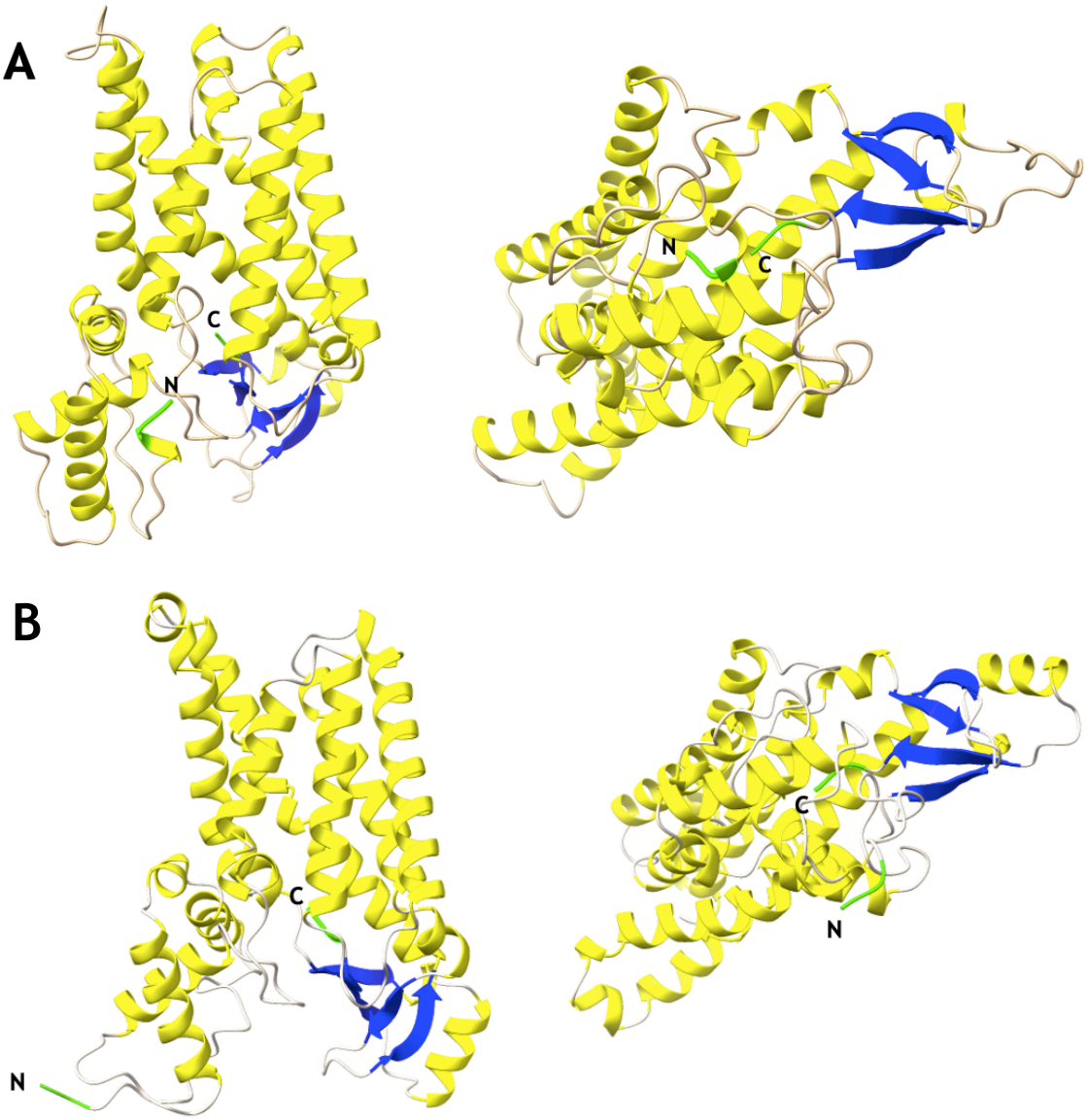

Fig. 6.5: Predicted secondary structure elements of yeast FSF1 and human SFXN3. *The predicted structures of (A) yeast FSF1 and (B) human SFXN3 were obtained from AlphaFold and edited in UCSF ChimeraX to highlight alpha helices (yellow ribbons) and beta strands (blue arrows). Two orientations of each structure are shown. N- and C-termini are labelled and coloured green.*

To further investigate similarities in structure, the five predicted TRs of FSF1 were visualised on the AlphaFold structure (**fig. 6.6**). As was true for SFXN3 (**fig. 4.3**), each predicted TR of FSF1 was helical and found within what appeared to be a bundle-like structure of six helices (**fig. 6.6**). Supporting this, superimposition of the structures of SFXN3 and FSF1 showed that the helical

bundle region was highly similar across these proteins (**fig. 6.7A**). Differences in protein structures appeared to lie in the regions out with said helices **(fig. 6.7B)**. Nonetheless, these regions showed similarities in that they consisted of small helices and beta-strands.

Overall, results presented demonstrate the high similarity of the structure and sequence of SFXN3 and FSF1. Similarities identified across human and fungal SFXNs suggest that there may be conservation of function across species, and thus warrant the use of FSF1 for further investigation in this study.

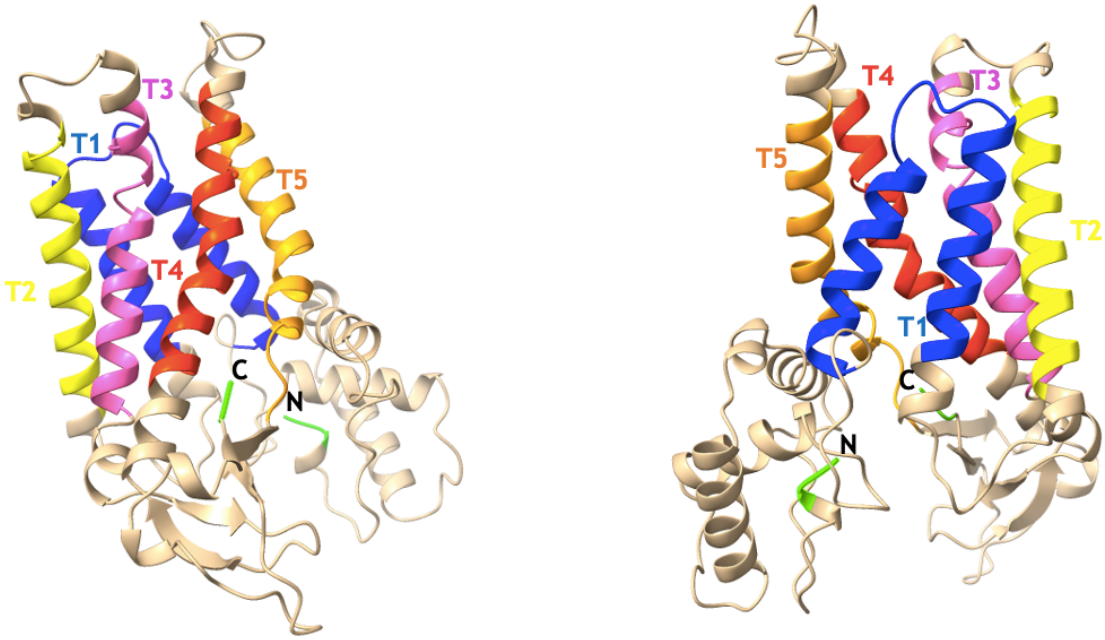

Fig. 6.6: AlphaFold-predicted structure of yeast FSF1, showing location of predicted TRs. *FSF1 predicted structure was obtained from AlphaFold and the location of predicted TRs mapped to the structure in UCSF ChimeraX. TR1 (T1) is coloured blue, TR2 (T2) coloured yellow, TR3 (T3) coloured pink, TR4 (T4) coloured red and TR5 (T5) coloured orange. The location of the N- and C-termini is labelled and coloured green. Two rotations of the structure are provided.*

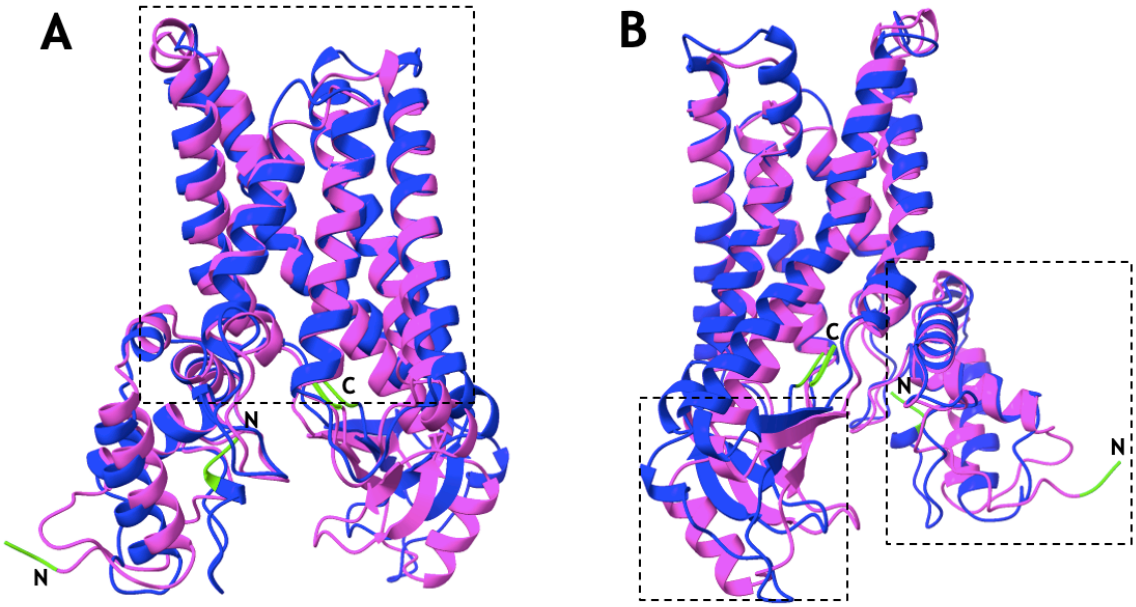

Fig. 6.7: Predicted structure of SFXN3 superimposed on that of FSF1. *Predicted structures were obtained from AlphaFold and superimposed using the Matchmaker function in UCSF ChimeraX. FSF1 structure is shown in blue whereas SFXN3 is shown in pink. N- and C-termini are labelled and coloured green. Two orientations are shown. (A) Orientation 1 of superimposed structures, showing helical bundle-like region within in dotted region. (B) Orientation 2 of superimposed structures, showing regions containing smaller helices and beta-strands.*

6.2.3 Import of FSF1 into WT yeast mitochondria

Following on from SFXN3 comparisons, study focused solely on FSF1. Localisation of FSF1 to mitochondria has been assumed, but not experimentally confirmed. Therefore, to determine if FSF1 could target the mitochondria, FSF1 was translated as a ^{35}S-radiolabelled precursor. Radiolabelled FSF1 was then imported into WT mitochondria via incubation with isolated mitochondria at 30°C for 10 minutes (**fig. 6.8**). As demonstrated in **fig. 6.8**, FSF1 was successfully imported into WT mitochondria. Import was reduced upon dissipation of the inner mitochondrial membrane potential ($\Delta\psi$-), which would suggest that the membrane potential is required for efficient import of FSF1. A lower molecular weight product can be visualised in the 3% lane of **fig. 6.8.** This may have been the result of alternative translation initiation, or perhaps protein degradation.

This band cannot be attributed to protease cleavage upon entry to the mitochondria as the band existed prior to import.

Following successful import of FSF1, import kinetics of the protein were investigated by repeating the import reaction at specified timepoints (**fig. 6.9**). As demonstrated in **fig. 6.9**, FSF1 was efficiently and quickly imported into mitochondria after only 5 minutes, in the presence of the membrane potential. The quantity of FSF1 imported did not increase by longer incubation (10 or 30 minutes) with mitochondria. Overall, import results demonstrate that FSF1 can be imported into yeast mitochondria and import is dependent on the membrane potential. However, it must be acknowledged that FSF1 import experiment should be repeated three times to allow for reliable quantification.

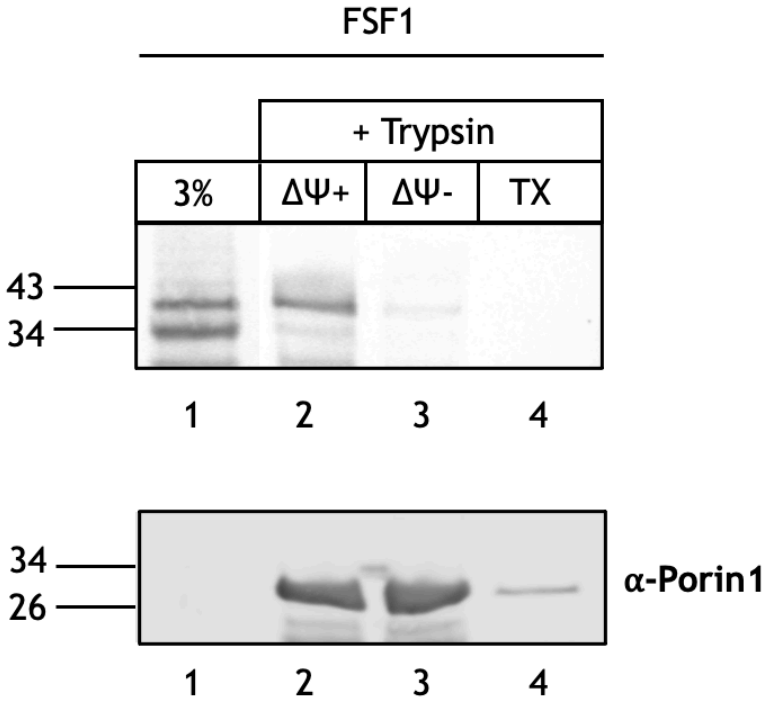

Fig. 6.8: Import of FSF1 into WT mitochondria. *^{35}S-radiolabelled FSF1 was imported into wild-type yeast mitochondria for 10 minutes, in the presence (lane 1) or absence (lane 2) of the IMM potential (Ψ+). After import, samples were treated with trypsin to remove any unimported material. Mitochondria were treated with triton-X as a negative control (lane 3). 3% represents 3% of the total radiolabelled FSF1 translated during the TNT reaction which was incubated with WT mitochondria for import (lane 4). Immunoblotting for levels of yeast Porin1 was performed to control for equal loading across lanes. The 3%*

sample was run to the lane immediately right of the TX lane but has been moved to the position shown to aid visualisation.

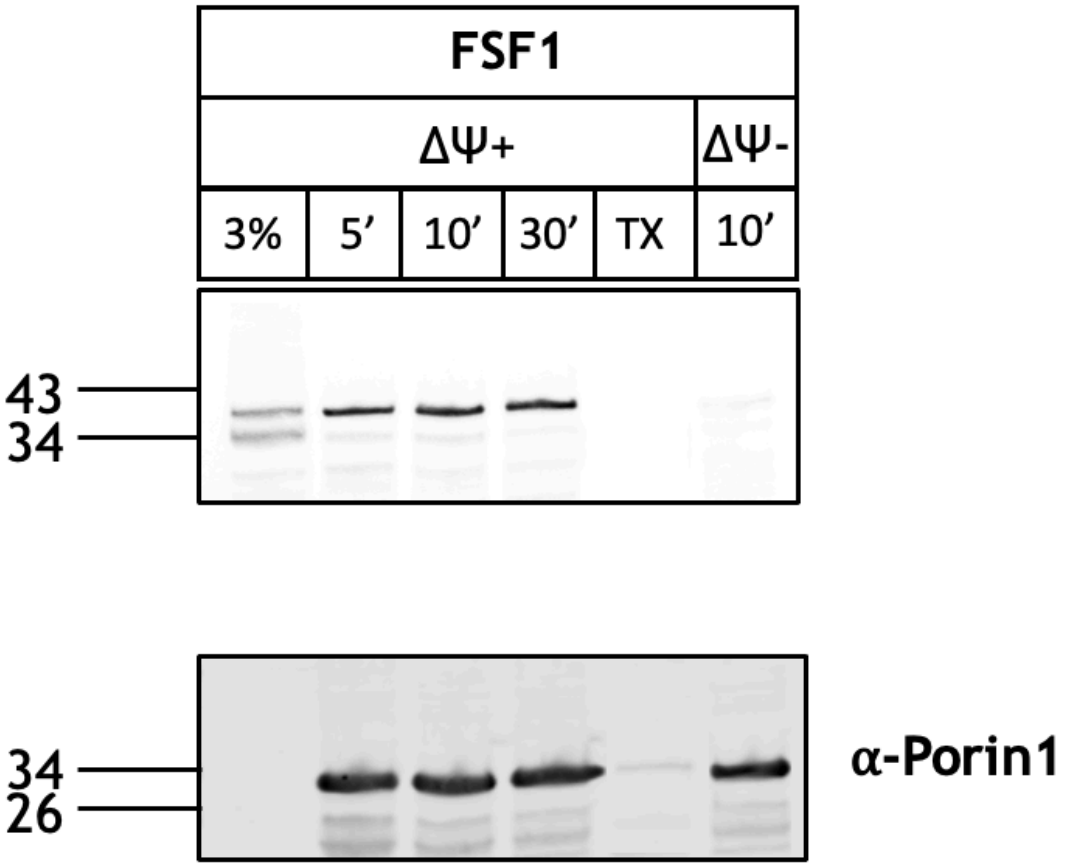

Fig. 6.9: Import kinetics of yeast FSF1 into wild-type yeast mitochondria. *Radiolabelled FSF1 was imported into wild-type yeast mitochondria for 5, 10 or 30 minutes in the presence of the IMM potential (ΔΨ+). Import was also carried out for 10 minutes following dissipation of the membrane potential (ΔΨ-). 3% corresponds to 3% of the total S^{35}-radiolabelled FSF1 which was incubated with mitochondria for import. Mitochondria were treated with Triton-X (TX) as a negative control. Immunoblotting for levels of yeast Porin1 was performed to confirm equal protein loading. The 10' (ΔΨ-) lane was run before the TX lane on the Tris-Tricine gel. The order has been swapped here to aid visualisation.*

6.2.4 Viability of ΔFSF1 yeast under fermentative and respiratory conditions

Following confirmation that FSF1 localises to mitochondria, investigation progressed by attempting to characterise FSF1 function in *S. cerevisiae*. Foremost, the decision was made to determine if FSF1 plays a role in respiration

as: (1) FSF1 is a mitochondrial protein and mitochondria are the site of the TCA cycle and ETC; (2) SFXN4 and SFXN2-KOs show mitochondrial respiration defects; and (3) SFXN4 loss in mitochondrial disease patients has been linked to decreased complex I activity and consequently, altered respiration (Hildick-Smith et al., 2013; Mon et al., 2019; Paul et al., 2019; Chen et al., 2022).

To assess the role of FSF1 in respiration, growth of FSF1 knockout (ΔFSF1) yeast (Horizon Discovery Yeast Knockout Collection) on YPLac, YPGal and YPD was assessed via spot test assay (**fig. 6.10**). Growth of yeast on YPLac provides cells with lactate as a carbon source. As lactate is non-fermentable, yeast cells grown on YPLac depend on mitochondrial respiration for ATP generation and thus, growth. In contrast, growth of yeast on YPD and YPGal provides glucose and galactose as carbon sources respectively. Both are fermentable, thus yeast grown on YPD and YPGal are less dependent on mitochondrial respiration for ATP generation. As demonstrated in **fig. 6.10A**, ΔFSF1 yeast showed no obvious growth defect relative to WT nor did they show differences in growth between respiratory and fermentative conditions. To determine if ΔFSF1 yeast were temperature-sensitive, growth on the same carbon sources was also tested at 37°C (non-permissive temperature) (**fig. 6.10B**). However, **fig. 6.10B** demonstrates that there was no clear difference in WT and ΔFSF1 yeast growth at 37°C. Overall, these results suggest that lack of FSF1 is not detrimental to cellular respiration.

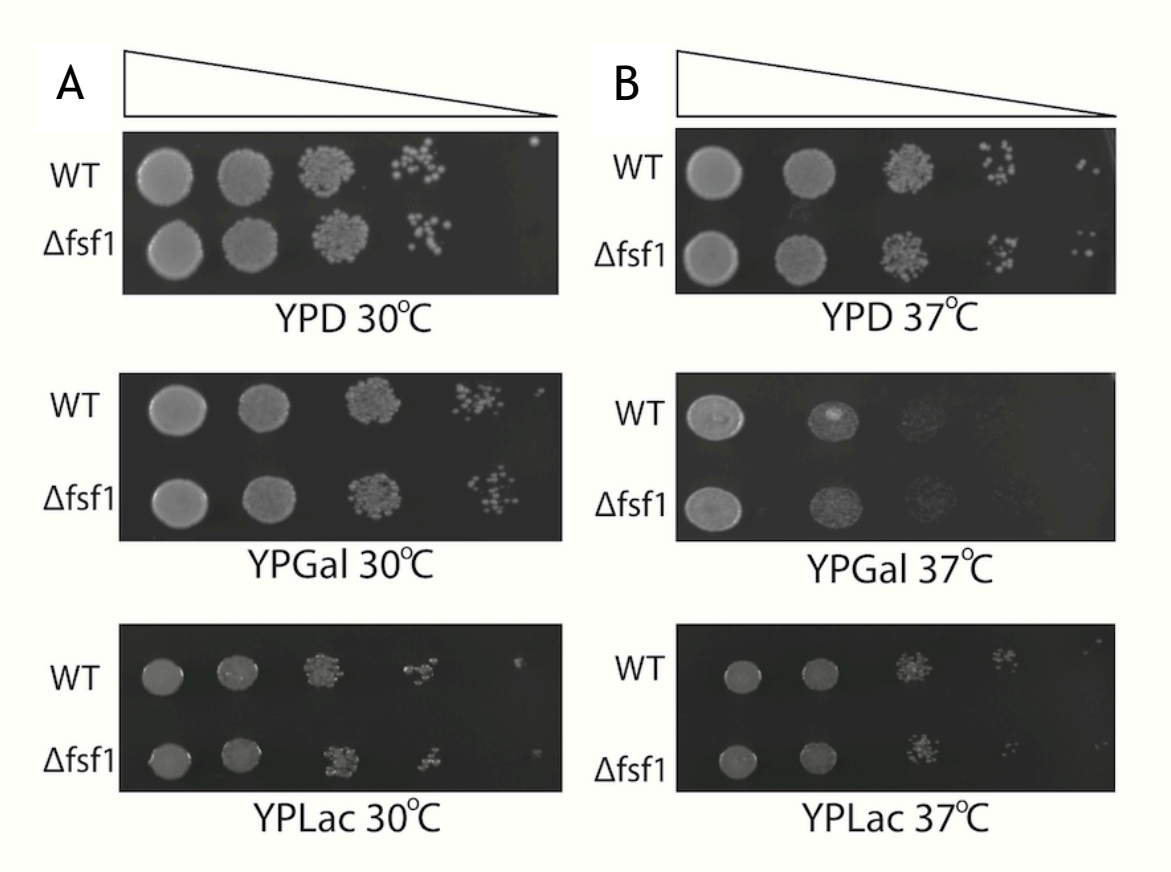

Fig. 6.10: Spot test assay of WT (BY4741) and ΔFSF1 yeast strains, grown under fermentative conditions (YPD and YPGal) or respiratory conditions (YPLac) at (A) 30°C (permissive temperature) or (B) 37°C (non-permissive temperature). *WT and ΔFSF1 yeast were grown in YPD overnight. Yeast cultures were serially diluted from 0.1 OD to 0.00001 OD and spotted on the indicated respiratory or fermentative media (from left to right). Plates were grown at permissive temperature (30°C) or non-permissive temperature (37°C).*

6.2.5 Steady state levels of mitochondrial proteins in ΔFSF1 yeast

Using the protocol detailed in section 3.2.3.1, ΔFSF1 mitochondria were isolated from the ΔFSF1 yeast strain. To gain an insight into FSF1 function from an unbiased perspective, steady state levels of mitochondrial proteins of wild-type and ΔFSF1 yeast strains were compared to identify any alterations upon loss of FSF1 (**fig. 6.11).** As shown in **fig. 6.11**, protein levels showed little difference across WT and ΔFSF1 yeast with the exception of aconitase, which showed a decrease in protein level in the ΔFSF1 strain relative to WT. Mitochondrial aconitase (ACO2) contains an Fe-S cluster ([3Fe-4S] or [4Fe-4S]). Overall, this

result may suggest that FSF1 plays a role in Fe-S cluster biosynthesis. Independent biological repeats must be performed to confirm this.

It should be noted that Tom40 and AAC levels appeared to be lower in the ΔFSF1 40 μg lane relative to that of the wild type. This was believed to be due to error when calculating amount of protein to be loaded to the second gel, resulting in less than 40 μg being loaded. Unfortunately, due to lack of time, the experiment could not be repeated to confirm or dispute this.

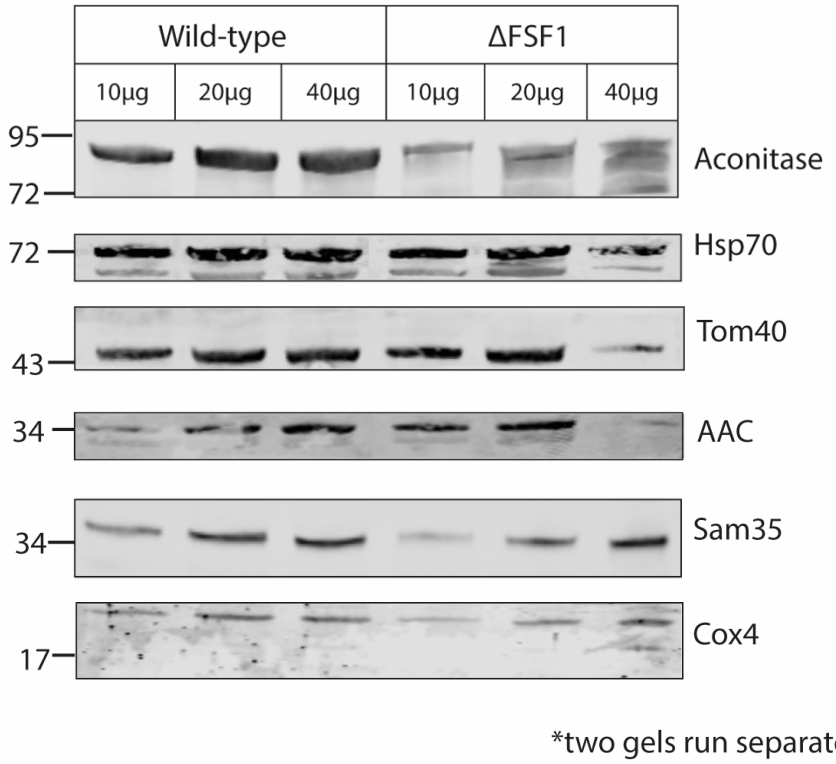

Fig. 6.11: Steady state levels of mitochondrial proteins in wild-type (BY4741) and ΔFSF1 mitochondria. *Mitochondria were isolated from wild-type (BY4741) and ΔFSF1 yeast strains. Mitochondrial protein (10 μg, 20 μg and 40 μg) was loaded into the wells of a 12% tris-tricine gel, and proteins separated via SDS-PAGE. Two gels were run separately, and proteins transferred to nitrocellulose membranes for immunoblotting. The first membrane was probed for mitochondrial aconitase, Sam35 and Cox4. The second membrane was probed for Hsp70, Tom40 and AAC*

6.2.6 FSF1 as a potential regulator of iron homeostasis

Fe-S cluster biogenesis is dependent on the delivery of iron to ISC machinery proteins in yeast, and a role for SFXNs in regulation of iron homeostasis has been proposed (Fleming et al., 2001; Ranatunga et al., 2016; Mon et al., 2019). Therefore, it was hypothesised that decreased levels of ACO2 seen in the absence of FSF1, as shown in **fig. 6.11,** may have resulted from impaired Fe-S cluster biogenesis caused by dysregulated iron homeostasis. Due to the TM structure of FSF1, it seems reasonable to suggest that the protein may be an iron transporter. To examine the role of FSF1 as an iron transporter, growth of wild-type and ΔFSF1 yeast was assessed on iron-limited YPLac media using a spot test assay (**fig. 6.12**). Iron content of YPLac was decreased via addition of iron chelator 1,10-phenanthroline to the media. Phenanthroline is a non-specific chelator and will also complex with ions such as zinc. Therefore, growth was also assessed on EGTA as a control, as EGTA chelates zinc and calcium ions, yet no evidence suggests iron chelation.

If FSF1 were an iron transporter, we would expect ΔFSF1 yeast to show poorer growth (auxotrophy) on iron-limited media as there would be a reduction in the uptake/export of iron into/out of the mitochondrial matrix which would disrupt maintenance of iron homeostasis. Specifically, we would expect that iron would accumulate in the mitochondria as a result of impaired export or there would be defective heme/Fe-S cluster biogenesis as a consequence of impaired iron import. As demonstrated in **fig. 6.12,** there was no difference in tolerance of wild-type and ΔFSF1 yeast strains to iron depletion. Therefore, results suggests that FSF1 is not an essential iron transporter in wild-type yeast strains.

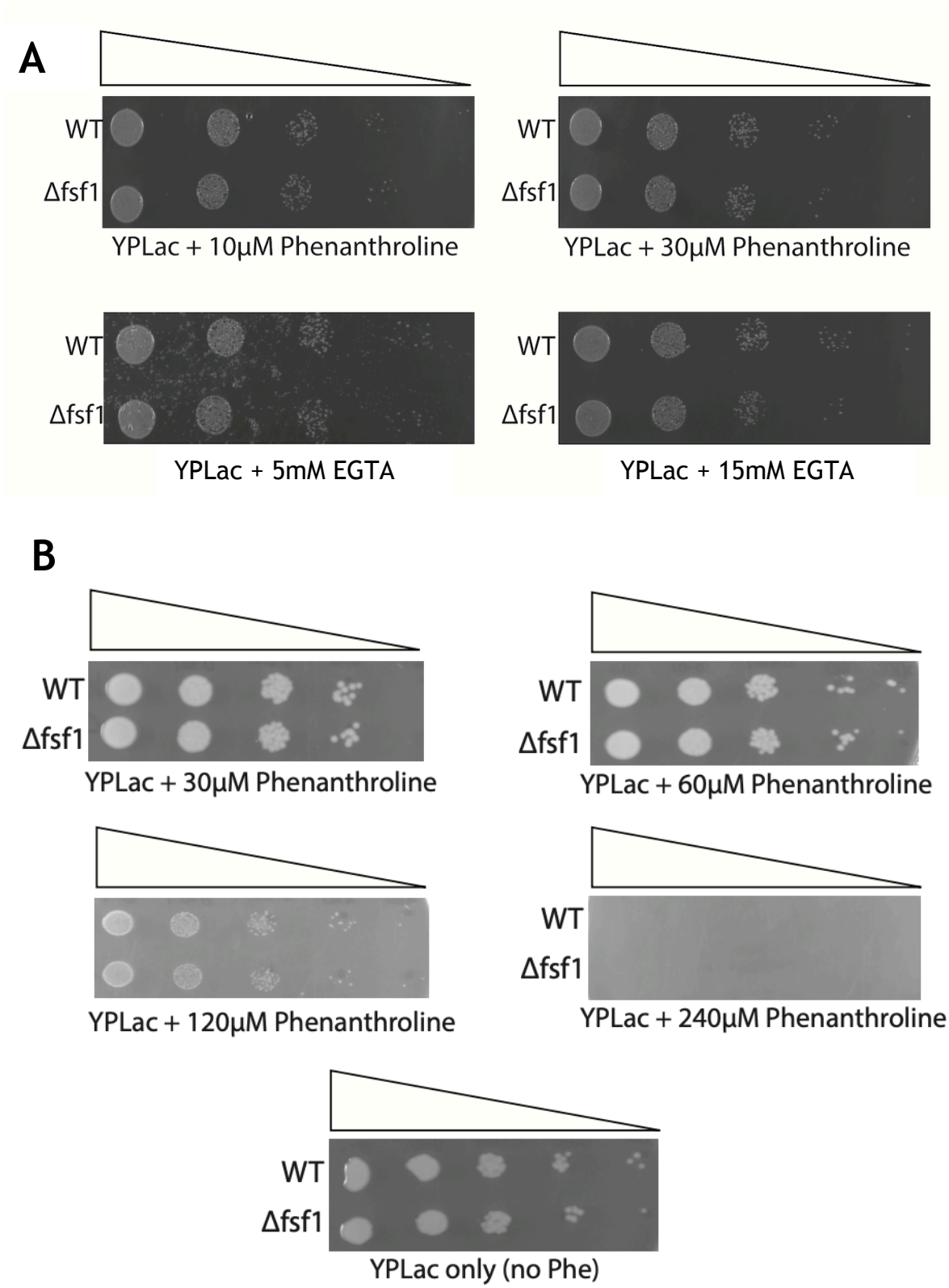

Fig. 6.12: Spot test assays to test tolerance of WT (BY4741) and ΔFSF1 yeast strains to iron-depletion by 1,10-phenanthroline. *(A) Serial dilutions of WT and ΔFSF1 yeast overnight cultures were grown on YPLac supplemented with iron chelator 1,10-phenanthroline (10 µM or 30 µM) or EGTA (5 mM or 15 mM). As 1,10-phenantholine is not a specific chelator of iron (also chelates*

magnesium and zinc ions), growth on chelator EGTA was tested as a control. (B) Spot test was repeated at various concentrations of 1,10-phenanthroline (30 μM, 60 μM, 120 μM or 240 μM). Spot tests were performed on YPLac only as a means of testing growth under iron-sufficient conditions.

6.3 Discussion

The role of SFXN3 as a transporter and in mitochondrial respiration has been debated. Therefore, this chapter aimed to elucidate the function of SFXN3 by generating an SFXN3-knockdown Hek293 cell line. However, due to difficulties faced, the aims of the study were altered to focus on uncovering function of yeast FSF1 as this could provide insight into a conserved SFXN family function.

6.3.1 Issues faced when creating an SFXN3-knockdown cell line

Exploration of SFXN3 function was halted due to issues with mammalian cell lysis (**fig 6.1 and 6.2**). Initially, TritonX-100 was the detergent of choice as it is widely used to solubilise membrane proteins. However, TritonX-100 lysis was consistently unable to release SFXN3 from the IMM (**fig. 6.2).** Gurtubay and colleagues (1980) demonstrated that membrane proteins could be 'selectively solubilised', meaning that throughout a range of detergent concentrations, certain membrane proteins were solubilised whereas others were not. Thus, perhaps in this study the detergent concentration used was not optimal for SFXN3 extraction. The decision was made to use RIPA buffer for cell lysis as said buffer contains harsh ionic detergents (SDS and sodium deoxycholate) which solubilise all membrane proteins. The advantage which TritonX-100 has over RIPA is that TritonX is non-denaturing so will not disrupt protein-protein interactions. However, this was not an issue for the present study as lysis was performed solely to check knockdown success, not for downstream applications. As **fig. 6.2** demonstrated, RIPA lysis permitted SFXN3 release. However, only low levels of SFXN3 protein expression were detected in WT Hek293 cells. This is likely as Hek293 cells show very low SFXN3 mRNA expression (Mon et al., 2019). Unfortunately, low expression made it very difficult to visualise any difference in SFXN3 levels across WT and KD cells. Only when chemiluminescent detection was used were SFXN3 bands clearly visible (**fig 6.3**). In retrospect, KD should

have been completed in a neuronal cell line as neurons show high SFXN3 expression levels (Rivell et al., 2019; Chen et al., 2022). As SFXN3 is essential for maintenance of synapses in mice and is a downstream target of α-synuclein in PD, SFXN3-KD in a neuronal cell line would allow further exploration of the role of SFXN3 in neurodegeneration (Amorim et al., 2017; Chen et al., 2020; Ledahawsky et al., 2022).

Nonetheless, SFXN3 levels do appear slightly reduced in SFXN3-KD Hek293 cells (**fig. 6.3**). As aforementioned, due to cell lysis issues, quantification of independent biological repeats was not performed. Thus, we cannot confirm success of KD at present. Further, as cell lysis took several attempts, Hek293 cells had to be maintained and cells divided far more times than desired. Thus, it is likely that SFXN3 levels only saw a slight reduction as SFXN3 shRNA was transiently expressed in Hek293 cells, and said expression decreased by the time cell lysis was successful. In hindsight, cell lysis should have been optimised prior to shRNA transfection to minimise time between transfection and lysis. Alternatively, SFXN3 shRNA could have been stably expressed in Hek293 cells via lentiviral transduction to permit persistent expression. Ideally, CRISPR-Cas9 would have been utilised to completely silence SFXN3 gene expression – eliminating any chance that residual SFXN3 protein could impact results. Additionally, it would have been beneficial to include further controls in the knockdown to identify where issues were arising. Additional negative controls could have included scramble shRNA or an empty vector control.

Failure to generate an SFXN3-KD line in sufficient time prevented any downstream experiments from going ahead, which would have allowed exploration of SFXN3 function. Using an SFXN3-KD/KO line, future study could determine if SFXN3 plays a role in respiration via oxygen consumption assays or measurement of respiratory complex activity as done previously (Jackson et al., 2022). As certain SFXNs have redundant functions, it would also be beneficial to create a cell line lacking several SFXNs as this would uncover functions hidden by compensation of other isoforms (Yoshikumi et al., 2005; Kory et al., 2018).

6.3.2 Human SFXN3 and yeast FSF1 share similar structural and sequence elements

There is very limited research surrounding *S. cerevisiae* FSF1. Similar to SFXN3, FSF1 is a TM protein, harbouring 3-5 TM regions (**fig 6.4**). It appears most likely that FSF1 has 5 TMs, as the majority of prediction programs used in this study and hydropathy analysis performed previously predict 5 TMs (Miotto et al., 2007; Li et al., 2010). Nonetheless, this is speculative without experimental evidence. Interestingly, the first TR of FSF1 identified by all four prediction programs spans residues 90-128. This overlaps with TOPCONS-predicted TM1 of SFXN3 (97-117). Several residues within this region are highly conserved between SFXN3 and FSF1, which may once again suggest TOPCONS predictions were correct. This should be further investigated as described prior.

Showing additional likeness to SFXN3, FSF1 has a large N-terminus and short C-terminus harbouring conserved motifs (**fig 6.4**). Predicted structures of SFXN3 and FSF1 show various similarities such as: their largely alpha-helical nature and unusual beta-strand region (**fig 6.5**) and the arrangement of TRs in a helical bundle-like structure (**fig 6.6, 6.7**). This is consistent with the prior finding that FSF1 and SFXN5 share highly similar secondary structures (Miotto et al., 2007).

6.3.3 FSF1 contains mitochondrial targeting information and requires the membrane potential for import

A study by Miotto and colleagues (2007) suggested that FSF1 targets the mitochondria solely based on its similarity to mammalian SFXNs. Thus, the present study provides the first experimental evidence that FSF1 can target the mitochondria (**fig 6.8**). As FSF1 lacks a mitochondrial pre-sequence (Fleming et al., 2001; Miotto et al., 2007), it seems likely that FSF1 must harbour internal targeting information. Additionally, FSF1 was quickly and efficiently imported into mitochondria, in a membrane potential-dependent manner (**fig 6.9**). Whilst this bears a likeness to SFXN3 import, shown in **fig 5.7**, the present results are unable to confirm or dispute if FSF1 too follows the carrier import pathway and localises to the IMM. To investigate this, FSF1 should be imported into mutant yeast mitochondria lacking components of the carrier import pathway as done

previously (Ledahawsky et al., 2022). IMM localisation could be assessed via mitoplasting and sodium carbonate extraction.

6.3.4 FSF1 is not vital for mitochondrial respiration

Loss of FSF1 did not impair fermentation or mitochondrial respiration of *S. cerevisiae* (**fig 6.10**). The latter demonstrates that FSF1 is not essential for mitochondrial bioenergetics. Similarly, lack of SFXN3 in mice synaptosomes did not alter mitochondrial respiration (Amorim et al., 2017). This highlights a key similarity in function of FSF1 and SFXN3. However, SFXN3 is the sole SFXN which has not been linked to respiration (with the exception of SFXN5 due to lack of data). SFXN1 KO decreased complex III activity (Acoba et al., 2021). SFXN2 KO led to a decline in complex II-IV activity (Mon et al., 2019; Chen et al., 2022). SFXN4 KO in K562 cells reduced levels of proteins of complexes I-IV (Paul et al., 2019). Additionally, SFXN4 complete/partial loss-of-function in mitochondrial disease patients is responsible for complex I deficiency – a result which is reproduced in SFXN4-KO in Hek293 cells and SFXN4-KD zebrafish (Hildick-Smith et al., 2013; Jackson et al., 2022). As a putative complex I assembly factor, SFXN4 primarily alters respiration via complex I (Jackson et al., 2022). Perhaps altered respiration was not seen for ΔFSF1 yeast due to the lack of complex I in the yeast ETC. Nonetheless, this cannot explain the difference in impact of FSF1 loss vs. SFXN1/SFXN2 loss on respiration, as complex I activity is unchanged in the absence of SFXN1 and 2 (Mon et al., 2019; Acoba et al., 2021). As a potential explanation, perhaps the role of SFXN1/2 in respiration is distinct to mammals. To test this, respiratory complex activity and oxygen consumption of ΔFSF1 yeast should be measured.

6.3.5 Loss of FSF1 results in decreased levels of mitochondrial aconitase

Results of steady state level experiments shown in **fig 6.11** demonstrated that ACO2 levels were decreased in FSF1 KO yeast mitochondria relative to the wild-type counterpart. ACO2 is an isomerase which converts citrate to isocitrate in the TCA cycle. Previous unpublished data identified a decrease in the metabolism of citrate upon loss of FSF1 (Siciarz et al., unpublished). It was suggested that citrate metabolism declined as FSF1 loss altered ACO2 activity,

which would reduce conversion of citrate to isocitrate. Supporting this, Hek293 SFXN4 KO reduced levels and activity of ACO2 (Paul et al., 2019).

ACO2 requires an Fe-S cluster for functionality and is degraded upon cluster loss (Paul et al., 2017). Therefore, perhaps FSF1 is required for global Fe-S biogenesis. Study by Paul and colleagues (2019) supports this hypothesis by identifying a decrease in levels of various additional mitochondrial and cytosolic Fe-S cluster containing proteins upon Hek293 SFXN4 KO. In contrast, Hek293 SFXN4 knockout performed by a different group did not alter levels of Fe-S cluster proteins, nor did it affect levels of Fe-S cluster-containing respiratory complexes II and III (Jackson et al., 2022). Similarly, SFXN2 loss does not alter levels of Fe-S cluster containing complex I (Mon et al., 2019). Interestingly, complexes II and III of *S. cerevisiae* contain Fe-S clusters which are essential for their activity, yet mitochondrial respiration did not appear to be altered by FSF1 loss in the present study (**fig 6.10**). Therefore, the role of SFXNs in Fe-S cluster biogenesis remains widely disputed. Further study must repeat the steady state experiment described to assess its reproducibility, and could then aim to determine if the effect of FSF1 loss is limited to ACO2 or whether other Fe-S cluster proteins are affected.

As an additional avenue for further study, it may be interesting to pursue the idea that SFXNs may be cysteine transporters. Cysteine is required for Fe-S cluster biogenesis (Paul et al., 2017). An *in vitro* competition assay demonstrated that cysteine competed with serine for transport by SFXN1 whereas SFXN4 was unable to transport cysteine (Kory et al., 2018; Jackson et al., 2022). Therefore, perhaps functioning in Fe-S cluster biogenesis is distinct to only certain SFXNs, and this function is only somewhat conserved in yeast as FSF1 is their only SFXN and it likely harbours a broader transport capacity than each individual mammalian SFXN which may have evolved to ensure more specialised transport functions.

6.3.6 FSF1 is not essential for iron transport *in vivo*

The present study does not suggest a role for FSF1 in iron transport (**fig 6.12**). Nonetheless, this finding was unexpected, as various studies have linked SFXNs and iron. For instance, SFXN1 KD enhanced mitochondrial iron levels (Tifoun et al., 2021); SFXN2 KO increased total iron content of Hek293 cells whereas knockdown resulted in accumulation of iron in the mitochondria (Mon et al., 2019; Chen et al., 2022) and SFXN4 KO stimulated mitochondrial iron accumulation (Paul et al., 2019). As a potential explanation, perhaps a role in iron transport is distinct to only mammalian SFXNs and lost in yeast. This should be tested by assessing mitochondrial ferrous iron levels of the FSF1 KO strain as done previously (Mon et al., 2019).

As an alternative explanation for the results shown in **fig 6.12**, IMM iron transporters have already been defined for mammals (mitoferrin-1, mitoferrin-2) and yeast (Mrs3, Mrs4) (Cunningham and Rutter, 2020). Thus, it is perhaps improbable that SFXNs would also transport iron. Rather, perhaps SFXNs influence iron homeostasis by interacting with iron transporters/IMM proteins to influence their function, as has recently been shown for mitochondrial carrier MITOSUR and cation channel MITOK (Chen et al., 2009; Paggio et al., 2019). Nonetheless, it should be acknowledged that SFXN2 is an OMM protein (Mon et al., 2019). It has been suggested that iron crosses the OM via porins, but this has not been confirmed experimentally (Lane et al., 2015). Therefore, we cannot rule out the possibility that SFXN2 may transport iron across the OMM before delivery to the IMS and subsequently mitoferrins.

Moreover, although SFXNs do not transport pyridoxine, a precursor of ALAS2 co-factor pyridoxal phosphate, it may be possible that SFXNs transport a different substrate required for incorporation of iron into heme as various studies have linked SFXNs and heme biosynthesis (Paul et al., 2017; Kory et al., 2018; Bao et al., 2021). For instance, SFXN2 KO led to decreased heme content in mammalian cell lines (Mon et al., 2019; Chen et al., 2022). Substrate specificity of SFXN3 could be assessed via isothermal titration calorimetry, and activity of the transporter analysed using electrophysiology assays as done previously

(Neginskaya, Pavlov and Sheu, 2021). Interestingly, Tifoun and colleagues (2021) recently identified heme binding motifs (HBMs) in SFXN1 which may suggest that SFXN1 is actually able to bind heme itself. Therefore, studying the relationship of SFXNs and heme biosynthesis should be highly valuable in providing insight into SFXN function. As a potential means of assessing substrate specificity of SFXN3, future study could use isothermal titration calorimetry.

Further, it is possible that the ΔFSF1 strain used throughout this chapter could have developed compensatory mechanisms upon loss of the FSF1 gene. To assess this in future, we could overexpress a library of various genes to assess if any are able to complement the null mutant ΔFSF1.

6.3.7 Overall conclusions

To conclude, human SFXN3 and yeast FSF1 show various similarities in their structure, sequence, and mitochondrial targeting. Nonetheless, the function of these proteins remains to be fully uncovered. The present report provides evidence against some functions for FSF1: essentiality for mitochondrial respiration and iron homeostasis. However, additional repeats are needed. Additionally, the present study established a potential link between FSF1 and ACO2 levels, emphasising the need for further study focused on uncovering the role of SFXNs in Fe-S cluster biogenesis.

Throughout the study it became increasingly evident that individual SFXNs, despite sharing some functions, probably exhibit distinct functions too. Individual functions cannot be investigated using FSF1. Therefore, value in creating mammalian KD/KO strains for elucidating function is evident and should be completed in future. Similarly, generating a SFXN3 KD/KO mouse model would be more relevant to medical research than the use of cell lines, as it would allow us to study the effects of SFXN3 loss on a whole organism which possesses a very similar genome to that of humans. Understanding SFXN3 function is key to understanding its potential as a therapeutic target. Therapeutic targeting of SLC25 family members has been successful in the past

(Cunningham and Rutter, 2020). Thus, it can be envisaged that SFXN targeting could also be a viable and interesting pharmaceutical route.

Appendix

Appendix table 1: Primers used in unsuccessful cloning attempts and description of their use.

Primer Name	Primer Sequence (5' – 3' orientation)	Use
FRW_SFXN3_SAL1	GCGTCGACATGGAAAGCAAAATGGGT	Forward primer for amplification of SFXN3 truncations
REV_SFXN3_NT_XBA1	GCTCTAGATCACATCATCATGATGGGAGTGTC	Reverse primer for amplification of SFXN3 N-terminal only
REV_SFXN3_T1_XBA1	GCTCTAGATCACATCATCATCATGGTGAGGGATTT	Reverse primer for amplification of SFXN3 N-terminal to TR1
REV_SFXN3_T2_XBA1	GCTCTAGATCACATCATCATCATCTCTCTCTGCCTCAT	Reverse primer for amplification of SFXN3 N-terminal to TR2
REV_SFXN3_T3_XBA1	GCTCTAGATCACATCATCATCATCTTCTCCAGAGT	Reverse primer for amplification of SFXN3 N-terminal to TR3
REV_SFXN3_T4_XBA1	GCTCTAGATCACATCATCATCATGGAGCTCTTCTG	Reverse primer for amplification of SFXN3 N-terminal to TR4
FRW_SFXN3_BAMH1	GCGGATCCATGGAAAGCAAAATGGGTGAATTGCC	Forward primer for amplification of SFXN3 truncations, alternative restriction site
REV_SFXN3_NT_ECOR1	GCGAATTCTCACATCATCATCATGCCTCACAGTGATGGGAGTGTC	Reverse primer for amplification of

		SFXN3 N-terminal only, alternative restriction site
REV_SFXN3_T1_ECOR1	GCGAATTCTCACATCATCATCATCAAGGGGGGCAAGTGCTTGGTGAGG	Reverse primer for amplification of SFXN3 N-terminal to TR1, alternative restriction site
REV_SFXN3_T2_ECOR1	GCGAATTCTCACATCATCATCATGCCCACCTGCAGCTCTCTC	Reverse primer for amplification of SFXN3 N-terminal to TR2, alternative restriction site
REV_SFXN3_T3_ECOR1	GCGAATTCTCACATCATCATCATCAGGAAGTCTTTCTTCTCCAGAGTGTCC	Reverse primer for amplification of SFXN3 N-terminal to TR3, alternative restriction site
REV_SFXN3_T4_ECOR1	GCGAATTCTCACATCATCATCATGTTGCTTATGTGTATGGAGCTCTTCTG	Reverse primer for amplification of SFXN3 N-terminal to TR4, alternative restriction site
FRW_PSP64_ECOR1	CAGTGAATTCGTAATCATGTCATAGCTGTTTCC	Forward primer for amplification of pSP64 vector
REV_PSP64_BAMH1	CAGTGGATCCTCTAGAGTCGACCTGC	Reverse primer for amplification of pSP64 vector

A

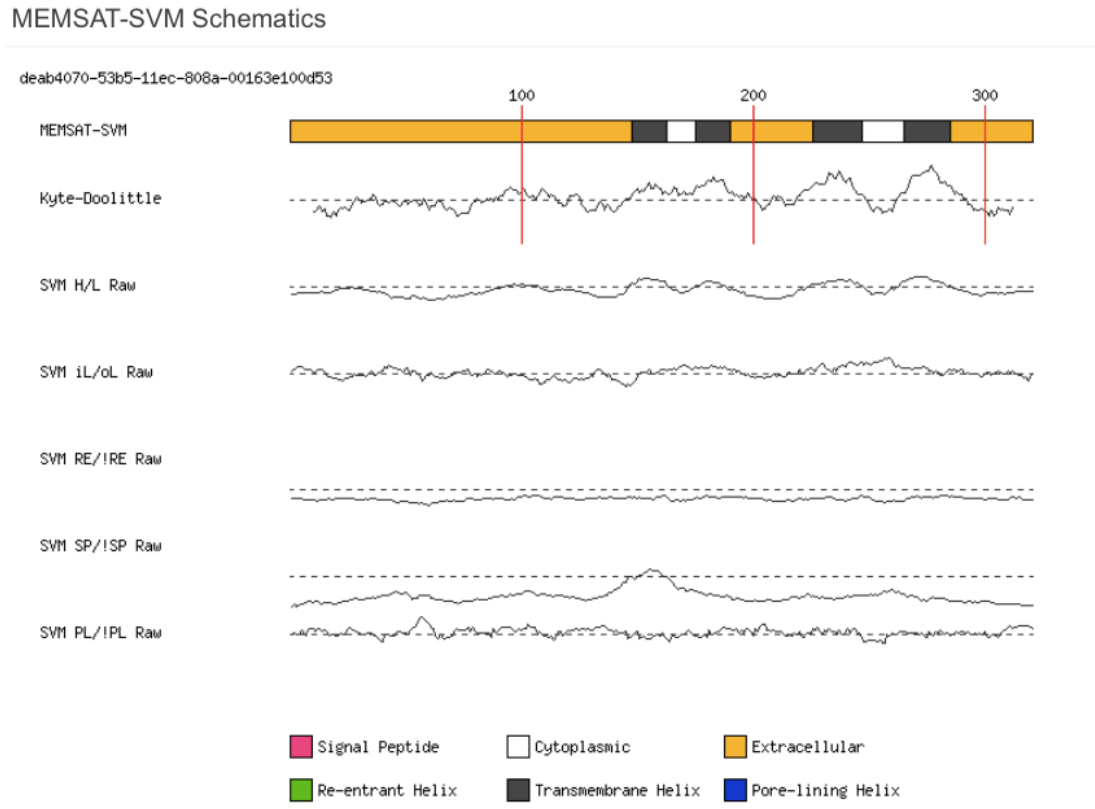
MEMSAT-SVM Schematics
deab4070-53b5-11ec-808a-00163e100d53
100
200
300
MEMSAT-SVM
Kyte-Doolittle
SVM H/L Raw
SVM iL/oL Raw
SVM RE/!RE Raw
SVM SP/!SP Raw
SVM PL/!PL Raw
Signal Peptide
Cytoplasmic
Extracellular
Re-entrant Helix
Transmembrane Helix
Pore-lining Helix

B

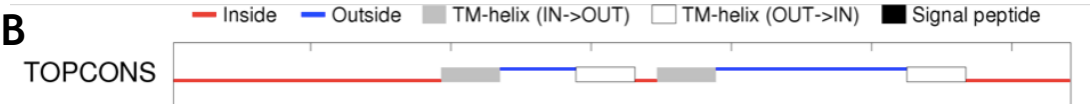
Inside
Outside
TM-helix (IN->OUT)
TM-helix (OUT->IN)
Signal peptide
TOPCONS

C

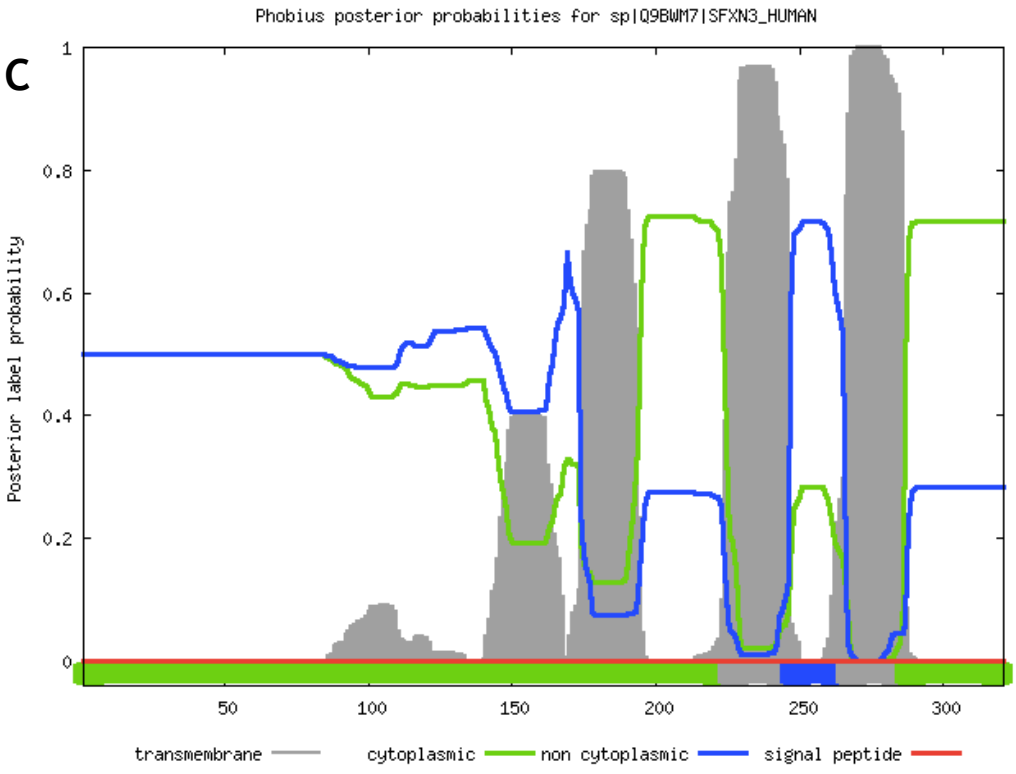
Phobius posterior probabilities for sp|Q9BWM7|SFXN3_HUMAN
Posterior label probability
1
0.8
0.6
0.4
0.2
0
50
100
150
200
250
300
transmembrane
cytoplasmic
non cytoplasmic
signal peptide

D

```
Length:  321
N-terminus: OUT
Number of transmembrane helices: 4
Transmembrane helices: 146-163 178-195 226-247 268-286

Total entropy of the model:  17.0149
Entropy of the best path:  17.0167

The best path:

     seq  MGELPLDINI QEPRWDQSTF LGRARHFFTV TDPRNLLLSG AQLEASRNIV    50
     pred OOOOOOOOOO OOOOOOOOOO OOOOOOOOOO OOOOOOOOOO OOOOOOOOOO

     seq  QNYRAGVVTP GITEDQLWRA KYVYDSAFHP DTGEKVVLIG RMSAQVPMNM   100
     pred OOOOOOOOOO OOOOOOOOOO OOOOOOOOOO OOOOOOOOOO OOOOOOOOOO

     seq  TITGCMLTFY RKTPTVVFWQ WVNQSFNAIV NYSNRSGDTP ITVRQLGTAY   150
     pred OOOOOOOOOO OOOOOOOOOO OOOOOOOOOO oooooooooo oooooHHHHH

     seq  VSATTGAVAT ALGLKSLTKH LPPLVGRFVP FAAVAAANCI NIPLMRQREL   200
     pred HHHHHHHHHH HHHiiiiiii iiiiiiiHHH HHHHHHHHHH HHHHHooooo

     seq  QVGIPVADEA GQRLGYSVTA AKQGIFQVVI SRICMAIPAM AIPPLIMDTL   250
     pred oooooooooo oooooooooo oooooHHHHH HHHHHHHHHH HHHHHHHiii

     seq  EKKDFLKRRP WLGAPLQVGL VGFCLVFATP LCCALFPQKS SIHISNLEPE   300
     pred iiiiiiiiii iiiiiiiHHH HHHHHHHHHH HHHHHHoooo oooooooooo

     seq  LRAQIHEQNP SVEVVYYNKG L  321
     pred oOOOOOOOOO OOOOOOOOOO O
```

Appendix Fig. 1: Raw data generated by TM and topology prediction programs for SFXN3. *Topology and TM prediction data generated by the following programs is shown: (A) MEMSAT-SVM (B) TOPCONS (C) PHOBIUS (D) HMMTOP 2.0. Symbols beneath the SFXN3 sequence and alongside 'pred' can be defined as follows: 'O' - sequence regions predicted to reside in the IMS (or outside). 'H' - predicted transmembrane helices. 'i' - sequence regions predicted to reside in the matrix (or inside).*

Appendix Table 2: Precise location of predicted TMs within the protein sequence of SFXN3. *Four TM prediction tools were used to predict the location of TMs within the sequence of SFXN3 (HMMTOP 2.0, MEMSAT-SVM, PHOBIUS, TOPCONS). For each tool, the amino acid residues which each TM was predicted to span is detailed in table 1.*

TM Prediction Tool	**Predicted TM1** (aa residues spanned)	**Predicted TM2** (aa residues spanned)	**Predicted TM3** (aa residues spanned)	**Predicted TM4** (aa residues spanned)
HMMTOP 2.0	146-163	178-195	226-247	268-286

MEMSAT-SVM	149-164	176-191	227-248	266-286
PHOBIUS	147-164	174-194	225-246	266-287
TOPCONS	97-117	145-165	174-194	263-283

Appendix table 3: Sequences of SFXN3 predicted TMs compiled to generate four transmembrane regions (TR). *Table 2 shows residues numbers for regions labelled as L2-5 in results fig. 4.1. The regions shown were considered as TM1-4 for the sequence and structure analysis detailed in chapter 4.*

Predicted TR1 (residues spanned)	**Predicted TR2 (residues spanned)**	**Predicted TR3 (residues spanned)**	**Predicted TR4 (residues spanned)**
145-165	174-195	225-248	263-283

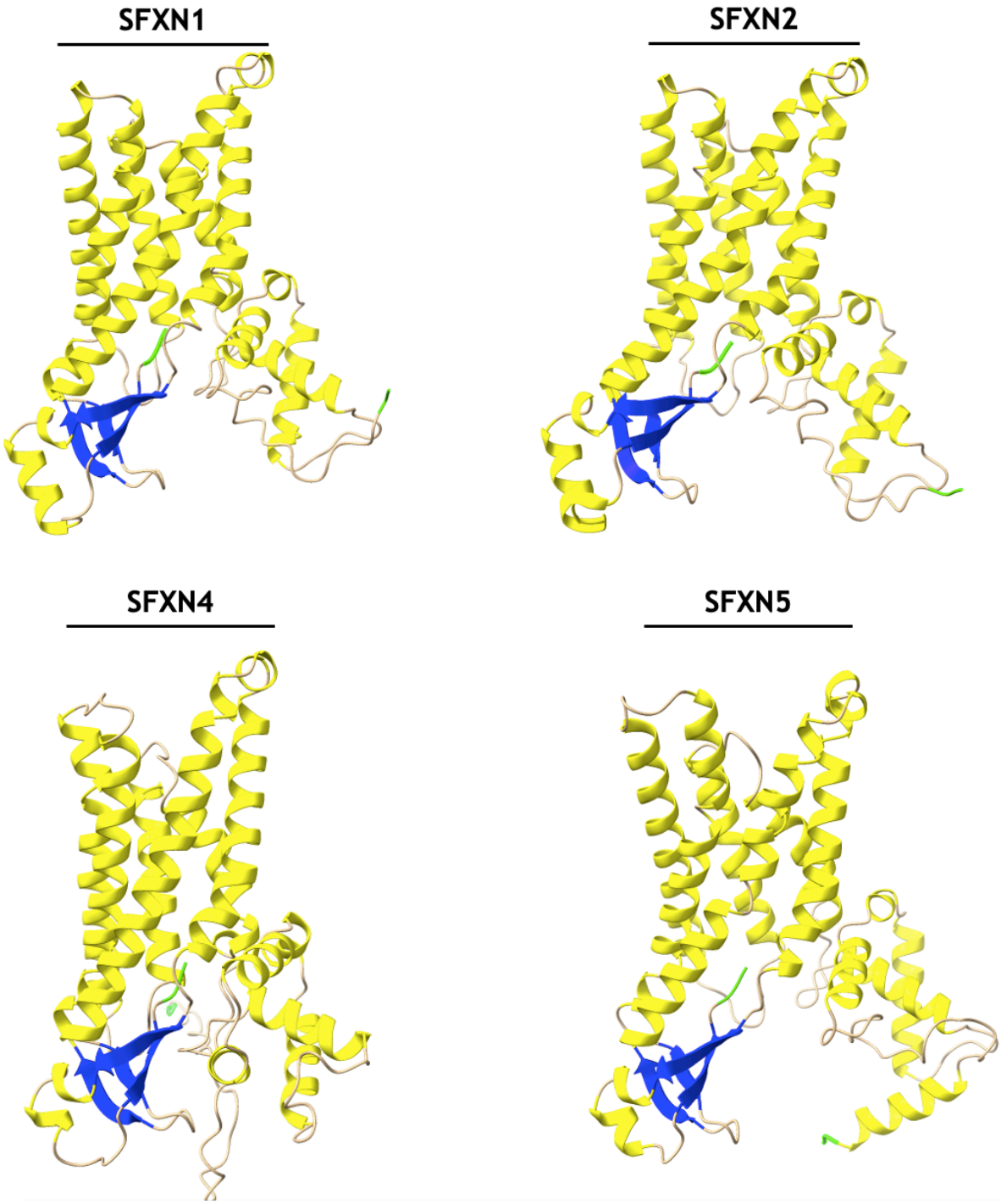

Appendix fig. 2: Predicted structure of SFXN family members. *The predicted 3D structure of SFXN1, SFXN2, SFXN4 and SFXN5 was obtained from AlphaFold. Structures were edited in UCSF ChimeraX to highlight helices (yellow) and beta-strands (blue). N- and C-termini are coloured green.*

Appendix Table 4: Sequences and charges of N- and C-termini extensions and IMS- or matrix-localised loops of SFXN3, according to prediction tools.
Prediction tools used to predict the location of TMs and topology of SFXN3 are shown in the first column. The sequences of the N- and C-termini, loop 1, loop 2 and loop 3 (as determined by prediction tools) are provided along with the corresponding amino acid charge of each sequence.

Prediction Tool	N-termini sequence	Overall amino acid charge
HMMTOP 2.0	MGELPLDINIQEPRWDQSTFLGRARHFFTVTDPRNLLL SGAQLEASRNIVQNYRAGVVTPGITEDQLWRAKYVYDS AFHPDTGEKVVLIGRMSAQVPMNMTITGCMLTFYRKTP TVVFWQWVNQSFNAIVNYSNRSGDTPITVRQ	+4
MEMSAT-SVM	MGELPLDINIQEPRWDQSTFLGRARHFFTVTDPRNLLL SGAQLEASRNIVQNYRAGVVTPGITEDQLWRAKYVYDS AFHPDTGEKVVLIGRMSAQVPMNMTITGCMLTFYRKTP TVVFWQWVNQSFNAIVNYSNRSGDTPITVRQLGT	+4
PHOBIUS	MGELPLDINIQEPRWDQSTFLGRARHFFTVTDPRNLLL SGAQLEASRNIVQNYRAGVVTPGITEDQLWRAKYVYDS AFHPDTGEKVVLIGRMSAQVPMNMTITGCMLTFYRKTP TVVFWQWVNQSFNAIVNYSNRSGDTPITVRQL	+4
TOPCONS	MGELPLDINIQEPRWDQSTFLGRARHFFTVTDPRNLLL SGAQLEASRNIVQNYRAGVVTPGITEDQLWRAKYVYDS AFHPDTGEKVVLIGRMSAQV	+1

Prediction Tool	Loop 1 sequence	Overall amino acid charge	Loop 2 sequence	Overall amino acid charge
HMMTOP 2.0	LKSLTKHLPPLVGR	+4	RQRELQVGIPVADEA GQRLGYSVTAAKQGI	+1
MEMSAT-SVM	KSLTKHLPPLV	+3	LMRQRELQVGIPVAD EAGQRLGYSVTAAKQ GIF	+1
PHOBIUS	KSLTKHLPP	+3	MRQRELQVGIPVADE AGQRLGYSVTAAKQG	+1
TOPCONS	FWQWVNQSFNAIVNYS NRSGDTPITVR	+1	SLTKHLPP	+2

Prediction Tool	Loop 3 sequence	Overall amino acid charge	C-termini sequence	Overall amino

				acid charge
HMMTOP 2.0	DTLEKKDFLKRRPWL GAPLQ	+2	PQKSSIHISNLEPE LRAQIHEQNPSVEV VYYNKGL	+1
MEMSAT-SVM	TLEKKDFLKRRPWLG AP	+3	PQKSSIHISNLEPE LRAQIHEQNPSVEV VYYNKGL	+1
PHOBIUS	MDTLEKKDFLKRRPW LGAP	+2	QKSSIHISNLEPEL RAQIHEQNPSVEVV YYNKGL	+1
TOPCONS	MRQRELQVGIPVADE AGQRLGYSVTAAKQG IFQVVISRICMAIPA MAIPPLIMDTLEKKD FLKRRPWL	+4	ALFPQKSSIHISNL EPELRAQIHEQNPS VEVVYYNKGL	+1

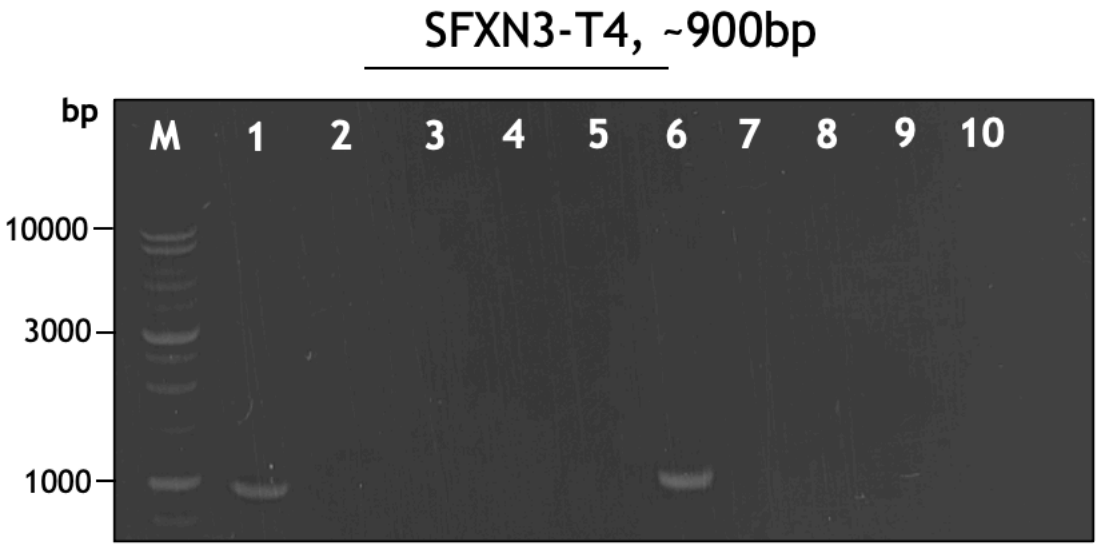

Appendix fig. 3: Agarose gel electrophoresis of SFXN3-T4 truncation, amplified through colony PCR. *DNA ligase was used to ligate SFXN3-T4 and pSP64. Ligated product was transformed into competent E. coli cells and grown on LB agar plates overnight at 37℃. To verify that SFXN3-T4-pSP64 was expressed by the bacteria, ten colonies were selected from the plates for use in colony PCR reactions. PCR products were separated via agarose gel electrophoresis. 1kB DNA Ladder (Promega) was run in lane 'M'. Selected bp*

markers along the ladder are labelled. Lanes 1-10 represent products from 10 individual PCR reactions, one for each colony selected.

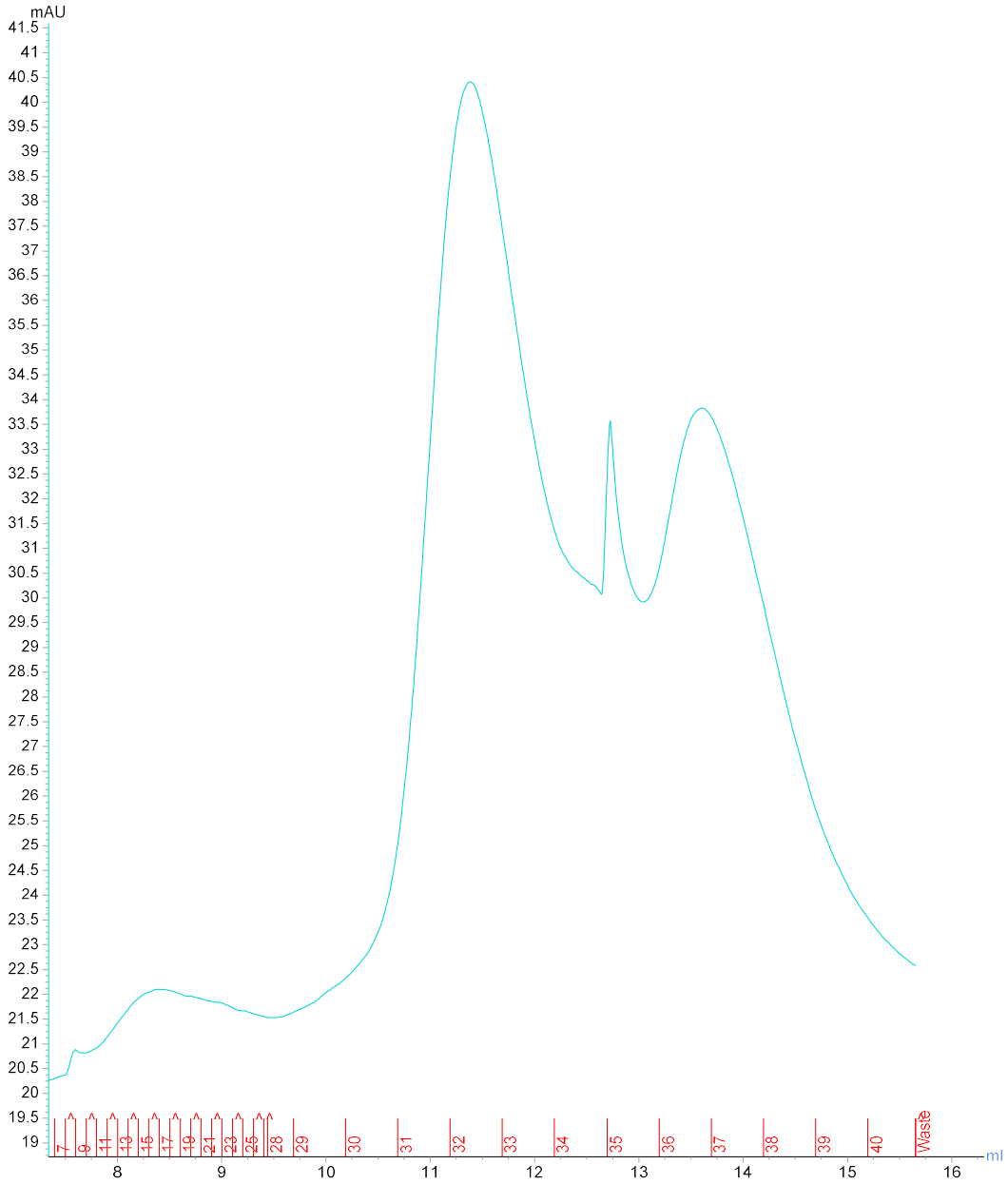

Appendix fig. 4 : FPLC elution trace for purified Tim9/10 complex. Purified Tim9 was incubated with purified Tim10 for 2 hours at 4°C. Purity of Tim9/10 was assessed via FPLC. Fractions 31-34 (mL) represent Tim9/10 complex and were pooled together for downstream applications. FPLC was conducted in collaboration with Tokatlidis lab technician, Erik Lacko.

1 MGELPLDINIQEP	27 HPDTGEKVVLIGR	53 AVATALGLKSLTK	79 MAIPAMAIPPLIM
2 LPLDINIQEPRWD	28 TGEKVVLIGRMSA	54 TALGLKSLTKHLP	80 PAMAIPPLIMDTL
3 DINIQEPRWDQST	29 KVVLIGRMSAQVP	55 GLKSLTKHLPPLV	81 AIPPLIMDTLEKK
4 IQEPRWDQSTFLG	30 LIGRMSAQVPMNM	56 SLTKHLPPLVGRF	82 PLIMDTLEKKDFL
5 PRWDQSTFLGRAR	31 RMSAQVPMNMTIT	57 KHLPPLVGRFVPF	83 MDTLEKKDFLKRR
6 DQSTFLGRARHFF	32 AQVPMNMTITGCM	58 PPLVGRFVPFAAV	84 LEKKDFLKRRPWL
7 TFLGRARHFFTVT	33 PMNMTITGCMLTF	59 VGRFVPFAAVAAA	85 KDFLKRRPWLGAP
8 GRARHFFTVTDPR	34 MTITGCMLTFYRK	60 FVPFAAVAAANCI	86 LKRRPWLGAPLQV
9 RHFFTVTDPRNLL	35 TGCMLTFYRKTPT	61 FAAVAAANCINIP	87 RPWLGAPLQVGLV
10 FTVTDPRNLLLSG	36 MLTFYRKTPTVVF	62 VAAANCINIPLMR	88 LGAPLQVGLVGFC
11 TDPRNLLLSGAQL	37 FYRKTPTVVFWQW	63 ANCINIPLMRQRE	89 PLQVGLVGFCLVF
12 RNLLLSGAQLEAS	38 KTPTVVFWQWVNQ	64 INIPLMRQRELQV	90 VGLVGFCLVFATP
13 LLSGAQLEASRNI	39 TVVFWQWVNQSFN	65 PLMRQRELQVGIP	91 VGFCLVFATPLCC
14 GAQLEASRNIVQN	40 FWQWVNQSFNAIV	66 RQRELQVGIPVAD	92 CLVFATPLCCALF
15 LEASRNIVQNYRA	41 WVNQSFNAIVNYS	67 ELQVGIPVADEAG	93 FATPLCCALFPQK
16 SRNIVQNYRAGVV	42 QSFNAIVNYSNRS	68 VGIPVADEAGQRL	94 PLCCALFPQKSSI
17 IVQNYRAGVVTPG	43 NAIVNYSNRSGDT	69 PVADEAGQRLGYS	95 CALFPQKSSIHIS
18 NYRAGVVTPGITE	44 VNYSNRSGDTPIT	70 DEAGQRLGYSVTA	96 FPQKSSIHISNLE
19 AGVVTPGITEDQL	45 SNRSGDTPITVRQ	71 GQRLGYSVTAAKQ	97 KSSIHISNLEPEL
20 VTPGITEDQLWRA	46 SGDTPITVRQLGT	72 LGYSVTAAKQGIF	98 IHISNLEPELRAQ
21 GITEDQLWRAKYV	47 TPITVRQLGTAYV	73 SVTAAKQGIFQVV	99 SNLEPELRAQIHE
22 EDQLWRAKYVYDS	48 TVRQLGTAYVSAT	74 AAKQGIFQVVISR	100 EPELRAQIHEQNP
23 LWRAKYVYDSAFH	49 QLGTAYVSATTGA	75 QGIFQVVISRICM	101 LRAQIHEQNPSVE
24 AKYVYDSAFHPDT	50 TAYVSATTGAVAT	76 FQVVISRICMAIP	102 QIHEQNPSVEVVY
25 VYDSAFHPDTGEK	51 VSATTGAVATALG	77 VISRICMAIPAMA	103 EQNPSVEVVYYNK
26 SAFHPDTGEKVVL	52 TTGAVATALGLKS	78 RICMAIPAMAIPP	104 NPSVEVVYYNKGL

Appendix fig. 5: SFXN3 peptide spot array sequences. *The sequence of each 13mer peptide synthesised on a cellulose membrane to produce the SFXN3 peptide spot array is shown.*

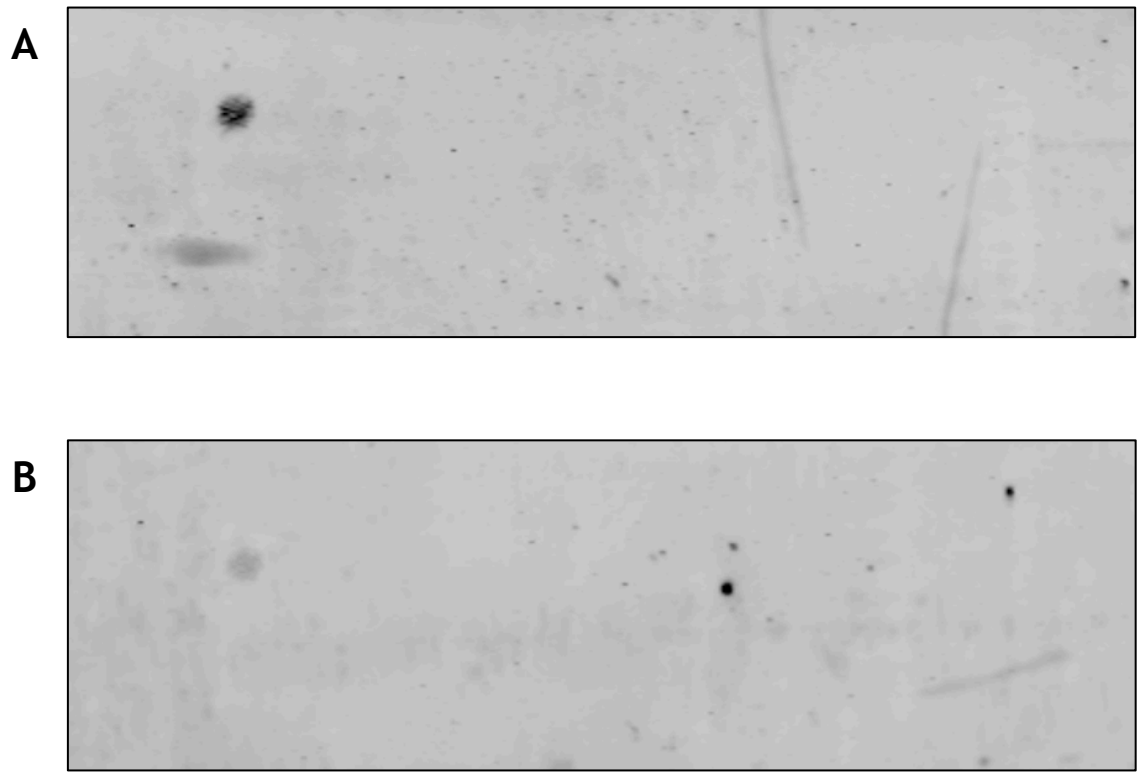

Appendix Fig. 6: Binding of Tim9/10 to SFXN3 peptide spot array, showing results from PVDF transfer two and three. *Tim9/10 complex was incubated with SFXN3 peptide membrane for 1 hour at 4℃. Protein was then transferred from the peptide membrane to a PVDF membrane three times (using fresh PVDF for each transfer) and Tim9/10 detected via Western blotting using anti-Tim10*

antibodies and fluorescence. Tim9/10 complex detected by this means is shown after the second transfer (A) and (B) the third transfer.

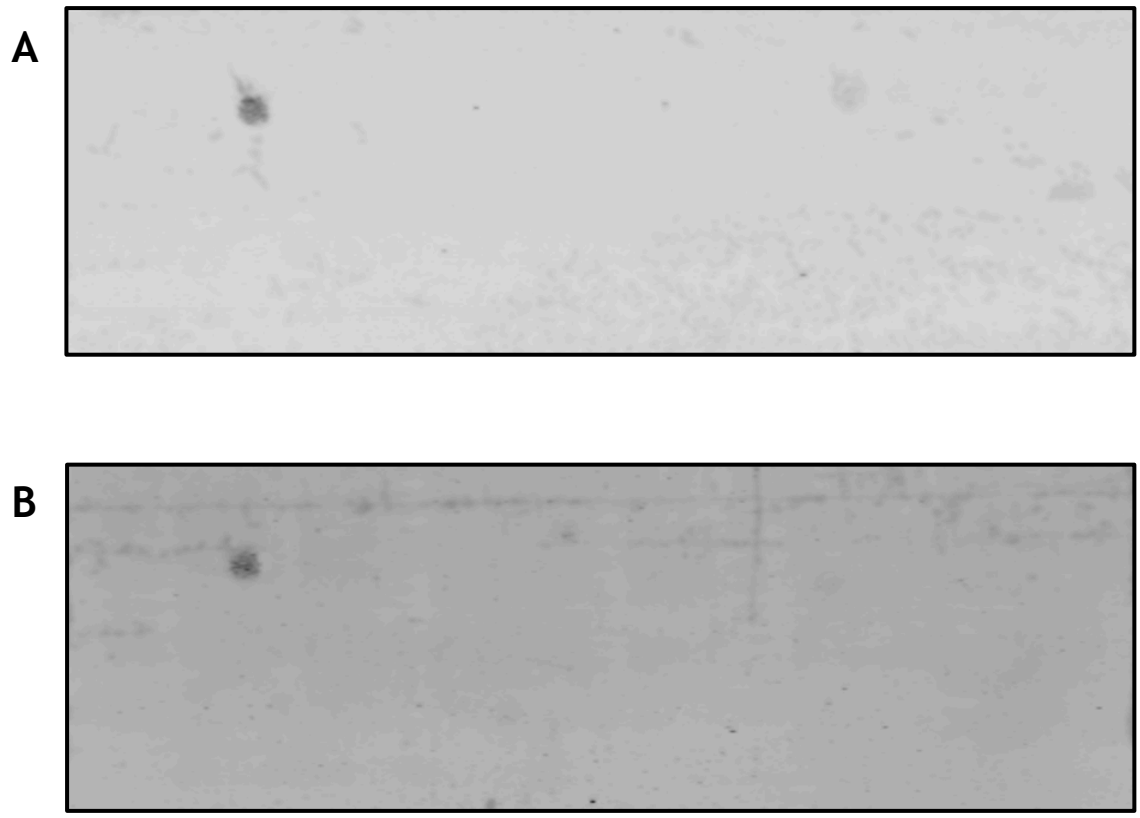

Appendix Fig. 7: Binding of Tim9/10 to SFXN3 peptide membrane, showing results from PVDF transfer one and two after troubleshooting of the JPT protocol. *Tim9/10 complex (prepared in incubation buffer) was incubated with SFXN3 peptide membrane at 4℃ overnight. Bound Tim9/10 was transferred to a PVDF membrane three times. Tim9/10 was detected via immunoblotting using anti-Tim10 (increased concentration) and fluorescence. Tim9/10 complex detected is shown after the first transfer (A) and (B) the second transfer*

A

TM Prediction Tool	Predicted TM1 (residues spanned)	Predicted TM2 (residues spanned)	Predicted TM3 (residues spanned)	Predicted TM4 (residues spanned)	Predicted TM5 (residues spanned)
HMMTOP 2.0	99-128	145-167	184-201	239-256	275-294

MEMSAT-SVM	90-106	149-164	185-200	232-254	270-291
PHOBIUS	99-121	149-167	179-200	271-292	
TOPCONS	147-167	181-201	270-290		

B

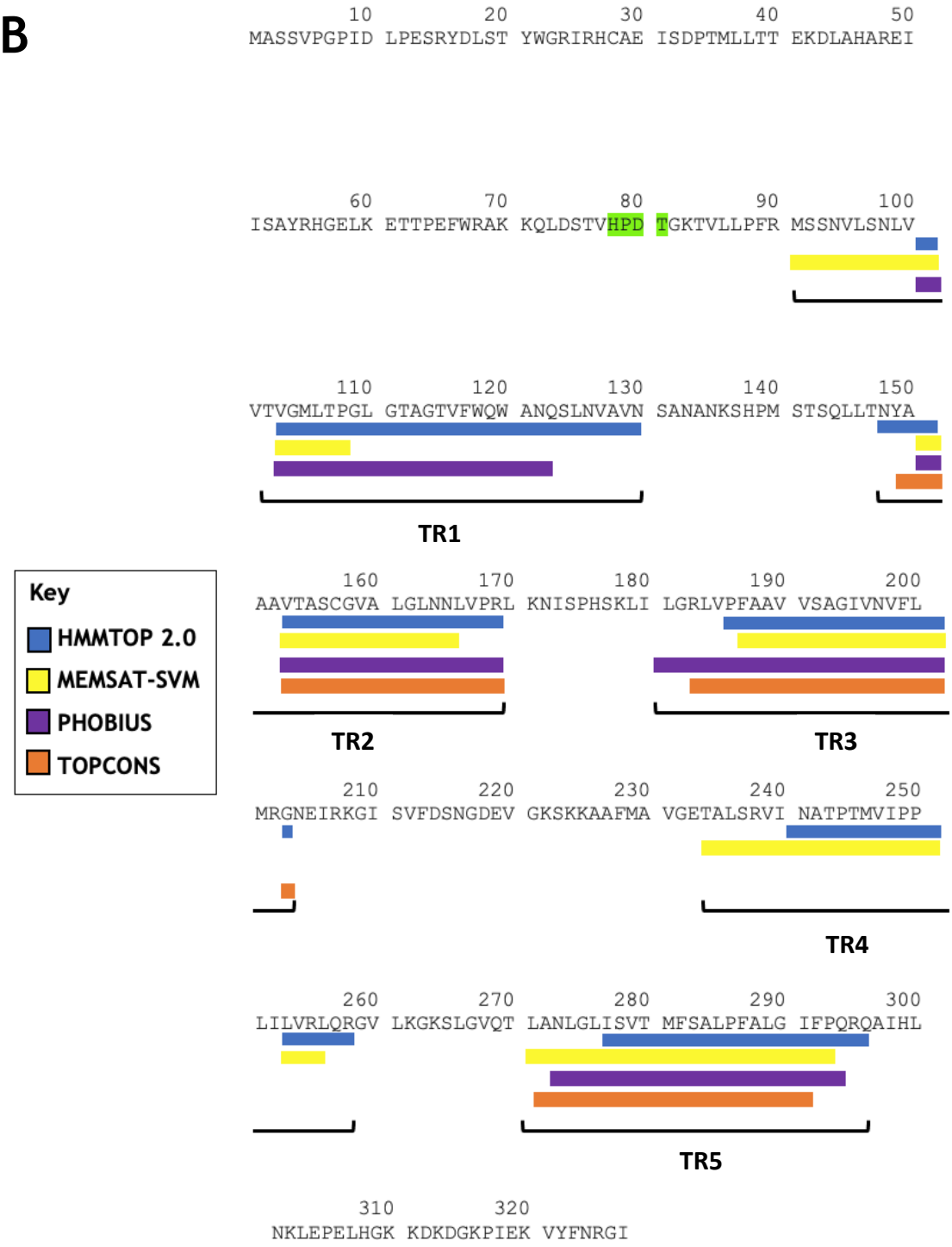

Appendix Fig. 8: Precise location of predicted TMs within the protein sequence of FSF1. (A) TM prediction tools were used to predict the location of TMs within the sequence of FSF1 (HMMTOP 2.0, MEMSAT-SVM, PHOBIUS,

TOPCONS). For each tool, the amino acid residues which each TM was predicted to span is detailed in table 1. ***(B)*** *Predicted TM regions from (A) mapped to the sequence. The five locations which contain TMs are labelled TR1-5.*

Appendix table 5: Predicted transmembrane regions of FSF1 compiled. *Table 3 shows residues numbers for the regions labelled as L1-5 in appendix fig. 8 above. The regions shown were considered as TR1-5 for the sequence and structure analysis detailed in chapter 6.*

Predicted TR1 (residues spanned)	**Predicted TR2 (residues spanned)**	**Predicted TR3 (residues spanned)**	**Predicted TR4 (residues spanned)**	**Predicted TR5 (residues spanned)**
90-128	145-167	179-201	232-254	270-294

References

Acoba, M.G., Alpergin, E.S.S., Renuse, S., Fernández-del-Río, L., Lu, Y., Khalimonchuk, O., Clarke, C.F., Pandey, A., Wolfgang, M.J. & Claypool, S.M. (2021). 'The mitochondrial carrier SFXN1 is critical for complex III integrity and cellular metabolism'. *Cell reports (Cambridge),* 34(11), 108869-108869. Doi: 10.1016/j.celrep.2021.108869

Allen, S., Balabanidou, V., Sideris, D.P., Lisowsky, T. & Tokatlidis, K. (2005). 'Erv1 Mediates the Mia40-dependent Protein Import Pathway and Provides a Functional Link to the Respiratory Chain by Shuttling Electrons to Cytochrome c'. *Journal of molecular biology,* 353(5), pp. 937-944. Doi: 10.1016/j.jmb.2005.08.049

Almannai, M., Alasmari, A., Alqasmi, A., Faqeih, E., Al Mutairi, F., Alotaibi, M., Samman, M.M., Eyaid, W., Aljadhai, Y.I., Shamseldin, H.E., Craigen, W. & Alkuraya, F.S. (2018). 'Expanding the phenotype of SLC25A42-associated mitochondrial encephalomyopathy'. *Clinical genetics,* 93(5), pp. 1097-1102. Doi: 10.1111/cge.13210

Altmann, R. (1890). *Die elementarorganismen und ihre beziehungen zu den zellen,* Veit & comp, Leipzig.

Amelio, I., Cutruzzolá, F., Antonov, A., Agostini, M. & Melino, G. (2014). 'Serine and glycine metabolism in cancer'. *Trends in biochemical sciences (Amsterdam. Regular ed.),* 39(4), pp. 191-198. Doi: 10.1016/j.tibs.2014.02.004

Amorim, I.S., Graham, L.C., Carter, R.N., Morton, N.M., Hammachi, F., Kunath, T., Pennetta, G., Carpanini, S.M., Manson, J.C., Lamont, D.J., Wishart, T.M. & Gillingwater, T.H. (2017). 'Sideroflexin 3 is an α-synuclein-dependent mitochondrial protein that regulates synaptic morphology'. *Journal of cell science,* 130(2), pp. 325-331. Doi: 10.1242/jcs.194241

Araiso, Y., Tsutsumi, A., Qiu, J., Imai, K., Shiota, T., Song, J., Lindau, C., Wenz, L., Sakaue, H., Yunoki, K., Kawano, S., Suzuki, J., Wischnewski, M., Schütze, C., Ariyama, H., Ando, T., Becker, T., Lithgow, T., Wiedemann, N., Pfanner, N., Kikkawa, M. & Endo, T. (2019). 'Structure of the mitochondrial import gate

reveals distinct preprotein paths'. *Nature (London),* 575(7782), pp. 395-401. Doi: 10.1038/s41586-019-1680-7

Armenteros, J.J.A., Salvatore, M., Emanuelsson, O., Winther, O., von Heijne, G., Elofsson, A. & Nielsen, H. (2019). 'Detecting sequence signals in targeting peptides using deep learning'. *Life science alliance* 2(5), e201900429. Doi: 10.26508/lsa.201900429

Bao, B., An, W., Lu, Q., Wang, Y., Lu, Z., Tu, J., Zhang, H., Duan, Y., Yuan, W., Zhu, X. & Jia, H. (2021). 'Sfxn1 is essential for erythrocyte maturation via facilitating hemoglobin production in zebrafish'. *Biochimica et biophysica acta. Molecular basis of disease,* 1867(5), pp. 166096-166096. Doi: 10.1016/j.bbadis.2021.166096

Becker, T., Pfannschmidt, S., Guiard, B., Stojanovski, D., Milenkovic, D., Kutik, S., Pfanner, N., Meisinger, C. & Wiedemann, N. (2008). 'Biogenesis of the Mitochondrial TOM Complex: Mim1 Promotes Insertion and Assembly of Signal-Anchored Receptors'. *The Journal of biological chemistry,* 283(1), pp. 120-127. Doi: 10.1074/jbc.M706997200

Benda, C. (1898). 'Weitere Mitteilungen über die Mitochondria'. *Verh Dtsch Physiolo Ges,* pp. 376-383.

Bender, T., Pena, G. & Martinou, J. (2015). 'Regulation of mitochondrial pyruvate uptake by alternative pyruvate carrier complexes'. *The EMBO journal,* 34(7), pp. 911-924. Doi: 10.15252/embj.201490197

Berndtsson, J., Aufschnaiter, A., Rathore, S., Marin-Buera, L., Dawitz, H., Diessl, J., Kohler, V., Barrientos, A., Büttner, S., Fontanesi, F., Ott, M. (2020). 'Respiratory supercomplexes enhance electron transport by decreasing cytochrome c diffusion distance'. *EMBO reports,* 21(12), pp. e51015. Doi: 10.15252/embr.202051015

Bihlmaier, K., Mesecke, N., Terziyska, N., Bien, M., Hell, K. & Herrmann, J.M. (2007). 'Disulfide relay system of mitochondria is connected to the respiratory chain'. *The Journal of cell biology,* 179(3), pp. 389-395. Doi: 10.1083/jcb.200707123

Bock, F.J. & Tait, S.W.G. (2020). 'Mitochondria as multifaceted regulators of cell death'. *Nature reviews. Molecular cell biology,* 21(2), pp. 85-100. Doi: 10.1038/s41580-019-0173-8

Brachmann, C.B., Davies, A., Cost, G.J., Caputo, E., Li, J., Hieter, P. & Boeke, J.D., (1998). 'Designer deletion strains derived from Saccharomyces cerevisiae S288C: A useful set of strains and plasmids for PCR-mediated gene disruption and other applications'. *Yeast,* 14(2), 115-132. Doi: 10.1002/(SICI)1097-0061(19980130)14:2<115::AID-YEA204>3.0.CO;2-2

Brzóska, K., Meczyńska, S. & Kruszewski, M. (2006). 'Iron-sulfur cluster proteins: electron transfer and beyond'. *Acta biochimica polonica,* 53(4), pp. 685-691.

Chaudhuri, M., Darden, C., Gonzalez, F.S., Singha, U.K., Quinones, L. & Tripathi, A. (2020). 'Tim17 Updates: A Comprehensive Review of an Ancient Mitochondrial Protein Translocator'. *Biomolecules (Basel, Switzerland),* 10(12), pp. 1643. Doi: 10.3390/biom10121643

Chen, W., Paradkar, P.N., Li, L., Pierce, E.L., Langer, N.B., Takahashi-Makise, N., Hyde, B.B., Shirihai, O.S., Ward, D.M., Kaplan, J. & Paw, B.H. (2009). 'Abcb10 Physically Interacts with Mitoferrin-1 (Slc25a37) to Enhance Its Stability and Function in the Erythroid Mitochondria'. *Proceedings of the National Academy of Sciences - PNAS,* 106(38), pp. 16263-16268. Doi: 10.1073/pnas.0904519106

Chen, B., Aredo, B., Ding, Y., Zhong, X., Zhu, Y., Zhao, C.X., Kumar, A., Xing, C., Gautron, L., Lyon, S., Russell, J., Li, X., Tang, M., Anderton, P., Ludwig, S., Moresco, E.M.Y., Beutler, B. & Ufret-Vincenty, R.L. (2020). 'Forward genetic analysis using OCT screening identifies Sfxn3 mutations leading to progressive outer retinal degeneration in mice'. *Proceedings of the National Academy of Sciences - PNAS,* 117(23), pp. 12931-12942. Doi: 10.1073/pnas.1921224117

Chen, K., Gong, S., Fang, X., Li, Q., Ye, M., Li, J., Huang, S., Zhao, Y., Liu, N., Li, Y. & Ma, J. (2022). 'Non-coding RNA-mediated high expression of SFXN3 as a prognostic biomarker associated with paclitaxel resistance and immunosuppressive microenvironment in head and neck cancer'. *Frontiers in immunology,* 13(1), 920136-920136. Doi: 10.3389/fimmu.2022.920136

Chipuk, J.E., Moldoveanu, T., Llambi, F., Parsons, M.J. & Green, D.R. (2010). 'The BCL-2 Family Reunion'. *Molecular cell,* 37(3), pp. 299-310. Doi: 10.1016/j.molcel.2010.01.025

Cunningham, C.N. & Rutter, J. (2020). '20,000 picometers under the OMM: diving into the vastness of mitochondrial metabolite transport'. *EMBO reports,* 21(5), e50071. Doi: 10.15252/embr.202050071

Curran, S.P., Leuenberger, D., Oppliger, W. & Koehler, C.M. (2002). 'The Tim9p-Tim10p complex binds to the transmembrane domains of the ADP/ATP carrier'. *The EMBO journal,* 21(5), 942-953. Doi: 10.1093/emboj/21.5.942

Dailey, H.A., Finnegan, M.G. & Johnson, M.K. (1994). 'Human ferrochelatase is an iron-sulfur protein'. *Biochemistry (Easton),* 33(2), pp. 403-407. Doi: 10.1021/bi00168a003

Davis, A.J., Alder, N.N., Jensen, R.E. & Johnson, A.E. (2007). 'The Tim9p/10p and Tim8p/13p complexes bind to specific sites on Tim23p during mitochondrial protein import'. *Molecular biology of the cell,* 18(2), pp. 475-486. Doi: 10.1091/mbc.e06-06-0546

Dekker, P.J.T., Keil, P., Rassow, J., Maarse, A.C., Pfanner, N. & Meijer, M. (1993). 'Identification of MIM23, a putative component of the protein import machinery of the mitochondrial inner membrane'. *FEBS letters,* 330(1), pp. 66-70. Doi: 10.1016/0014-5793(93)80921-g

Ducker, G.S. & Rabinowitz, J.D. (2017). 'One-Carbon Metabolism in Health and Disease'. *Cell metabolism,* 25(1), pp. 27-42. Doi: 10.1016/j.cmet.2016.08.009

Edwards, R., Eaglesfield, R. & Tokatlidis, K. (2021). 'The mitochondrial intermembrane space: the most constricted mitochondrial sub-compartment with the largest variety of protein import pathways'. *Open biology,* 11(3), pp. 210002-210002. Doi: 10.1098/rsob.210002

Ellenrieder, L., Mårtensson, C.U. & Becker, T. (2015). 'Biogenesis of mitochondrial outer membrane proteins, problems and diseases'. *Biological chemistry,* 396(11), pp. 1199. Doi: 10.1515/hsz-2015-0170

Esser, K., Jan, P.S., Pratje, E. & Michaelis, G. (2004). 'Mitochondrial IMP peptidase of yeast: functional analysis of domains and identification of Gut2 as a new natural substrate'. *Molecular genetics and genomics : MGG,* 271(5), pp. 616-626. Doi: 10.1007/s00438-004-1011-y

Fiesel, F.C., Geisler, S., Kahle, P.J., Springer, W., Skujat, D., Rothfuss, O.C. & Holmström, K.M. (2010). 'PINK1/Parkin-mediated mitophagy is dependent on VDAC1 and p62/SQSTM1'. *Nature cell biology,* 12(2), pp. 119-131. Doi: 10.1038/ncb2012

Fleming, M.D., Campagna, D.R., Haslett, J.N., Trenor, 3., C C & Andrews, N.C. (2001). 'A mutation in a mitochondrial transmembrane protein is responsible for the pleiotropic hematological and skeletal phenotype of flexed-tail (f/f) mice'. *Genes & development,* 15(6), 652-657. Doi: 10.1101/gad.873001

Fukasawa, Y., Tsuji, J., Fu, S., Tomii, K., Horton, P. & Imai, K. (2015). 'MitoFates: Improved Prediction of Mitochondrial Targeting Sequences and Their Cleavage Sites'. *Molecular & cellular proteomics.* 14(4), 1113-1126. Doi: 10.1074/mcp.M114.043083

Gabriel, K., Milenkovic, D., Chacinska, A., Müller, J., Guiard, B., Pfanner, N. & Meisinger, C. (2007). 'Novel Mitochondrial Intermembrane Space Proteins as Substrates of the MIA Import Pathway'. *Journal of molecular biology,* 365(3), pp. 612-620. Doi: 10.1016/j.jmb.2006.10.038

Gebert, N., Chacinska, A., Wagner, K., Guiard, B., Koehler, C.M., Rehling, P., Pfanner, N. & Wiedemann, N. (2008). 'Assembly of the three small Tim proteins precedes docking to the mitochondrial carrier translocase'. *EMBO reports,* 9(6), pp. 548-554. Doi: 10.1038/embor.2008.49

Glick, B.S. (1991). 'Chapter 20 Protein Import into Isolated Yeast Mitochondria'. *Methods in Cell Biology*, 34, 389-399. Doi: 10.1016/s0091-679x(08)61693-3

Glick, B.S., Brandt, A., Cunningham, K., Müller, S., Hallberg, R.L. & Schatz, G. (1992). 'Cytochromes c1 and b2 are sorted to the intermembrane space of yeast

mitochondria by a stop-transfer mechanism'. *Cell*, 69(5), pp. 809-822. Doi: 10.1016/0092-8674(92)90292-k

Greber, B.J. & Ban, N. (2016). 'Structure and Function of the Mitochondrial Ribosome'. *Annual review of biochemistry*, 85(1), pp. 103-132. Doi: 10.1146/annurev-biochem-060815-014343

Gurtubay, J.I., Goñi, F.M., Gómez-Fernández, J.C., Otamendi, J.J. & Macarulla, J.M. (1980). 'Triton X-100 solubilization of mitochondrial inner and outer membranes'. *Journal of bioenergetics and biomembranes*, 12(1-2), pp. 47-70. Doi: 10.1007/BF00745012

Haferkamp, I. & Schmitz-Esser, S. (2012). 'The plant mitochondrial carrier family: functional and evolutionary aspects'. *Frontiers in plant science*, 3, pp. 2-2. Doi: 10.3389/fpls.2012.00002

Hawlitschek, G., Schneider, H., Schmidt, B., Tropschug, M., Hartl, F. & Neupert, W. (1988). 'Mitochondrial protein import: Identification of processing peptidase and of PEP, a processing enhancing protein'. *Cell*, 53(5), pp. 795-806. Doi: 10.1016/0092-8674(88)90096-7

HERZIG, S., RAEMY, E., MONTESSUIT, S., VEUTHEY, J., ZAMBONI, N., WESTERMANN, B., KUNJI, E.R.S. & MARTINOU, J. (2012). 'Identification and Functional Expression of the Mitochondrial Pyruvate Carrier'. *Science (American Association for the Advancement of Science)*, 337(6090), pp. 93-96. Doi: 10.1126/science.1218530

Hildick-Smith, G., Cooney, J., Garone, C., Kremer, L., Haack, T., Thon, J., Miyata, N., Lieber, D., Calvo, S., Akman, H. ., Yien, Y., Huston, N., Branco, D., Shah, D., Freedman, M., Koehler, C., Italiano, J., Merkenschlager, A., Beblo, S., Strom, T., Meitinger, T., Freisinger, P., Donati, M. ., Prokisch, H., Mootha, V., DiMauro, S. & Paw, B. (2013). 'Macrocytic Anemia and Mitochondriopathy Resulting from a Defect in Sideroflexin 4'. *American journal of human genetics*, 93(5), pp. 906-914. Doi: 10.1016/j.ajhg.2013.09.011

Hill, K., Pfanner, N., Model, K., Ryan, M.T., Dietmeier, K., Martin, F. & Wagner, R. (1998). 'Tom40 forms the hydrophilic channel of the mitochondrial import

pore for preproteins'. *Nature (London)*, 395(6701), pp. 516-521. Doi: 10.1038/26780

Hoffman, M., Góra, M. & Rytka, J. (2003). 'Identification of rate-limiting steps in yeast heme biosynthesis'. *Biochemical and biophysical research communications*, vol. 310(4), pp. 1247-1253. Doi: 10.1016/j.bbrc.2003.09.151

Hogeboom, G. H. & Schneider, W.C. (1950). 'Cytochemical studies of mammalian tissues. III. Isocitric dehydrogenase and triphosphopyridine nucleotide-cytochrome c reductase of mouse liver'. *The Journal of biological chemistry*, 186(2), pp. 417-427. Doi: https://doi.org/10.1016/S0021-9258(18)56236-0

Höhr, A.I.C., Straub, S.P., Warscheid, B., Becker, T. & Wiedemann, N. (2015). 'Assembly of ß-barrel proteins in the mitochondrial outer membrane'. *Biochimica et biophysica acta*, 1853(1), pp. 74-88. Doi: 10.1016/j.bbamcr.2014.10.006

Hoogenraad, N.J., Ward, L.A. & Ryan, M.T. (2002). 'Import and assembly of proteins into mitochondria of mammalian cells'. *Molecular Cell Research*, 1592(1), pp. 99-105. Doi: 10.1016/s0167-4889(02)00268-9

Horowitz, M.P. & Greenamyre, J.T. (2010). 'Mitochondrial iron metabolism and its role in neurodegeneration'. *Journal of Alzheimer's disease*, 20(2), pp. S551. Doi: 10.3233/JAD-2010-100354

Horten, P., Colina-Tenorio, L. & Rampelt, H. (2020). 'Biogenesis of Mitochondrial Metabolite Carriers'. *Biomolecules (Basel, Switzerland)*, 10(7), pp. 1008. Doi: 10.3390/biom10071008

Hurt, E.C., Pesold-Hurt, B. & Schatz, G. (1984). 'The amino-terminal region of an imported mitochondrial precursor polypeptide can direct cytoplasmic dihydrofolate reductase into the mitochondrial matrix'. *The EMBO journal*, 3(13), pp. 3149-3156. Doi: 10.1002/j.1460-2075.1984.tb02272.x

Iwata, M., Lee, Y., Yamashita, T., Yagi, T., Iwata, S., Cameron, A.D. & Maher, M.J. (2012). 'Structure of the yeast NADH dehydrogenase (Ndi1) reveals overlapping binding sites for water- and lipid-soluble substrates'. *Proceedings of*

the National Academy of Sciences - PNAS, 109(38), pp. 15247-15252. Doi: 10.1073/pnas.1210059109

Jackson, T.D., Hock, D.H., Fujihara, K.M., Palmer, C.S., Frazier, A.E., Low, Y.C., Kang, Y., Ang, C., Clemons, N.J., Thorburn, D.R., Stroud, D.A. & Stojanovski, D. (2021). 'The TIM22 complex mediates the import of sideroflexins and is required for efficient mitochondrial one-carbon metabolism'. *Molecular biology of the cell*, 32(6), pp. 475-491. Doi: 10.1091/mbc.E20-06-0390

Jackson, T.D., Crameri, J.J., Muellner-Wong, L., Frazier, A.E., Palmer, C.S., Formosa, L.E., Hock, D.H., Fujihara, K.M., Stait, T., Sharpe, A.J., Thorburn, D.R., Ryan, M.T., Stroud, D.A. & Stojanovski, D. (2022). 'Sideroflexin 4 is a complex I assembly factor that interacts with the MCIA complex and is required for the assembly of the ND2 module'. *Proceedings of the National Academy of Sciences - PNAS*, 119(13), e2115566119-e2115566119. Doi: 10.1073/pnas.2115566119

Jumper, J., Evans, R., Pritzel, A., Green, T., Figurnov, M., Ronneberger, O., Tunyasuvunakool, K., Bates, R., Žídek, A., Potapenko, A., Bridgland, A., Meyer, C., Kohl, S.A.A., Ballard, A.J., Cowie, A., Romera-Paredes, B., Nikolov, S., Jain, R., Adler, J., Back, T., Petersen, S., Reiman, D., Clancy, E., Zielinski, M., Steinegger, M., Pacholska, M., Berghammer, T., Bodenstein, S., Silver, D., Vinyals, O., Senior, A.W., Kavukcuoglu, K., Kohli, P. & Hassabis, D. (2021). 'Highly accurate protein structure prediction with AlphaFold'. *Nature (London)*, 596(7873), 583-589. Doi: 10.1038/s41586-021-03819-2

Kabe, Y., Ohmori, M., Shinouchi, K., Tsuboi, Y., Hirao, S., Azuma, M., Watanabe, H., Okura, I. & Handa, H. (2006). 'Porphyrin Accumulation in Mitochondria Is Mediated by 2-Oxoglutarate Carrier'. *The Journal of biological chemistry*, 281(42), pp. 31729-31735. Doi: 10.1074/jbc.M604729200

Kaldi, K., Bauer, M.F., Sirrenberg, C., Neupert, W. & Brunner, M. (1998). 'Biogenesis of Tim23 and Tim17, integral components of the TIM machinery for matrix-targeted preproteins'. *The EMBO journal*, 17(6), pp. 1569-1576. Doi: 10.1093/emboj/17.6.1569

Käll, L., Krogh, A. & Sonnhammer, E.L.L. (2004). 'A Combined Transmembrane Topology and Signal Peptide Prediction Method'. *Journal of molecular biology,* 338(5), 1027-1036. Doi: 10.1016/j.jmb.2004.03.016

Kang, P.J., Ostermann, J., Shilling, J., Neupert, W., Craig, E.A. & Pfanner, N. (1990). 'Requirement for hsp70 in the mitochondrial matrix for translocation and folding of precursor proteins'. *Nature (London),* 348(6297), pp. 137-143. Doi: 10.1038/348137a0

Kawano, S., Yamano, K., Naoé, M., Momose, T., Terao, K., Nishikawa, S., Watanabe, N. & Endo, T. (2009). 'Structural basis of yeast Tim40/Mia40 as an oxidative translocator in the mitochondrial intermembrane space'. *Proceedings of the National Academy of Sciences - PNAS,* 106(34), pp. 14403-14407. Doi: 10.1073/pnas.0901793106

Kemper, C., Habib, S.J., Engl, G., Heckmeyer, P., Dimmer, K.S. & Rapaport, D. (2008). 'Integration of tail-anchored proteins into the mitochondrial outer membrane does not require any known import components'. *Journal of cell science,* 121(12), pp. 1990-1998. Doi: 10.1242/jcs.024034

Kennedy, E.P. & Lehninger, A.L. (1949). 'Oxidation of fatty acids and tricarboxylic acid cycle intermediates by isolated rat liver mitochondria'. *The Journal of biological chemistry,* 179(2), pp. 957-972.

Kispal, G., Csere, P., Guiard, B. & Lill, R. (1997). 'The ABC transporter Atm1p is required for mitochondrial iron homeostasis'. *FEBS letters,* 418(3), pp. 346-350. Doi: 10.1016/s0014-5793(97)01414-2

Kobayashi, K., Fujikawa, M. & Kozawa, T. (2014). 'Oxidative stress sensing by the iron–sulfur cluster in the transcription factor, SoxR'. *Journal of inorganic biochemistry,* 133, pp. 87-91. Doi: 10.1016/j.jinorgbio.2013.11.008

Komiya, T., Rospert, S., Koehler, C., Looser, R., Schatz, G. & Mihara, K. (1998). 'Interaction of mitochondrial targeting signals with acidic receptor domains along the protein import pathway: evidence for the 'acid chain' hypothesis'. *The EMBO journal,* 17(14), pp. 3886-3898. Doi: 10.1093/emboj/17.14.3886

Kory, N., Wyant, G.A., Prakash, G., Uit de Bos, J., Bottanelli, F., Pacold, M.E., Chan, S.H., Lewis, C.A., Wang, T., Keys, H.R., Guo, Y.E. & Sabatini, D.M. (2018). 'SFXN1 is a mitochondrial serine transporter required for one-carbon metabolism'. *Science (American Association for the Advancement of Science)*, 362(6416), 791. Doi: 10.1126/science.aat9528

Krimmer, T., Rapaport, D., Ryan, M.T., Meisinger, C., Kassenbrock, C.K., Blachly-Dyson, E., Forte, M., Douglas, M.G., Neupert, W., Nargang, F.E. & Pfanner, N. (2001). 'Biogenesis of Porin of the Outer Mitochondrial Membrane Involves an Import Pathway via Receptors and the General Import Pore of the TOM Complex'. *The Journal of cell biology*, 152(2), pp. 289-300. Doi: 10.1083/jcb.152.2.289

Krumpe, K., Frumkin, I., Herzig, Y., Rimon, N., Özbalci, C., Brügger, B., Rapaport, D. & Schuldiner, M. (2012). 'Ergosterol content specifies targeting of tail-anchored proteins to mitochondrial outer membranes'. *Molecular biology of the cell*, 23(20), pp. 3927-3935. Doi: 10.1091/mbc.E11-12-0994

Kudithipudi, S., Kusevic, D., Weirich, S. & Jeltsch, A. (2014). 'Specificity analysis of protein lysine methyltransferases using SPOT peptide arrays'. *Journal of Visualized Experiments : JoVE*, 93, pp. e52203-e52203. Doi: 10.3791/52203

Kudou, M., Ejima, D., Sato, H., Yumioka, R., Arakawa, T. & Tsumoto, K. (2011). 'Refolding single-chain antibody (scFv) using lauroyl- l-glutamate as a solubilization detergent and arginine as a refolding additive'. *Protein expression and purification*, 77(1), pp. 68-74. Doi: 10.1016/j.pep.2010.12.007

Kunji, E.R.S., Aleksandrova, A., King, M.S., Majd, H., Ashton, V.L., Cerson, E., Springett, R., Kibalchenko, M., Tavoulari, S., Crichton, P.G. & Ruprecht, J.J. (2016). 'The transport mechanism of the mitochondrial ADP/ATP carrier'. *Biochimica et biophysica acta*, 1863(10), pp. 2379-2393. Doi: 10.1016/j.bbamcr.2016.03.015

Kunová, N., Havalová, H., Ondrovičová, G., Stojkovičová, B., Bauer, J.A., Bauerová-Hlinková, V., Pevala, V. & Kutejová, E. (2022). 'Mitochondrial Processing Peptidases-Structure, Function and the Role in Human

Diseases'. *International journal of molecular sciences,* 23(3), pp. 1297. Doi: 10.3390/ijms23031297

Kutik, S., Stojanovski, D., Becker, L., Becker, T., Meinecke, M., Krüger, V., Prinz, C., Meisinger, C., Guiard, B., Wagner, R., Pfanner, N. & Wiedemann, N. (2008). 'Dissecting Membrane Insertion of Mitochondrial ß-Barrel Proteins'. *Cell,* 132(6), pp. 1011-1024. Doi: 10.1016/j.cell.2008.01.028

Lane, D.J.R., Merlot, A.M., Huang, M.L., Bae, D., Jansson, P.J., Sahni, S., Kalinowski, D.S. & Richardson, D.R. (2015). 'Cellular iron uptake, trafficking and metabolism: Key molecules and mechanisms and their roles in disease'. *Biochimica et biophysica acta,* 1853(5), pp. 1130-1144. Doi: 10.1016/j.bbamcr.2015.01.021

Lange, C. & Hunte, C. (2002). 'Crystal structure of the yeast cytochrome bc1 complex with its bound substrate cytochrome c'. *Proceedings of the National Academy of Sciences - PNAS,* 99(5), pp. 2800-2805. Doi: 10.1073/pnas.052704699

Ledahawsky, L.M., Terzenidou, M.E., Edwards, R., Kline, R.A., Graham, L.C., Eaton, S.L., Hoorn, D., Chaytow, H., Huang, Y., Groen, E.J.N., Motyl, A.A.L., Lamont, D.J., Tokatlidis, K., Wishart, T.M. & Gillingwater, T.H. (2022). 'The mitochondrial protein Sideroflexin 3 (SFXN3) influences neurodegeneration pathways in vivo'. *The FEBS journal,* 289(13), 3894-3914. Doi: 10.1111/febs.16377

Lemire, B.D. & Oyedotun, K.S. (2002). '*The Saccharomyces cerevisiae mitochondrial succinate:ubiquinone oxidoreductase*'. Elsevier B.V, Netherlands. Doi: 10.1016/s0005-2728(01)00229-8

Lenox, L.E., Perry, J.M. & Paulson, R.F. (2005). 'BMP4 and Madh5 regulate the erythroid response to acute anemia'. *Blood,* 105(7), pp. 2741-2748. Doi: 10.1182/blood-2004-02-0703

Letts, J.A. & Sazanov, L.A. (2017). 'Clarifying the supercomplex: the higher-order organization of the mitochondrial electron transport chain'. *Nature structural & molecular biology,* 24(10), pp. 800-808. Doi: 10.1038/nsmb.3460

Li, Y., Dudek, J., Guiard, B., Pfanner, N., Rehling, P. & Voos, W. (2004). 'The presequence translocase-associated protein import motor of mitochondria. Pam16 functions in an antagonistic manner to Pam18'. *The Journal of biological chemistry*, 279(36), pp. 38047-38054. Doi: 10.1074/jbc.M404319200

Li, X., Han, D., Kin Ting Kam, R., Guo, X., Chen, M., Yang, Y., Zhao, H. & Chen, Y. (2010). 'Developmental expression of sideroflexin family genes in Xenopus embryos'. *Developmental dynamics*, 239(10), 2742-2747. Doi: 10.1002/dvdy.22401

Lill, R., Dutkiewicz, R., Freibert, S.A., Heidenreich, T., Mascarenhas, J., Netz, D.J., Paul, V.D., Pierik, A.J., Richter, N., Stümpfig, M., Srinivasan, V., Stehling, O. & Mühlenhoff, U. (2015). 'The role of mitochondria and the CIA machinery in the maturation of cytosolic and nuclear iron–sulfur proteins'. *European journal of cell biology*, 94(7-9), pp. 280-291. Doi: 10.1016/j.ejcb.2015.05.002

Liu, X., Kim, C.N., Yang, J., Jemmerson, R. & Wang, X. (1996). 'Induction of Apoptotic Program in Cell-Free Extracts: Requirement for dATP and Cytochrome c'. *Cell*, 86(1), pp. 147-157. Doi: 10.1016/s0092-8674(00)80085-9

Liu, J., Rone, M.B. & Papadopoulos, V. (2006). 'Protein-Protein Interactions Mediate Mitochondrial Cholesterol Transport and Steroid Biosynthesis'. *The Journal of biological chemistry*, 281(50), pp. 38879-38893. Doi: 10.1074/jbc.M608820200

Liu, G., Sil, D., Maio, N., Tong, W., Bollinger, J., J Martin, Krebs, C. & Rouault, T.A. (2020). 'Heme biosynthesis depends on previously unrecognized acquisition of iron-sulfur cofactors in human amino-levulinic acid dehydratase'. *Nature communications*, 11(1), pp. 6310-6310. Doi: 10.1038/s41467-020-20145-9

Lockhart, P.J., Holtom, B., Lincoln, S., Hussey, J., Zimprich, A., Gasser, T., Wszolek, Z.K., Hardy, J. & Farrer, M.J. (2002). 'The human sideroflexin 5 (SFXN5) gene: sequence, expression analysis and exclusion as a candidate for PARK3'. *Gene*, 285(1), pp. 229-237. Doi: 10.1016/s0378-1119(02)00402-x

Luciano, P., Vial, S., Vergnolle, M.A.S., Dyall, S.D., Robinson, D.R. & Tokatlidis, K. (2001). 'Functional reconstitution of the import of the yeast ADP/ATP carrier

mediated by the TIM10 complex'. *The EMBO journal*, 20(15), pp. 4099-4106. Doi: 10.1093/emboj/20.15.4099

Lytovchenko, O., Melin, J., Schulz, C., Kilisch, M., Hutu, D.P. & Rehling, P. (2013). 'Signal recognition initiates reorganization of the presequence translocase during protein import'. *The EMBO journal*, 32(6), pp. 886-898. Doi: 10.1038/emboj.2013.23

Mariani, V., Biasini, M., Barbato, A. & Schwede, T. (2013). 'lDDT: a local superposition-free score for comparing protein structures and models using distance difference tests'. *Bioinformatics*, 29(21), pp. 2722-2728. Doi: 10.1093/bioinformatics/btt473

Marobbio, C.M.T., Giannuzzi, G., Paradies, E., Pierri, C.L. & Palmieri, F. (2008). 'α-Isopropylmalate, a Leucine Biosynthesis Intermediate in Yeast, Is Transported by the Mitochondrial Oxalacetate Carrier'. *The Journal of biological chemistry*, 283(42), pp. 28445-28453. Doi: 10.1074/jbc.M804637200

Martínez-Reyes, I. & Chandel, N.S. (2020). 'Mitochondrial TCA cycle metabolites control physiology and disease'. *Nature communications*, 11(1), pp. 102-11. Doi: 10.1038/s41467-019-13668-3

Mesecke, N., Terziyska, N., Kozany, C., Baumann, F., Neupert, W., Hell, K. & Herrmann, J.M. (2005). 'A Disulfide Relay System in the Intermembrane Space of Mitochondria that Mediates Protein Import'. *Cell*, 121(7), pp. 1059-1069. Doi: 10.1016/j.cell.2005.04.011

Mills, E.L., Pierce, K.A., Jedrychowski, M.P., Garrity, R., Winther, S., Vidoni, S., Yoneshiro, T., Spinelli, J.B., Lu, G.Z., Kazak, L., Banks, A.S., Haigis, M.C., Kajimura, S., Murphy, M.P., Gygi, S.P., Clish, C.B. & Chouchani, E.T. (2018). 'Accumulation of succinate controls activation of adipose tissue thermogenesis'. *Nature (London)*, 560(7716), pp. 102-106. Doi: 10.1038/s41586-018-0353-2

Milenkovic, D., Ramming, T., Müller, J.M., Wenz, L., Gebert, N., Schulze-Specking, A., Stojanovski, D., Rospert, S. & Chacinska, A. (2009). 'Identification of the signal directing Tim9 and Tim10 into the intermembrane space of

mitochondria'. *Molecular biology of the cell*, 20(10), pp. 2530-2539. Doi: 10.1091/mbc.E08-11-1108

Miotto, G., Tessaro, S., Rotta, G.A. & Bonatto, D. (2007). 'In silico analyses of Fsf1 sequences, a new group of fungal proteins orthologous to the metazoan sideroblastic anemia-related sideroflexin family'. *Fungal genetics and biology*, 44(8), 740-753. Doi: 10.1016/j.fgb.2006.12.004

Mitraki, A., Fane, B., Haase-Pettingell, C., Sturtevant, J. & King, J. (1991). 'Global Suppression of Protein Folding Defects and Inclusion Body Formation'. *Science (American Association for the Advancement of Science)*, 253(5015), pp. 54-58. Doi: 10.1126/science.1648264

Miyake, S., Yamashita, T., Taniguchi, M., Tamatani, M., Sato, K. & Tohyama, M. (2002). 'Identification and characterization of a novel mitochondrial tricarboxylate carrier'. *Biochemical and biophysical research communications*, 295(2), 463-468. Doi: 10.1016/s0006-291x(02)00694-0

Mon, E.E., Wei, F., Ahmad, R.N.R., Yamamoto, T., Moroishi, T. & Tomizawa, K. (2019). 'Regulation of mitochondrial iron homeostasis by sideroflexin 2'. *The journal of physiological sciences*, 69(2), 359-373. Doi: 10.1007/s12576-018-0652-2

Mordas, A. & Tokatlidis, K. (2015). 'The MIA Pathway: A Key Regulator of Mitochondrial Oxidative Protein Folding and Biogenesis'. *Accounts of chemical research*, 48(8), pp. 2191-2199. Doi: 10.1021/acs.accounts.5b00150

Neginskaya, M.A., Pavlov, E.V. & Sheu, S. (2021). 'Electrophysiological properties of the mitochondrial permeability transition pores: Channel diversity and disease implication'. *Biochimica et biophysica acta. Bioenergetics*, 1862(3), pp. 148357-148357. Doi: 10.1016/j.bbabio.2020.148357

Nemani, V.M., Lu, W., Berge, V., Nakamura, K., Onoa, B., Lee, M.K., Chaudhry, F.A., Nicoll, R.A. & Edwards, R.H. (2010). 'Increased Expression of α-Synuclein Reduces Neurotransmitter Release by Inhibiting Synaptic Vesicle Reclustering after Endocytosis'. *Neuron (Cambridge, Mass.)*, 65(1), pp. 66-79. Doi: 10.1016/j.neuron.2009.12.023

Nugent, T. & Jones, D.T. (2009). 'Transmembrane protein topology prediction using support vector machines'. *BMC bioinformatics*. 10(1), 159-159. Doi: 10.1186/1471-2105-10-159

Nygaard, R., Kim, J. & Mancia, F. (2020). 'Cryo-electron microscopy analysis of small membrane proteins'. *Current opinion in structural biology,* 64(1), pp. 26-33. Doi: 10.1016/j.sbi.2020.05.009

Ohsato, T., Ishihara, N., Muta, T., Umeda, S., Ikeda, S., Mihara, K., Hamasaki, N. & Kang, D. (2002). 'Mammalian mitochondrial endonuclease G. Digestion of R-loops and localization in intermembrane space'. *European journal of biochemistry,* 269(23), pp. 5765-5770. Doi: 10.1046/j.1432-1033.2002.03238.x

Omasits, U., Ahrens, C.H., Müller, S. & Wollscheid, B. (2014). 'Protter: interactive protein feature visualization and integration with experimental proteomic data'. *Bioinformatics,* 30(6), 884-886.

Ostermann, J., Horwich, A.L., Neupert, W. & Hartl, F. (1989). 'Protein folding in mitochondria requires complex formation with hsp60 and ATP hydrolysis'. *Nature (London),* 341(6238), pp. 125-130. Doi: 10.1038/341125a0

Paggio, A., Checchetto, V., Campo, A., Menabò, R., Di Marco, G., Di Lisa, F., Szabo, I., Rizzuto, R. & De Stefani, D. (2019). 'Identification of an ATP-sensitive potassium channel in mitochondria'. *Nature (London),* 572(7771), pp. 609-613. Doi: 10.1038/s41586-019-1498-3

Palade, G.E. (1953). 'AN ELECTRON MICROSCOPE STUDY OF THE MITOCHONDRIAL STRUCTURE'. *The journal of histochemistry and cytochemistry,* 1(4), pp. 188-211. Doi: 10.1177/1.4.188

Park, K., Botelho, S.C., Hong, J., Österberg, M. & Kim, H. (2013). 'Dissecting Stop Transfer versus Conservative Sorting Pathways for Mitochondrial Inner Membrane Proteins in Vivo'. *The Journal of biological chemistry,* 288(3), pp. 1521-1532. Doi: 10.1074/jbc.M112.409748

Paul, B.T., Manz, D.H., Torti, F.M. & Torti, S.V. (2017). 'Mitochondria and Iron: current questions'. *Expert review of hematology,* 10(1), pp. 65. Doi: 10.1080/17474086.2016.1268047

Paul, B.T., Tesfay, L., Winkler, C.R., Torti, F.M. & Torti, S.V. (2019). 'Sideroflexin 4 affects Fe-S cluster biogenesis, iron metabolism, mitochondrial respiration and heme biosynthetic enzymes'. *Scientific reports,* 9(1), pp. 19634-13. Doi: 10.1038/s41598-019-55907-z

Paw, B.H., Shaw, G.C., Cope, J.J., Li, L., Corson, K., Hersey, C., Ackermann, G.E., Gwynn, B., Lambert, A.J., Wingert, R.A., Traver, D., Trede, N.S., Barut, B.A., Zhou, Y., Minet, E., Donovan, A., Brownlie, A., Balzan, R., Weiss, M.J., Peters, L.L., Kaplan, J. & Zon, L.I. (2006). 'Mitoferrin is essential for erythroid iron assimilation'. *Nature,* 440(7080), pp. 96-100. Doi: 10.1038/nature04512

Pebay-Peyroula, E., Brandolin, G., Dahout-Gonzalez, C., Kahn, R., Trézéguet, V. & Lauquin, G.J. (2003). 'Structure of mitochondrial ADP/ATP carrier in complex with carboxyatractyloside'. *Nature,* 426(6962), 39-44. Doi: 10.1038/nature02056

Pettersen, E.F., Goddard, T.D., Huang, C.C., Meng, E.C., Couch, G.S., Croll, T.I., Morris, J.H. & Ferrin, T.E. (2021). 'UCSF ChimeraX: Structure visualization for researchers, educators, and developers'. *Protein science,* 30(1), 70-82. Doi: 10.1002/pro.3943

Pfanner, N. (2000). 'Protein sorting: Recognizing mitochondrial presequences'. *Current biology,* 10(11), pp. R412-R415. Doi: 10.1016/s0960-9822(00)00507-8

Pfanner, N. & Neupert, W. (1987). 'Distinct steps in the import of ADP/ATP carrier into mitochondria'. *The Journal of biological chemistry,* 262(16), pp. 7528-7536.

Pfanner, N., Meisinger, C. & Schmidt, O. (2010). 'Mitochondrial protein import: from proteomics to functional mechanisms'. *Nature reviews. Molecular cell biology,* 11(9), pp. 655-667. Doi: 10.1038/nrm2959

Rath, S., Sharma, R., Gupta, R., Ast, T., Chan, C., Durham, T.J., Goodman, R.P., Grabarek, Z., Haas, M.E., Hung, W.H.W., Joshi, P.R., Jourdain, A.A., Kim,

S.H., Kotrys, A.V., Lam, S.S., McCoy, J.G., Meisel, J.D., Miranda, M., Panda, A., Patgiri, A., Rogers, R., Sadre, S., Shah, H., Skinner, O.S., To, T., Walker, M., Wang, H., Ward, P.S., Wengrod, J., Yuan, C., Calvo, S.E. & Mootha, V.K. (2021). 'MitoCarta3.0: an updated mitochondrial proteome now with sub-organelle localization and pathway annotations'. *Nucleic acids research,* 49(D1), pp. D1541-D1547. Doi: 10.1093/nar/gkaa1011

Rathore, S., Berndtsson, J., Marin-Buera, L., Conrad, J., Carroni, M., Brzezinski, P. & Ott, M. (2019). 'Cryo-EM structure of the yeast respiratory supercomplex'. *Nature structural & molecular biology,* 26(1), pp. 50-57. Doi: 10.1038/s41594-018-0169-7

Rivell, A., Petralia, R.S., Wang, Y., Mattson, M.P. & Yao, P.J. (2019). 'Sideroflexin 3 is a Mitochondrial Protein Enriched in Neurons'. *Neuromolecular medicine,* 21(3), pp. 314-321. Doi: 10.1007/s12017-019-08553-7

Ruprecht, J.J. & Kunji, E.R.S. (2019). 'The SLC25 Mitochondrial Carrier Family: Structure and Mechanism'. *Trends in biochemical sciences (Amsterdam. Regular ed.),* 45(3), pp. 244-258. Doi: 10.1016/j.tibs.2019.11.001

Ryan, M.T., Muller, H. & Pfanner, N. (1999). 'Functional staging of ADP/ATP carrier translocation across the outer mitochondrial membrane'. *The Journal of biological chemistry,* 274(29), pp. 20619-20627. Doi: 10.1074/jbc.274.29.20619

Saraste, M. & Walker, J.E. (1982). 'Internal sequence repeats and the path of polypeptide in mitochondrial ADP/ATP translocase'. *FEBS letters,* 144(2), pp. 250-254. Doi: 10.1016/0014-5793(82)80648-0

Sawicki, K.T., Chang, H. & Ardehali, H. 2015, "Role of heme in cardiovascular physiology and disease", *Journal of the American Heart Association,* vol. 4, no. 1, pp. e001138-e001138. Doi: 10.1161/JAHA.114.001138

Schiestl, R.H. & Gietz, R.D. (2007). 'Frozen competent yeast cells that can be transformed with high efficiency using the LiAc/SS carrier DNA/PEG method'. *Nature protocols,* 2(1), 1-4. Doi: 10.1038/nprot.2007.17

Schlame, M. (2008). 'Cardiolipin synthesis for the assembly of bacterial and mitochondrial membranes'. *Journal of lipid research,* 49(8), pp. 1607-1620. Doi: 10.1194/jlr.R700018-JLR200

Schlisselberg, D., Mazarib, E., Inbar, E., Rentsch, D., Myler, P.J. & Zilberstein, D. (2015). 'Size does matter: 18 amino acids at the N-terminal tip of an amino acid transporter in Leishmania determine substrate specificity'. *Scientific reports,* 5(1), 16289-16289. Doi: 10.1038/srep16289

Schmidt, T., Situ, A.J. & Ulmer, T.S. (2016). 'Structural and thermodynamic basis of proline-induced transmembrane complex stabilization'. *Scientific reports,* 6(1), 29809-29809. Doi: 10.1038/srep29809

Seo, B.B., Nakamaru-Ogiso, E., Flotte, T.R., Matsuno-Yagi, A. & Yagi, T. (2006). 'In vivo complementation of complex I by the yeast Ndi1 enzyme. Possible application for treatment of Parkinson disease'. *The Journal of biological chemistry*, 281(20), pp. 14250-14255. Doi: 10.1074/jbc.M600922200

Sha, B. & Wu, Y. (2006). 'Crystal structure of yeast mitochondrial outer membrane translocon member Tom70p'. *Nature structural & molecular biology,* 13(7), pp. 589-593. Doi: 10.1038/nsmb1106

Sherman, F. (1964). 'Mutants of yeast deficient in cytochrome C'. *Genetics,* 49(1), 39-48. https://doi.org/10.1093/genetics/49.1.39

Shi, R., Hou, W., Wang, Z. & Xu, X. (2021). 'Biogenesis of Iron-Sulfur Clusters and Their Role in DNA Metabolism'. *Frontiers in cell and developmental biology,* 9, pp. 735678-735678. Doi: 10.3389/fcell.2021.735678

Sideris, D.P., Petrakis, N., Katrakili, N., Mikropoulou, D., Gallo, A., Ciofi-Baffoni, S., Banci, L., Bertini, I. & Tokatlidis, K. (2009). 'A novel intermembrane space-targeting signal docks cysteines onto Mia40 during mitochondrial oxidative folding'. *The Journal of Cell Biology,* 187(7), 1007-1022. doi: 10.1083/jcb.200905134.

Singh, A., Upadhyay, V., Upadhyay, A.K., Singh, S.M. & Panda, A.K. (2015). 'Protein recovery from inclusion bodies of Escherichia coli using mild

solubilization process'. *Microbial cell factories,* 14(1), pp. 41-41. Doi: 10.1186/s12934-015-0222-8

Sjostrand, F.S. (1953). 'Electron microscopy of mitochondria and cytoplasmic double membranes'. *Nature (London),* 171(4340), pp. 30-32. Doi: 10.1038/171030a0

Song, G., Zhang, S., Tian, M., Zhang, L., Guo, R., Zhuo, W. & Yang, M. (2021). 'Molecular insights into the human ABCB6 transporter'. *Cell discovery,* 7(1), pp. 55-55. Doi: 10.1038/s41421-021-00284-z

Szymczak, L.C., Kuo, H. & Mrksich, M. (2017). 'Peptide Arrays: Development and Application'. *Analytical chemistry (Washington),* 90(1), pp. 266-282. Doi: 10.1021/acs.analchem.7b04380

Tifoun, N., De Las Heras, José M, Guillaume, A., Bouleau, S., Mignotte, B. & Le Floch, N. (2021). 'Insights into the Roles of the Sideroflexins/SLC56 Family in Iron Homeostasis and Iron-Sulfur Biogenesis'. *Biomedicines,* 9(2), 103. Doi: 10.3390/biomedicines9020103

Tifoun, N., Bekhouche, M., José M De las Heras, Guillaume, A., Bouleau, S., Guénal, I., Mignotte, B. & Floch, N.L. (2022). 'A High-Throughput Search for SFXN1 Physical Partners Led to the Identification of ATAD3, HSD10 and TIM50'. *Biology (Basel, Switzerland),* 11(9), pp. 1298. Doi: 10.3390/biology11091298

Tsirigos, K.D., Peters, C., Shu, N., Kall, L. & Elofsson, A. (2015). The TOPCONS web server for consensus prediction of membrane protein topology and signal peptides. *Nucleic acids research,* 43(W1), W401-W407. Doi: 10.1093/nar/gkv485

Tusnády, G.E. & Simon, I. (2001). 'The HMMTOP transmembrane topology prediction server'. *Bioinformatics,* 17(9), 849-850. Doi: 10.1093/bioinformatics/17.9.849

van Wilpe, S., Ryan, M.T., Hill, K., Maarse, A.C., Meisinger, C., Brix, J., Dekker, P.J., Moczko, M., Wagner, R.e. & Meijer, M. (1999). 'Tom22 is a multifunctional organizer of the mitochondrial preprotein translocase'. *Nature (London),* 401(6752), pp. 485-489. Doi: 10.1038/46802

Varadi, M., Anyango, S., Deshpande, M., Nair, S., Natassia, C., Yordanova, G., Yuan, D., Stroe, O., Wood, G., Laydon, A., Žídek, A., Green, T., Tunyasuvunakool, K., Petersen, S., Jumper, J., Clancy, E., Green, R., Vora, A., Lutfi, M., Figurnov, M., Cowie, A., Hobbs, N., Kohli, P., Kleywegt, G., Birney, E., Hassabis, D. & Velankar, S. (2022). 'AlphaFold Protein Structure Database: massively expanding the structural coverage of protein-sequence space with high-accuracy models'. *Nucleic acids research,* 50(D1), D439-D444. Doi: 10.1093/nar/gkab1061

Vasiljev, A., Ahting, U., Nargang, F.E., Go, N.E., Habib, S.J., Kozany, C., Panneels, V., Sinning, I., Prokisch, H., Neupert, W., Nussberger, S. & Rapaport, D. (2004). 'Reconstituted TOM core complex and Tim9/Tim10 complex of mitochondria are sufficient for translocation of the ADP/ATP carrier across membranes'. *Molecular biology of the cell,* 15(3), 1445-1458. Doi: 10.1091/mbc.e03-05-0272

Vazquez, C. & Horner, S.M. (2015). 'MAVS Coordination of Antiviral Innate Immunity'. *Journal of virology,* 89(14), pp. 6974-6977. Doi: 10.1128/JVI.01918-14

Vergnolle, M.A.S., Baud, C., Golovanov, A.P., Alcock, F., Luciano, P., Lian, L. & Tokatlidis, K. (2005). 'Distinct Domains of Small Tims Involved in Subunit Interaction and Substrate Recognition'. *Journal of molecular biology,* 351(4), 839-849. Doi: 10.1016/j.jmb.2005.06.010

Vial, S., Lu, H., Allen, S., Savory, P., Thornton, D., Sheehan, J. & Tokatlidis, K. (2002). 'Assembly of Tim9 and Tim10 into a Functional Chaperone'. *The Journal of biological chemistry,* 277(39), pp. 36100-36108. Doi: 10.1074/jbc.M202310200

Vögtle, F., Wortelkamp, S., Zahedi, R.P., Becker, D., Leidhold, C., Gevaert, K., Kellermann, J., Voos, W., Sickmann, A., Pfanner, N. & Meisinger, C. (2009). 'Global Analysis of the Mitochondrial N-Proteome Identifies a Processing Peptidase Critical for Protein Stability'. *Cell,* 139(2), pp. 428-439. Doi: 10.1016/j.cell.2009.07.045

Vögtle, F., Burkhart, J.M., Rao, S., Gerbeth, C., Hinrichs, J., Martinou, J., Chacinska, A., Sickmann, A., Zahedi, R.P. & Meisinger, C. (2012).

‘Intermembrane Space Proteome of Yeast Mitochondria’. *Molecular & cellular proteomics,* 11(12), pp. 1840-1852. Doi: 10.1074/mcp.M112.021105

Vukotic, M., Nolte, H., König, T., Saita, S., Ananjew, M., Krüger, M., Tatsuta, T. & Langer, T. (2017). ‘Acylglycerol Kinase Mutated in Sengers Syndrome Is a Subunit of the TIM22 Protein Translocase in Mitochondria’. *Molecular cell,* 67(3), pp. 471-483.e7. Doi: 10.1016/j.molcel.2017.06.013

Watkins, A.M. & Arora, P.S. (2014). ‘Anatomy of β-Strands at Protein–Protein Interfaces’. *ACS chemical biology,* 9(8), 1747-1754. Doi: 10.1021/cb500241y

Webb, C.T., Gorman, M.A., Lazarou, M., Ryan, M.T. & Gulbis, J.M. (2006). ‘Crystal Structure of the Mitochondrial Chaperone TIM9•10 Reveals a Six-Bladed α-Propeller’. *Molecular cell,* 21(1), pp. 123-133. Doi: 10.1016/j.molcel.2005.11.010

Weinhäupl, K., Lindau, C., Hessel, A., Wang, Y., Schütze, C., Jores, T., Melchionda, L., Schönfisch, B., Kalbacher, H., Bersch, B., Rapaport, D., Brennich, M., Lindorff-Larsen, K., Wiedemann, N. & Schanda, P. (2018). ‘Structural Basis of Membrane Protein Chaperoning through the Mitochondrial Intermembrane Space’. *Cell,* 175(5), pp. 1365-1379.e25. Doi: 10.1016/j.cell.2018.10.039

Wenz, L., Ellenrieder, L., Qiu, J., Bohnert, M., Zufall, N., van der Laan, M., Pfanner, N., Wiedemann, N. & Becker, T. (2015). ‘Sam37 is crucial for formation of the mitochondrial TOM-SAM supercomplex, thereby promoting β-barrel biogenesis’. *The Journal of cell biology,* 210(7), pp. 1047-1054. Doi: 10.1083/jcb.201504119

Wiedemann, N., Pfanner, N. & Ryan, M.T. (2001). ‘The three modules of ADP/ATP carrier cooperate in receptor recruitment and translocation into mitochondria’. *The EMBO journal,* 20(5), pp. 951-960. Doi: 10.1093/emboj/20.5.951

Wiedemann, N., Kozjak, V., Chacinska, A., Schönfisch, B., Rospert, S., Ryan, M.T., Pfanner, N. & Meisinger, C. (2003). ‘Machinery for protein sorting and assembly in the mitochondrial outer membrane’. *Nature (London),* 424(6948), pp. 565-571. Doi: 10.1038/nature01753

Wiedemann, N., van der Laan, M., Hutu, D.P., Rehling, P. & Pfanner, N. (2007). 'Sorting switch of mitochondrial presequence translocase involves coupling of motor module to respiratory chain'. *The Journal of cell biology*, 179(6), pp. 1115-1122. Doi: 10.1083/jcb.200709087

Wiedemann, N. & Pfanner, N. (2017). 'Mitochondrial Machineries for Protein Import and Assembly'. *Annual review of biochemistry*, 86(1), pp. 685-714. Doi: 10.1146/annurev-biochem-060815-014352

Yano, M., Terada, K. & Mori, M. (2004). 'Mitochondrial Import Receptors Tom20 and Tom22 Have Chaperone-like Activity'. *The Journal of biological chemistry*, 279(11), pp. 10808-10813. Doi: 10.1074/jbc.M311710200

Yoshikumi, Y., Mashima, H., Ueda, N., Ohno, H., Suzuki, J., Tanaka, S., Hayashi, M., Sekine, N., Ohnishi, H., Yasuda, H., Iiri, T., Omata, M., Fujita, T. & Kojima, I. (2005). 'Roles of CTPL/Sfxn3 and Sfxn family members in pancreatic islet'. *Journal of cellular biochemistry*, 95(6), 1157-1168. Doi: 10.1002/jcb.20481

Young, M.J., Bay, D.C., Hausner, G. & Court, D.A. (2007). 'The evolutionary history of mitochondrial porins'. *BMC evolutionary biology*, 7(1), pp. 31-31. Doi: 10.1186/1471-2148-7-31